PHASE STABILITY, SINTERING, AND ELECTRICAL PROPERTIES

OF THE (Mg,Ni,Co,Cu,Zn)O ENTROPY STABILIZED

OXIDE SYSTEM

by

Katie Gann

A thesis submitted to the Faculty and the Board of Trustees of the Colorado School of Mines in partial fulfillment of the requirements for the degree of Master of Science (Materials Science).

Golden, Colorado

Date _____

                                         Signed: _____
                                                                        Katie Gann

                                         Signed: _____
                                                              Dr. Geoffrey Brennecka
                                                                       Thesis Advisor

Golden, Colorado

Date _____

                                         Signed: _____
                                                                  Dr. Ryan O'Hayre
                                                          Professor and Program Chair
                                                          Program of Materials Science

ABSTRACT

This thesis focuses on the synthesis and characterization of the recently discovered (Mg,Ni,Co,Cu,Zn)O entropy stabilized oxide. In this system, oxygen populates the anion sublattice of the FCC rock-salt structure while the five cations randomly populate the cation sublattice. Configurational entropy drives the formation of a single-phase solid solution, overcoming the enthalpy of mixing of the five components. The temperature required for this transition is minimized for the $(Mg_{0.2}Ni_{0.2}Co_{0.2}Cu_{0.2}Zn_{0.2})O$ composition because configurational entropy is maximized for equimolar amounts of each cation.

Various techniques are employed to characterize the formation of the single phase and its stability under different thermal treatments. Upon heating a single-phase sample at temperatures between 600 and 875 °C, a copper-rich tenorite precipitate forms, providing another method for controlling the microstructure. The reversibility of the formation of the single-phase solution is paramount to the entropy stabilization.

Octahedrally coordinated Cu^{2+} ions exhibit a Jahn-Teller distortion and have been shown to cluster within the rock-salt lattice to relieve the stress induced by these distorted bonds. The global structure of this entropy-stabilized single phase is rock-salt; under certain processing conditions, selective peak broadening appears which suggests the presence of lattice distortion. This is hypothesized to be the result of copper-rich nanoscale defects where the cations are displaced from ideal lattice sites, due to the tetragonal distortion around these ions.

Samples were sintered to >95% density using mixed oxide processing and solid-state sintering, which is an improvement on previous attempts to densify this material by similar methods. Dilatometry revealed two distinct temperature regimes where densification occurs at different rates, indicating the presence of different active sintering mechanisms.

DC and AC measurements were employed to characterize the electrical properties of dense samples. The single-phase entropy stabilized oxide is insulating at room temperature with resistivity values on the order of 10^9 Ω m and possesses several thermally activated conduction mechanisms. When heat treated at lower temperatures to precipitate tenorite, the electrical resistivity drops by six orders of magnitude.

TABLE OF CONTENTS

LIST OF FIGURES

vii

x

LIST OF TABLES AND EQUATIONS

CHAPTER ONE: INTRODUCTION

A common goal in the field of materials science is to design materials with tailored and tunable properties. While traditional materials design has focused on the use of a few principal materials with minor amounts of additional elements as dopants, there has been a shift towards incorporating more principal elements into materials systems. Various computational methods that screen potential energy surfaces for local and global minima to predict stable phases are limited to lower temperatures, missing the entire phase space at elevated temperatures where entropy dominates the free energy landscape [1], [2]. The first high entropy alloy (HEA) was proposed in 2004 [3], utilizing the stabilization afforded by engineering configurational entropy into a system [4]. HEAs have been defined as having five or more principal elements where the contents of each element ranges from 5 to 35%, yielding the maximum configurational entropy when the contents of the material are equimolar [3]. HEAs have been found to possess exceptional ductility and strain hardening, resistance to oxidation and radiation, as well as potential applications as superconductors and in hydrogen storage [5], [6]. Despite the field being less than 15 years old, it has already inspired significant exploration of the vast alloy composition space of multicomponent systems.

While there is much debate about whether HEAs are truly stabilized by their large configurational entropy due to possessing regions of inhomogeneity, the concept of HEAs has been expanded to the fields of polymers, composites, and ceramics, where the high entropy of mixing enhances the formation of simple solutions at high temperatures. The ability to tune the number of components, compositions, and processing techniques has led to materials with a wide range of properties and microstructures with targeted applications in turbine blades, thermal spray coatings, carbides for cutting tools, and more [7].

This thesis report will focus on a recently discovered system, $(Mg,Ni,Co,Cu,Zn)O$, that is stabilized by configurational entropy, rather than by its enthalpy of formation. The phase stability of this material system is investigated under different heat treatments to identify the conditions under which a single, entropy-stabilized phase forms. The phase stability is also investigated over temperature ranges where multi-phase systems are favored and where peak broadening occurs,

likely as a result of cation segregation. The sintering and densification of the (Mg,Ni,Co,Cu,Zn)O system is also investigated to determine thermal profiles that yield dense samples using bulk processing methods and solid state sintering. Lastly, various electrical measurements on dense single and multi-phase samples are discussed. The purpose of this study is to further characterize this materials system and contribute to the rapidly expanding body of literature on the class of entropy stabilized materials.

CHAPTER TWO: LITERATURE REVIEW

Because the field pertaining to entropy stabilized oxides is relatively new, the body of literature is still relatively small and growing quickly. This section focuses on some of the useful thermodynamics concepts for understanding entropy stabilization and the relevant background literature to this project, including the original paper proposing the (Mg,Ni,Co,Cu,Zn)O system, additional characterization that has since been conducted, and additional entropy stabilized systems that have been discovered.

2.1   Thermodynamics

The equation for Gibbs free energy is a convenient place to start when considering entropy as the dominant stabilizing factor in this materials system:

$$\Delta G = \Delta H - T\Delta S \tag{2.1}$$

At 0 K, the entropic term in this equation is zero, and the minimization of Gibbs free energy is based solely on the change in enthalpy. As temperature increases, the weight of the entropy term increases and there is a competition between the stabilizing thermodynamic factors. For a system to be stabilized by entropy, the configurational entropy value must exceed the enthalpy of mixing, stabilizing a single phase over any intermediate phases that can be predicted by the Gibbs phase rule [2]. The configurational entropy of a system is logarithmically related to Ω, the number of arrangements of atoms, or microstates within the system [2]. The number of microstates, and therefore configurational entropy, is maximized when there are equal amounts of the species present. For an oxide system with a cation and anion sublattice, the configurational entropy can be calculated by Eq. 2 [8]:

$$S_{config} = -R\left[\left(\sum_{i=1}^{N} x_i lnx_i\right)_{cation\ site} + \left(\sum_{j=1}^{M} x_j lnx_j\right)_{anion\ site}\right] \tag{2.2}$$

Where R is the ideal gas constant and x_i and x_j are the mole fractions of each constituent. In the (Mg,Ni,Co,Cu,Zn)O system, the anion sublattice has minimal contribution to the configurational entropy due to the presence of only one anion. For the five cations, the maximum

configurational entropy is 1.61 R, which exceeds 1.5 R, the minimum configurational entropy value necessary to be considered a high entropy material [8], [9]. At values above 1.5 R, the $T\Delta S$ term can overcome the enthalpy of mixing and dominate the free energy landscape. This does not guarantee that a single phase material will form, and intermediate phases may still be more favorable [8], but is a necessary condition.

As the number of constituents in a system increases, the maximum configurational entropy increases. The enthalpy of mixing also increases, but by a decreasing amount for each additional species. As the number of cations increases, the diversity of local cation sites is also increased due to the higher standard deviation of bond lengths and differing cation sizes. This allows for better incorporation of additional species, promoting the stability of higher component systems [10].

2.2 Background of the (Mg,Ni,Co,Cu,Zn)O Composition

In 2015, Rost *et al.* [2] reported that equimolar amounts of MgO, CuO, CoO, ZnO, and NiO form an entropy stabilized solid solution with a rock-salt structure when heated to temperatures between 850 and 900 °C. This was the first time there was a shift in terminology from materials being regarded as high entropy to entropy being the stabilizing thermodynamic factor. The components in this system were chosen because all the cations possess divalent states, allowing for variation of the relative cations while still preserving electroneutrality. Another motivation for choosing these components is the diversity in structures, with NiO, MgO, and CoO existing as cubic rock-salt structures, and ZnO and CuO as wurtzite and tenorite, respectively. These cations also provide diversity in cationic radii, electronegativity, and coordination in their parent structures. These cations were also chosen because there are pairs of binary oxides, such as MgO – ZnO and CuO – NiO, that do not possess significant solubility [2].

Rost *et al.* observed that upon heating the five constituent oxides to ≳ 700 °C, only two phases (rock-salt and tenorite) were detectable by x-ray diffraction (XRD). As the heating continued, the tenorite peaks disappeared and the full conversion to a single phase occurred within the temperature range of 850 to 900 °C. To test the reversibility of this reaction, shown below in Figure 2.1, a low temperature anneal of the single phase was performed at 750 °C, driving the transformation to a multi-phase system. Heating back up to 1000 °C returned the system to a single

phase, confirming the reversibility of the reaction, which is a requirement for entropy-driven transitions.
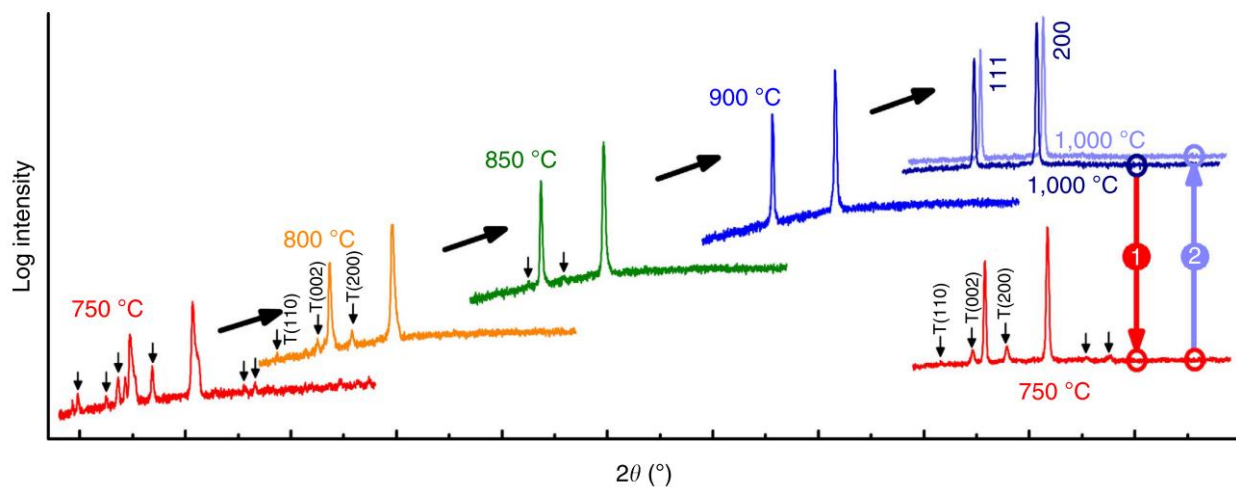
Figure 2.1   Schematic from Rost *et al*. seminal paper [2] demonstrating temperature dependence of XRD patterns for a single sample that was allowed to equilibrate for two hours at each temperature. The second phase, tenorite (T), remains until the scan at 900 °C and is shown to reversibly phase separate when the single-phase sample is annealed at 750 °C.

In the study by Rost *et al.*, it was also verified that as the relative cation amounts are varied from equimolar ratios, the transition temperature increases. Alterations in the stoichiometry reduces the number of atomic configurations and the configurational entropy of the system. Therefore, the increase in temperature supports the claim that the single-phase system is entropy stabilized. The solid-state transformation from the multiple phases to a single rock-salt phase is similar to melting. Confirming the endothermicity of the phase transformation further confirms that the (Mg,Ni,Co,Cu,Zn)O system's stability is dominated by entropy.

The homogeneity and random distribution of cations within the lattice was verified using more sensitive techniques than XRD to rule out the possibility of local clustering or segregation that would not change the global structure. Fitting of extended x-ray absorption fine structure (EXAFS) data shows that the cation-to-anion first nearest neighbor distances are nearly identical and that the local structures for each element are similar out to approximately the seventh nearest neighbor. Scanning transmission electron microscopy with energy dispersive x-ray spectroscopy (STEM EDS) images also revealed that each atom has a uniform spatial distribution on an atomic resolution.

5

2.2.1 Formation of a Single Phase

Upon heating the mixed binary oxides, the diffraction peaks associated with CoO and MgO are the first to broaden, between 650 and 725 °C, and merge together [6]. Over this temperature range, the intensity of the peaks associated with NiO, ZnO and CuO decrease in intensity, presumably as a result of interdiffusion [6]. It is important to note that during the heating, even if the precursor cobalt oxide used is CoO, peaks associated with the Co_3O_4 spinel phase appear at low temperatures and then disappear. After the NiO and ZnO peaks disappear, the tenorite phase, likely CuO with limited solubility of the other four cations, is the only remaining secondary phase after 800 °C [6], as can be seen in Figure 2.1 on page 5.

As ZnO and CuO do not naturally form rock-salt structures, it is reasonable to assume they would be the last to incorporate into the rock-salt solid solution. There is also an enthalpic penalty associated with the phase transformation of wurtzite to rock-salt for ZnO, of 25 kJ/mol, and of tenorite to rock-salt for CuO of 22 kJ/mol. Since the chemical potential of a species is related to the molar volume within a system, the maximum expected theoretical difference expected on mixing is around 15 kJ/mol [2]. In an ideal system, there would be no enthalpy of mixing associated with NiO, MgO, and CoO since these compounds naturally form rock-salt in their binary, parent structures. Differential scanning calorimetry (DSC) and thermogravimetric analysis (TGA) performed on the stoichiometric raw oxides by Rost *et al.* also reveal the completion of the formation of the single phase between 825 and 875 °C. The completion of the endothermic transformation is associated with a 12 ± 2 kJ/mol energy gain. There is also a small mass loss (~1.5%) due to the transition of the spinel intermediate phase to the rock-salt lattice [2], likely as Co^{3+} is reduced to Co^{2+}, which is associated with the evolution of oxygen.

2.2.2 Lattice Distortion

While the global structure of this entropy stabilized system is rock-salt with randomly distributed cations, additional EXAFS studies since the seminal paper by Rost *et al.* have shown that there is local variation in bond lengths between each cation and the neighboring oxygen atoms [11]. The second nearest neighbors for each cation, or the cation-cation pairs have a very uniform

distance, but the cation-oxygen bonds vary greatly showing that the randomness and difference in cation size is accommodated by the oxygen sublattice [11]. Density functional theory (DFT) calculations have also shown that as the system relaxes, the oxygen sublattice undergoes positional broadening, compared to the cation sublattice, which remains well-ordered [11].

Fitted EXAFS data reveal the bond lengths around the cations, where the coordination of these cations was assumed to be a six-fold, octahedral coordination. The bond lengths for Ni – O are 2.084 ± 0.005 Å, which is comparable to the bond length in rock-salt NiO [11]. Bond lengths for Co – O are smaller than that of a binary, rock-salt CoO, at 2.089 ± 0.009 Å and fall in between values for high and low spin states of Co [11]. The bonds for Zn – O cannot be compared to the binary ZnO system because ZnO does not naturally occur as rock-salt, but are smaller than the bonds in wurtzite ZnO at 2.078 ± 0.009 Å [11].

The local configuration around Cu^{2+} ions is different than that of the other cations. When fitting the EXAFS data, the scattering paths of the first coordination shell were split into two different lengths since the assumed six-fold coordination did not fit the data. The results suggested four planar bond lengths of 1.993 ± 0.007 Å and two axial bonds of 2.22 ± 0.002 Å for the Cu-O configuration. The geometry and bond lengths are consistent with the Jahn-Teller distortion that is often seen in Cu^{2+} in an octahedrally coordinated system [11]. In octahedral complexes of transition metals, ligand-field splitting often results in the splitting of the d orbitals and a degenerate ground electronic state [12]. This distortion, either by the contraction or elongation of the axial bonds, eliminates this double degeneracy and reduces the overall energy in the system. Simulated systems reveal similar bond lengths for this observed elongated geometry with contracted equatorial bonds of 2.05 Å and two elongated axial bonds of 2.30 Å [12]. A smaller subset of compressed octahedra are also observed. The orientation of these distorted polyhedral appear random and the distorted bond lengths require compensation within the anion sublattice, and likely the polyhedra of other cations [12]. This reveals ways in which the bonding and lattice change and distort in order to preserve the configurational entropy. While the Jahn-Teller distortion occurs to reduce the degeneracy of the copper d orbitals, reducing the energy of the system, it locally distorts the oxygen sublattice and this tetragonal distortion around these ions is in competition with the regular octahedral geometry of the other four cations.

The same DFT studies and classical potential simulations reveal that there is a slight tendency toward the formation of Cu^{2+}- Cu^{2+} pairs within the lattice [10], [12]. Classical potential

simulations show that there is an energy decrease with the formation of Cu^{2+}- Cu^{2+} pairs and a slight energy increase associated with the formation of Cu^{2+}- Zn^{2+} pairs [10]. DFT studies have shown a tendency for clustering of Cu^{2+} ions in the stoichiometric compound, that increases when the copper concentration is further increased [12].

Field emission scanning electron microscopy (FESEM) EDS, conducted by Hong *et al.,* of samples quenched from 900 °C, shows no evidence of cation segregation [6]. However, (transmission electron microscopy) TEM images of the same sample show nanoscale defects within the grains of the rock-salt material. Elemental analysis of these samples shows that the defects are copper rich, despite XRD indicating these samples to be a rock-salt with no additional phases present [6].

2.2.3 Altered Compositions

As the number of components increases, the configurational entropy of the system also increases. Attempts at adding a sixth element into the system with aliovalent substitution of dopants of 3+ or 4+ valency resulted in systems containing a secondary phase upon heating to 1000 °C, despite these dopants all existing regularly in octahedral coordination. There has been success with the partial substitution of Li^+ in the (Mg,Ni,Co,Cu,Zn)O system [13]. The addition of Li^+ up to 16.6%, where each of the six cations exist in equimolar amounts in the sample, was achieved where the increase in lithium concentration resulted in the decrease of lattice parameter in accordance with Vegard's law. This decreasing lattice parameter reveals that the Li^+ ions are substituting cation sites, rather than occupying interstitial sites, where the lattice parameter would increase instead [13]. In these systems, x-ray photo spectroscopy (XPS) was conducted on the (Mg,Ni,Co,Cu,Zn)O composition, revealing that all the cations were in a 2+ valence state. XPS revealed that the increase of Li^+ is accompanied by the presence and increased intensity of the Li (1s) peak, as expected. As the Li^+ concentration increases in the system, the Mg (1s), Ni (2p), Cu (2p), and Zn (2p) spectra remain unchanged, but there is a decrease in the intensity of the peaks associated with cobalt in a 2+ valence state and a shift toward a lower binding energy, characteristic of Co^{3+} [13]. This shows that the compensation mechanism within the system for the presence of 1+ ions is the formation of 3+ ions by oxidizing cobalt. To confirm this, Berarden *et*

al., also removed one of the five original ions completely, Zn, and formed a single phase from the composition $(MgNiCoCu)_{0.8}(LiGa)_{0.2}O$, where the Li^+ is compensated by the presence of Ga^{3+}, showing that the divalent cations can be completely substituted with a combination of 1+ and 3+ cations to charge balance the system [13]. Other groups have achieved success synthesizing a single phase of (Mg,Ni,Co,Zn)O, without substituting other ions in to replace the fifth component [14], despite the reduction in configurational entropy.

Other compositions that are not based on the (Mg,Ni,Co,Cu,Zn)O composition but still inspired by the recent advent of entropy stabilized ceramics have appeared in literature. Oxide systems containing up to 7 equiatomic rare earth oxides, rather than transition metals [15] that form the fluorite $Fm\overline{3}m$ structures, result in materials with narrow band gaps [16]. Entropy stabilized oxides in a perovskite structure have been developed that form single phase solutions, where five different cations are incorporated on the B site in the ABO_3 structure [17]. Non-oxide materials, such as entropy stabilized hexagonal diborides [18], have also been investigated.

2.2.4   Materials Properties

Many interesting physical properties and potential applications for the (Mg,Ni,Co,Cu,Zn)O system have been reported. The thermal conductivity has been explored through experiments and simulations, showing that the five-cation system approaches the amorphous limit for low thermal conductivity. This is attributed to the disorder in the system resulting in local deviations from the ideal crystal structure [19]. Rather than the differing masses resulting in the low thermal conductivities, it is the stress fields associated with these atoms that significantly affect the simulated conductivity [20]. When a sixth cation is added to the system, the thermal conductivity drops further by a factor of two, past the theoretical amorphous limit, going against conventional understandings of thermal conductivities. Phonon scattering in this system is thought to be a result of the disorder in the atomic forces introduced by charge transfer [19], [21].

Mechanical testing on samples sintered under different conditions revealed that the highest mechanical properties occur for samples sintered at 900 °C, with a 95.6% density, optimizing the trade-off between grain growth and density. At this sintering condition, there is a strength of 323

± 19 MPa and an elastic modulus of 108 ± 5 GPa [6]. The strength decreased upon approaching full density as a result of the grain size reaching 10 μm [6].

Additional interesting properties have been reported in recent literature on the (Mg,Ni,Co,Cu,Zn)O system. Charge compensation mechanisms when doping with Li$^+$ ions lead to potential reversible lithium storage properties and provide conduction pathways for high ionic conductivity of Na$^+$ and Li$^+$ ions [22], [23]. The entropy stabilized system has also been reported as antiferromagnetic [24], possessing colossal dielectric constants [13], and presented as a possible CO oxidation catalyst with the addition of platinum [25].

CHAPTER THREE: PHASE FORMATION AND STABILIZATION

The rock-salt (Mg,Ni,Co,Cu,Zn)O formation was investigated by several methods to determine the calcining conditions required to form a single phase and the progression to a single phase from the precursor oxides. The stability of the single phase was investigated under different heat treatments to verify the reversibility of the reaction by forming a multi-phase system and by determining the conditions where peak broadening occurs within XRD patterns, suggesting local inhomogeneities within the system.

3.1   Methods

Batching:

The (Mg,Ni,Co,Cu,Zn)O composition material was synthesized using binary oxides purchased from Fisher Scientific: Zinc (II) Oxide (99.999%, AA1113718, 1314-13-2), Cobalt (II) Oxide (99.995%, AA4435414, 1307-96-6), Nickel (II) Oxide (99.99%, AA1081914, 1313-99-1), Magnesium (II) Oxide (99.998%, AA1080009, 1309-48-4), and Copper (II) Oxide (99.995%, AA1070014, 1317-38-0).

The starting oxides were all characterized using XRD and environmental scanning electron microscopy (ESEM) to confirm the phases present and to observe the particle size and morphology. The nickel oxide and zinc oxide were crushed using an alumina mortar and pestle to break up the large agglomerates prior to mixing. The other chemicals were used as received. The Cobalt (II) Oxide was labeled as containing up to 10% Co_3O_4, so the relative amount of Co (II) and Co (II,III) were determined using XRD and the pattern was refined using GSAS II [26] to ensure proper batching.

Equimolar amounts of the cations were measured after drying the oxides in an oven at 200 °C to remove any physiosorbed hydration of the powders. The amounts of each oxide were measured to within one thousandth of a gram. These powders were then added to a 125 mL Nalgene bottle with 30 vol% 2 mm diameter, cylindrical yttria stabilized zirconia (YSZ) milling

media, reagent grade ethanol, and 3 drops of fish oil. A counterweight was prepared with another 125 mL bottle, media, and ethanol. The two Nalgene bottles were secured in a planetary mill and mixed at 375 RPM for 2 hours. After mixing, the powder suspension was poured from the Nalgene bottle into a Pyrex baking dish, rinsed with extra ethanol, covered with aluminum foil, and allowed to dry in a drying oven overnight at 70 °C. The powders were then mixed using a mortar and pestle to break up soft chunks and to reduce any segregation due to settling while drying.

Calcining:

The mixed oxides were calcined in batches of ~25 g in a double crucible set up, using two sets of alumina crucibles and lids to avoid furnace contamination from the potential volatilization of cobalt. The oxides were calcined in a drop-down box furnace using $MoSi_2$ heating elements and were heated at a ramp rate of 5 °C per minute to a temperature of 900 °C and held for 6-8 hours. The powder was air quenched from the calcining temperature of 900 °C, by removing the double crucible setup from the hot furnace. It is important to note that as the powders were loose, they were cooled within the crucibles, meaning that they did not cool as rapidly as if the sample had been able to be removed from the crucibles as well, as was done when quenching sintered pellets.

The rock-salt phase was verified using a PANalytical PW3040 X-ray Diffractometer with Bragg-Brentano geometry and Cu Kα incident radiation. Scans were conducted from 30 to 80° values of 2θ to verify the presence of a single, rock-salt phase. After seeing peak broadening of a few peaks (discussed later), some powders were calcined a second time with the same furnace profile to see if the peak broadening was resolved.

Annealing:

The thermal stability of the system was explored by slow cooling single-phase samples cooled in the furnace at 2 °C per minute after being held at a temperature above 870 °C. Additional samples were also held at lower temperatures ranging from 400 and 850 °C for various lengths of time after being verified as single phase following quenching from calcining or sintering. Temperatures within the tube furnace were checked using an external thermocouple in addition to the two present within the furnace.

Reduction:

Two-phase samples consisting of rock-salt and tenorite were treated under a reducing atmosphere with relative flow rates of 20 SCCM H_2 and 80 SCCM N_2. The samples were heated from room temperature to 650 °C over three hours, held at temperature for one hour, and then cooled to room temperature over three hours.

Hot stage XRD:

In situ calcining and annealing studies were conducted using the DHS 1100 stage within a PANalytical Empyrean X-ray Diffractometer with a graphite dome to improve homogenous heating. Samples were heated with a thin layer of platinum foil between the stage and the sample to prevent the sample from reacting with the stage. Experiments were performed in air and heating was done at the maximum ramp rate of 200 °C per minute.

Additional Techniques:

Several additional characterization techniques were conducted by Dave Diercks at the Colorado School of Mines. TEM images were obtained using a FEI Talos F200X TEM. Atom Probe Tomography (APT) was conducted using a LEAP 4000X Si with a 90 mm flight path, 12 pJ laser pulses with a 500-625 kHz pulse rate, detection rate of 0.5-1.8 ions per 100 pulses with a voltage rate of 2-7 kHz, at a temperature of 51.4 K.

3.2   Results and Discussion

Using the various techniques and methods discussed above, the single-phase formation and the reversibility of the reaction were confirmed. Additional temperature ranges were investigated revealing where the phase separation occurs as well as conditions under which chemical segregation occurs without a phase transformation.

3.2.1 Rock-Salt Formation

The mixed oxides were calcined at 900 °C to ensure that they were above the temperature required for the formation of a single phase, despite the inherent uncertainty associated with thermocouples and variation in actual furnace temperatures. As the system is stabilized at higher temperatures and the transition between multi-phase and single-phase states is a reversible, entropy-driven reaction, quenching is crucial for maintaining the metastable phase at room temperature.

XRD of the resulting powder after quenching, in Figure 3.1, shows that a single phase has been formed with a rock-salt structure. The peaks were indexed according to the assumed $Fm\bar{3}m$ space group of the rock-salt structure. The lattice parameter for the cubic structure was calculated to be 4.241 ± 0.005 Å, which is in good agreement with other sources that report 4.228 Å [13] and 4.237 Å [11].
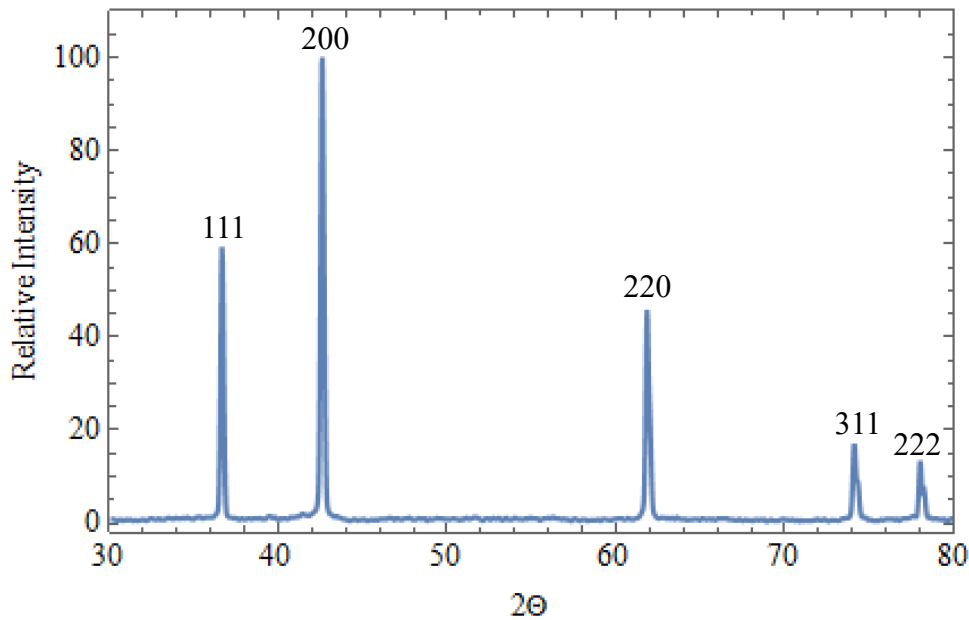
Figure 3.1 XRD pattern for powders calcined at and quenched from above 900 °C. Peaks are labeled for the rock-salt structure reflections.

A model of the (Mg,Ni,Co,Cu,Zn)O system was made in the modeling software Vesta, with oxygen populating the anion sublattice of the structure and a 0.2 occupancy for each of the

five cations on the cation sublattice. The calculated powder diffraction, shown in Figure 3.2, reveals the relative peak heights of the crystal and should have a maximum intensity from the (200) reflection. The experimental diffraction pattern shown above in Figure 3.1, on page 14, reveals a different peak height ratio and slight peak broadening, which will be discussed in section 3.2.4.
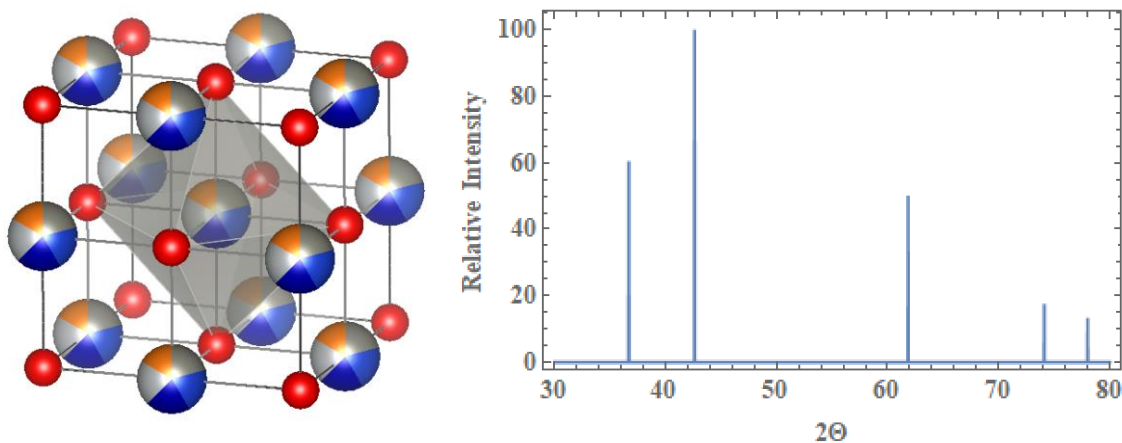
Figure 3.2   Simulated Vesta model for (Mg,Ni,Co,Cu,Zn)O structure (left) where oxygen (red) populates the anion sublattice and each cation is represented by 0.2 occupancy for each of the five cations, indicated by spheres of five colors. The calculated powder diffraction pattern from the model using Cu Kα radiation is shown on the right.

The molecular weight of this stoichiometric system is 70.18 g/cc and the theoretical density of the material is 6.12 g/cc. With the Vesta model, it is visible how each cation is in an octahedral coordination with the surrounding six oxygen atoms. The distance between these nearest neighbors in the ideal structure is 2.12 Å. The distance between nearest cations, or second nearest neighbors is 2.99 Å.

The coefficient of linear expansion (CTE) for this oxide system is approximately 1×10^{-5} K^{-1}. *In situ* XRD scans were conducted over a range of 30 to 80° in 2θ from room temperature to 750 °C. The lattice parameter was determined at four temperatures by averaging the calculated values from the (111) and (200) peaks. A linear fit of the lattice parameter versus temperature is shown below, in Figure 3.3, which was used to determine the CTE using the equation $\frac{\Delta L}{L} = \alpha_L \Delta T$, where α_L is the CTE, ΔL is the change in lattice parameter, L is the initial lattice parameter, and ΔT is the change in temperature from room temperature.
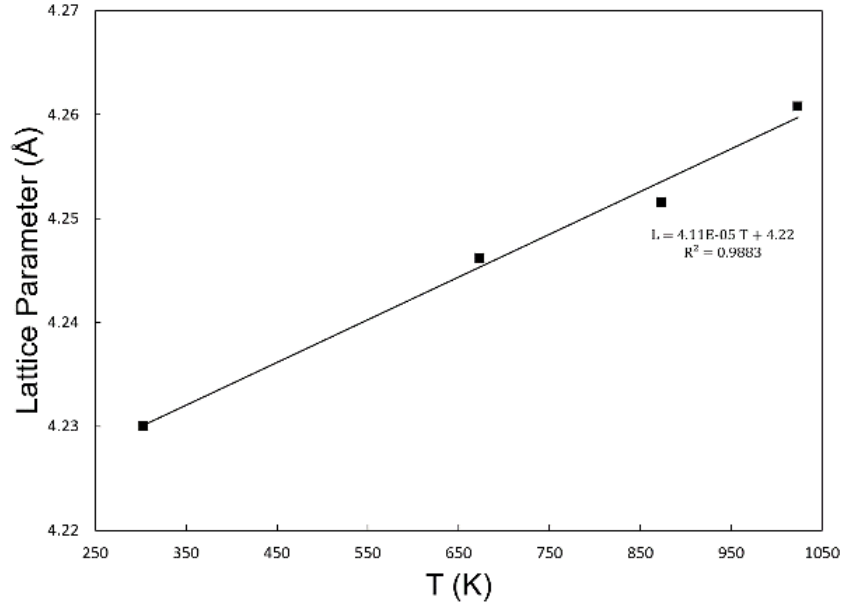
Figure 3.3   Linear fit of lattice parameter vs. temperature for *in situ* XRD data averaged from three diffraction peaks to calculate linear CTE.

3.2.2   Solid-State Reaction

Several experiments were conducted to study the progression from the five phases to the single phase. Initial experiments by Rost *et al.* demonstrated that during the formation of the single phase, the CuO tenorite phase is the last precursor to fully go into the rock-salt solution at around 875 °C through *ex situ* experiments where samples were equilibrated at different temperatures, quenched, and analyzed [2]. To verify that the mechanisms were similar and repeatable, several *in situ* experiments were conducted using various techniques to examine the progression from the mixed oxides to a single phase.

The *in situ* XRD experiment, shown below in Figure 3.4, demonstrates the initial stages of heating of the raw oxides. This plot shows that despite the raw oxides containing CoO, rather than Co_3O_4, as the sample heats, small peaks appear that are indicative of the formation of the Co_3O_4 spinel phase, indicated with arrows. This phenomenon was observed by Rost *et al.* and is confirmed in this experiment.
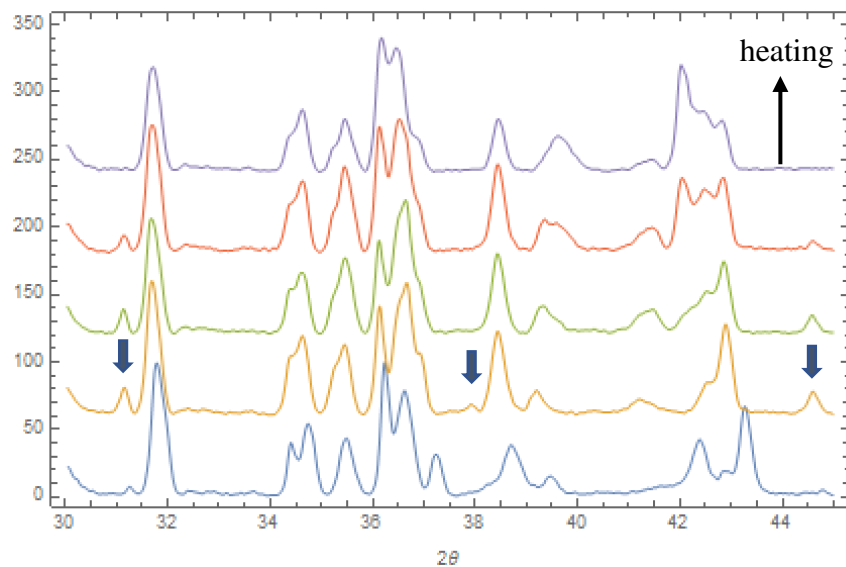
Figure 3.4   XRD patterns for *in situ* experiment where mixed oxides were held at 950 °C, confirming the transformation of Co^{2+} to Co^{3+} upon heating. Co_3O_4 peaks are identified with arrows.

An additional *in situ* XRD experiment, shown below in Figure 3.5, on page 18, was conducted by holding the mixed oxides at 1000 °C using the same heating stage. Initial room temperature scans from 30 to 44° values of 2θ show that there are many peaks present, attributable to the different starting oxides. By the time that the sample has reached 1000 °C, the peaks present have already changed drastically. Each scan was 20 minutes long, meaning that the reaction was still progressing throughout the scan, giving poor time resolution for the reaction happening as the lower 2θ values are at a different time than the higher 2θ values. By the third scan at 1000 °C, the only peaks present are due to the entropy stabilized rock-salt phase and the tenorite phase, which is reported as the last phase to fully go into solution and the first phase to precipitate out when heat treated below 875 °C [2]. The small peaks at 31.6, 32.7, and 37.9° 2θ are due to the sample stage.

DSC and TGA measurements were carried out on the mixed raw oxide powders to further characterize the formation of the single phase. The powders were heated at a rate of 5 °C/min to examine the heat and mass flow associated with the phase transition and are shown in Figure 3.6 on page 18.

17
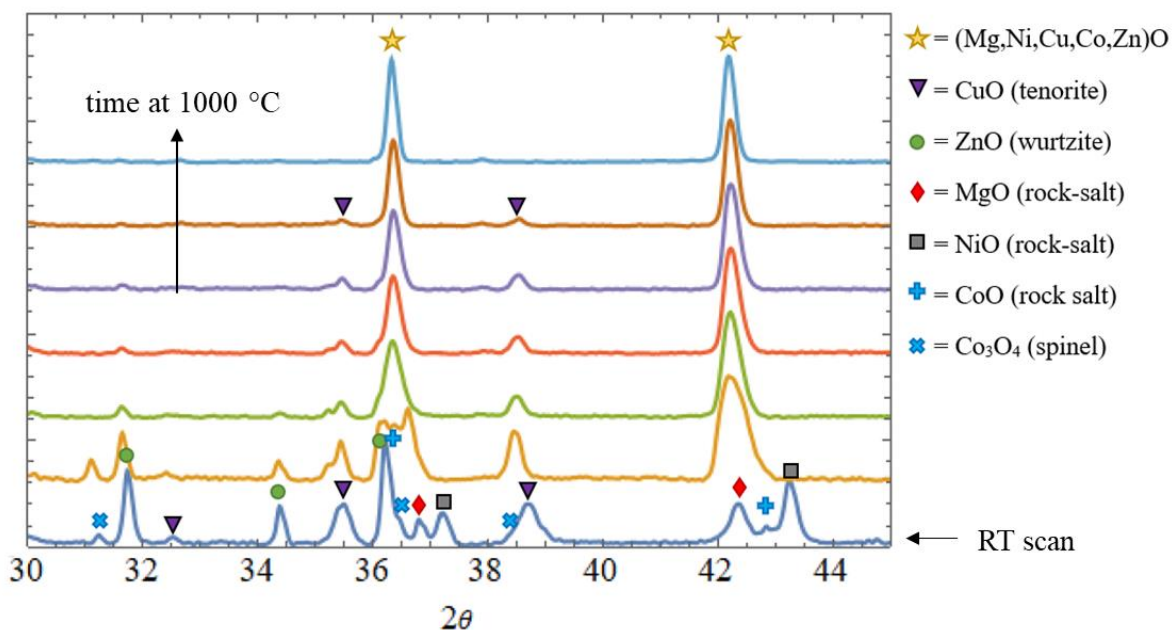
Figure 3.5   XRD patterns for *in situ* experiment heating mixed oxides to 1000 °C and holding, with Pt foil between the sample and heating stage.
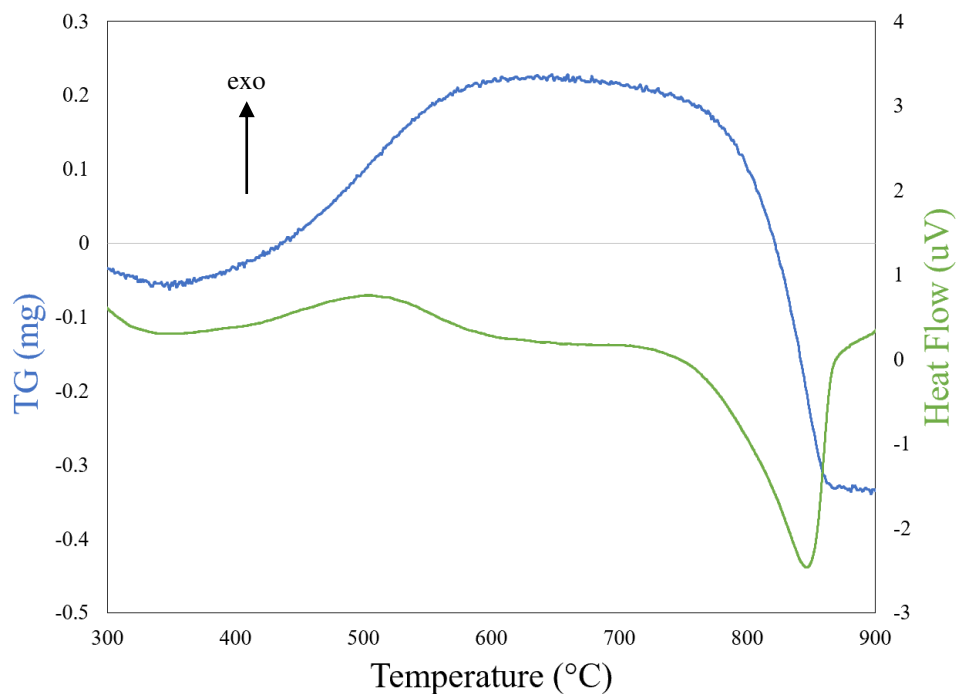
Figure 3.6   DSC and TGA data for heating raw mixed oxides under air at a rate of 5 °C/min, shown from 300 to 900 °C to highlight reactions.

From around 400 to 580 °C, there is a slight exothermic reaction accompanied by a mass gain. This is likely due to the reaction between the constituent oxides as they are reacting and forming a mixture of tenorite and rock-salt by about 600 °C. The sharp endothermic reaction accompanied by a mass loss from 750 to 870 °C is likely due to the final formation of the single-phase sample. This suggests that prior to forming a single phase, the stoichiometry of the various phases present contains more oxygen and at least one of the cations adopts a higher valency; once the single rock-salt phase has formed, all the cations adopt a valency of 2+. In the studies on the formation of a single phase from the precursor oxides, Rost *et al.*, suggests that an intermediate spinel phase involving Co^{3+} ions forms on heating [2]. As the same presence of a spinel phase has been observed on heating in *in situ* XRD experiments, it is likely that this mass gain from 400 to 580 °C is associated with the formation of an intermediate spinel phase, followed by the reduction of Co^{3+} to Co^{2+} resulting in the subsequent mass loss of oxygen from 750 to 870 °C. The reported precipitation of CuO, while reported over a similar temperature range, would not result in a mass change.

3.2.3   Phase Separation

While quenching from over 875 °C results in a single rock-salt phase, slow cooling or annealing the sample at temperatures between 600 and 875° C precipitates a copper-rich tenorite phase. This phase is the last binary oxide to go into the solid solution upon heating and the first to phase-separate upon heating to lower temperatures [2]. In addition to the rock-salt peaks, the additional peaks at 35.6 and 38.7, seen below in Figure 3.7, indicate the presence of the second phase in XRD. The structure of tenorite is confirmed through peak fitting of the XRD pattern. The two predominant peaks that are visible within the experimental data are representative of four peaks that are overlapping: (002) and ($11\bar{1}$) at 35.6° and (200) and (111) at 38.7° in 2θ.
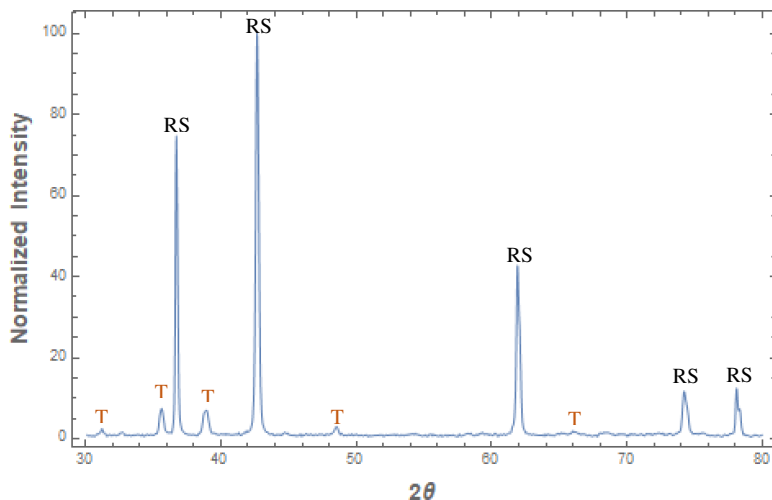
Figure 3.7   XRD pattern for a single-phase sample annealed at 750 °C for 30 minutes. Peaks are labelled as either the entropy stabilized rock-salt (RS) or the copper-rich tenorite (T) phase.

Vesta was used to examine the tenorite CuO crystal structure and determine the powder diffraction pattern. Both the crystal structure and XRD pattern are shown in Figure 3.8 below.
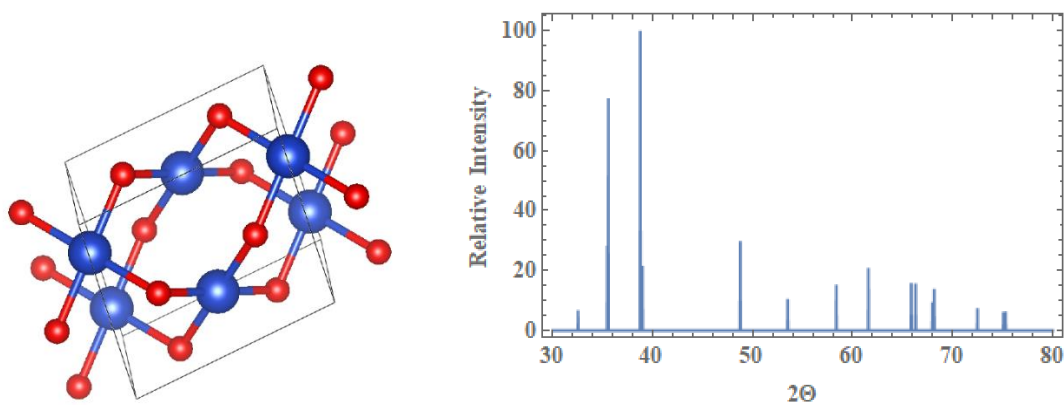
Figure 3.8   Vesta model for tenorite CuO (left) where oxygen is red and copper is blue and calculated powder diffraction pattern using Cu Kα radiation (right).

The reversibility of the formation of a single-phase and phase separation was confirmed and the data is shown below in Figure 3.9. Lower temperature anneals of a single-phase sample result in the precipitation of the tenorite phase. Subsequent high temperature treatments result in

20

the formation of the single-phase solid solution, confirming the work conducted by Rost *et al.* where the reversible reaction confirms the entropy stabilization of the rock-salt phase.
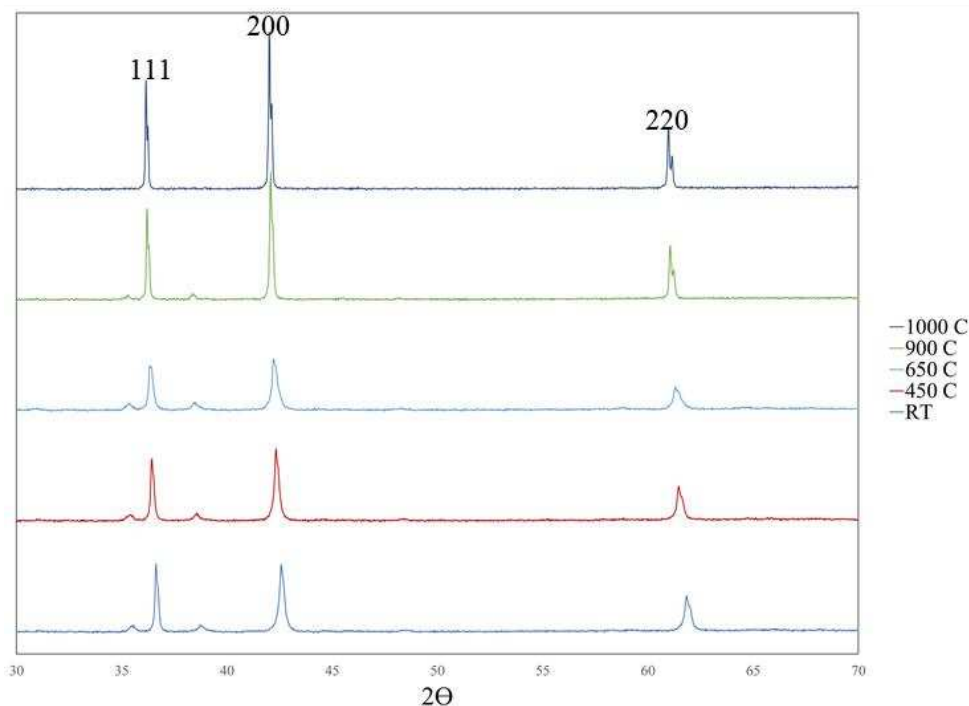
Figure 3.9   XRD patterns for *in situ* experiment confirming the reversibility of the formation of the tenorite phase.

High angle annular dark field imaging (HAADF) and EDS line scans on a slow cooled sample, shown in Figure 3.10 below, with tenorite peaks present in XRD confirm that the tenorite phase visible in XRD is copper-rich. The rock-salt matrix consists of about 50% oxygen and close to equal amounts of the cations, as expected based on the equimolarity of the material system. The needle-like precipitates have a significantly increased concentration of copper and a decreased concentration of the other four cations within the system. From this image, it also appears that the orientation of the precipitates is not random but may have a particular orientation relative to the rock-salt structure. The line scans do not suggest any change in oxygen concentration within the precipitates, consistent with the copper valency of 2+ within tenorite copper oxide.
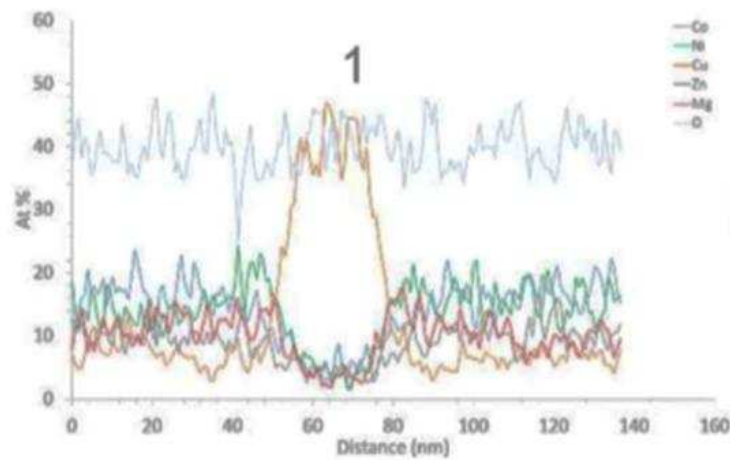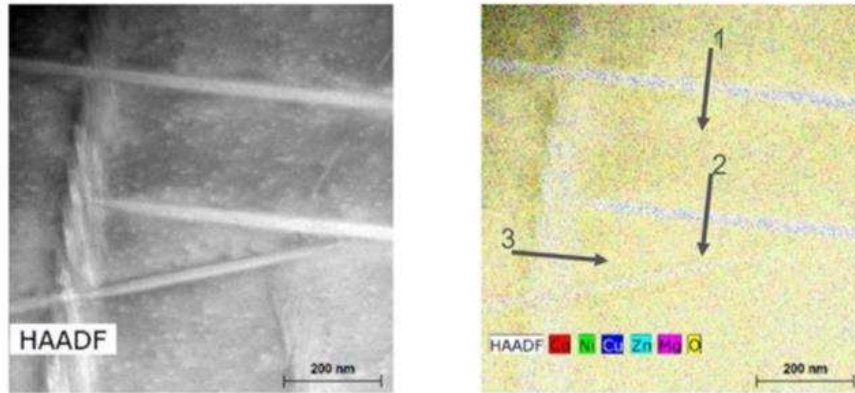
Figure 3.10   HAADF and EDS analysis of a slow cooled sample containing tenorite, where line scans reveal the chemistry of the precipitates relative to the rock-salt matrix.

APT reconstructions of the same slow cooled sample reveal that the "needle" shaped precipitates actually have a three-dimensional platelet structure. Similar to the TEM images, the APT reconstructions, shown below in Figure 3.11, also suggest that there may be a non-random orientation of the precipitates, as there appears to be a regular spacing of this secondary phase. It is suspected that this orientation of the platelets is along the (111) direction of the rock-salt lattice, which is supported by the proposed tetragonal distortion discussed in section 3.2.4.
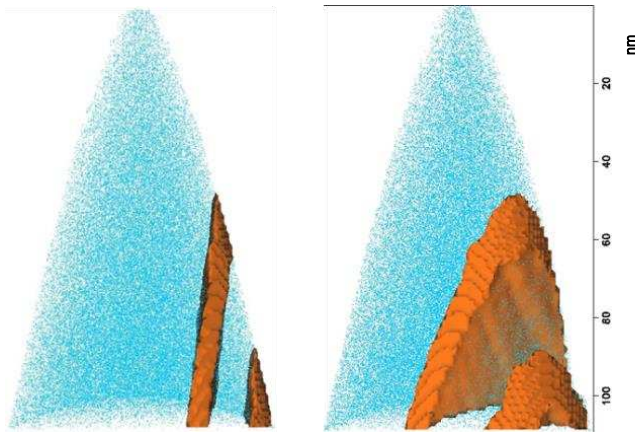
Figure 3.11   APT reconstructions of slow cooled samples revealing the 3D morphology of the tenorite precipitates.

When heat treated under a reducing atmosphere the CuO tenorite phase within the two-phase samples can be selectively reduced to form copper metal, while the matrix remains a rock-salt phase with a homogenous distribution of cations, as seen in Figure 3.12. There is no segregation seen by any additional cations, other than copper and oxygen. The successful reduction of tenorite provides an additional method of tuning the microstructure of the (Mg,Ni,Co,Cu,Zn)O system.
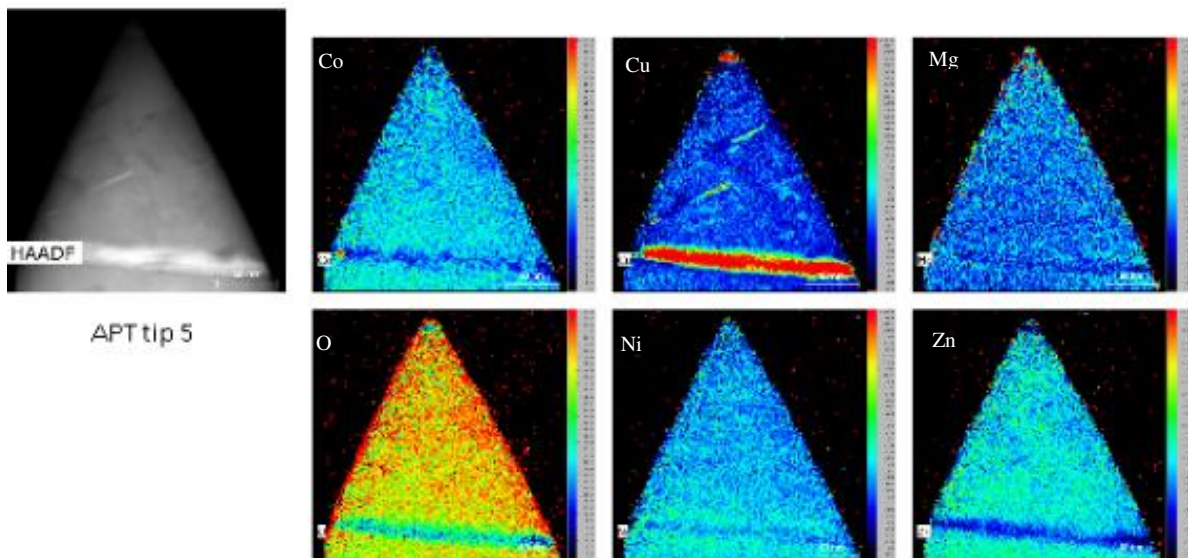
Figure 3.12   HAADF and EDS analysis of a two-phase sample treated under reducing conditions, revealing the successful reduction of copper oxide to copper metal without evidence of reduction or segregation of any of the other species.

23

HAADF and EDS reveal that the precipitate has a greatly increased concentration in copper content as well as a decreased concentration of oxygen, relative to the rest of the sample. In these images, warmer colors are indicative of an increased concentration of the species in question, indicated at the top left of each figure. The top, middle figure shows that there is a decreased concentration of copper outside of the needle-like precipitate and that the precipitate itself has a greatly increased concentration of copper. The other four cations are greatly reduced within the precipitate. The image for oxygen, on the bottom left, confirms that the concentration of oxygen has also been reduced within the precipitate, confirming that the reduction of the CuO precipitate was successful. XRD, shown in Appendix A, confirms that there is no tenorite within the sample, but instead reveals peaks identifiable as copper metal.

To understand more about the precipitation of the tenorite phase, *in situ* XRD experiments were conducted by heating a single-phase sample to conditions under which phase separation occurs. Scans were conducted from 33 to 44° in 2θ continuously throughout heating for 4.5 hours at a set temperature of 750 °C. Scans were three minutes long, providing higher resolution of the phase precipitation rate than longer scans would provide. Looking at a graphic of all the scans combined as a heat map, in Figure 3.13, it can be seen that as time progresses, peaks associated with tenorite become detectable.
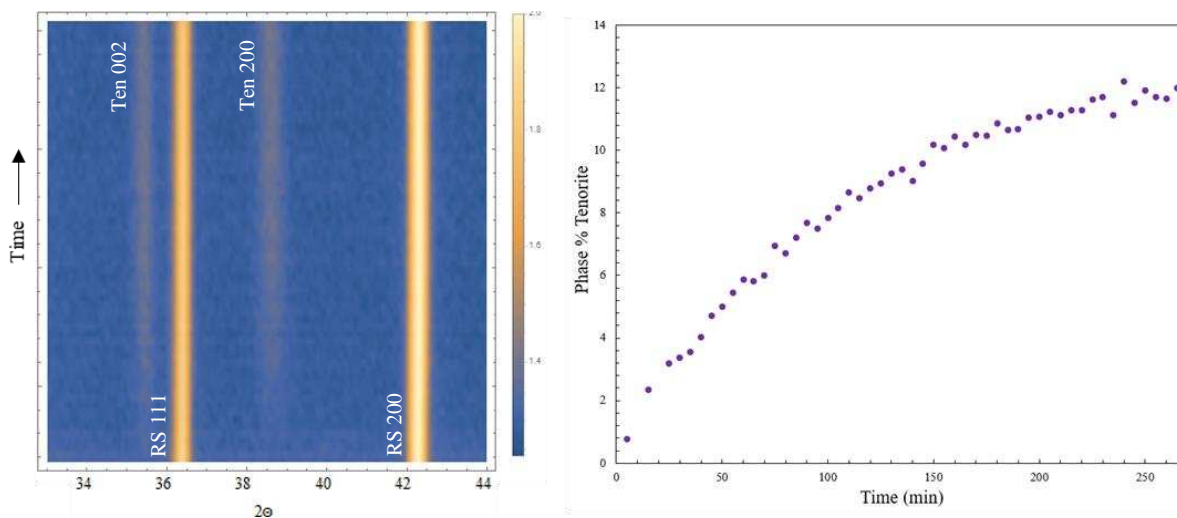
Figure 3.13   *In situ* XRD plots of single phase annealed at 750 °C (left) and a plot of wt% tenorite versus time for fitted XRD patterns (right).

24

Each of the scans was individually refined to achieve a wR <5% in GSAS II [26], and the phase percent for each scan was calculated and plotted to show the evolution of the tenorite phase as a function of time. At 750 °C, the precipitation of the tenorite is favorable and starts quickly. As the local concentration of copper is depleted within the rock-salt matrix, the formation rate of tenorite, seen as the slope of the curve, decreases. This suggests that the precipitation reaction is at least a 1st order transition and is dependent on the concentration of copper ions within the material system.

XRD scans of the sample after the 4.5 hour hold at 750 °C, shown in Figure 3.14, reveal that there are additional peaks present after the extended anneal beyond those of rock-salt and tenorite.
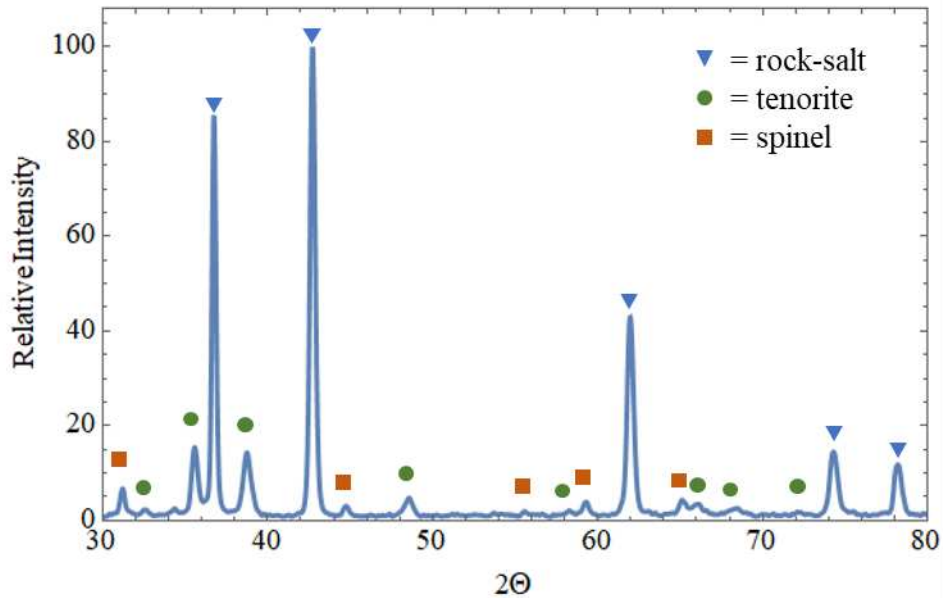
Figure 3.14   XRD pattern after *in situ* anneal revealing presence of rock-salt, tenorite, and additional spinel phase.

While the rock-salt, stabilized by configurational entropy, is stable at higher temperatures with a variation of up to ± 10% of each cation [2], once enough of the tenorite has formed and the copper is lost from the matrix, the rock-salt is no longer stable, and begins to phase separate further. These peaks were identified as a spinel phase, likely of Co_3O_4, which has been seen in the formation of the single-phase in *in situ* XRD experiments. This supports the observed mass gain and subsequent loss seen in the DSC and TGA data attributed to the valence change of Co^{2+} to

25

Co^{3+} with an associated gain in oxygen. After sufficient copper oxide has precipitated out of solution, and the rock-salt matrix is no longer stable, the spinel phase is detectable with XRD.

3.2.4   Peak Broadening

XRD patterns of single-phase samples quenched from different temperatures reveal different peak height ratios. In Figure 3.15, below, diffraction patterns from a sample quenched at 900 and one from 1000 °C are compared to the predicted diffraction pattern.
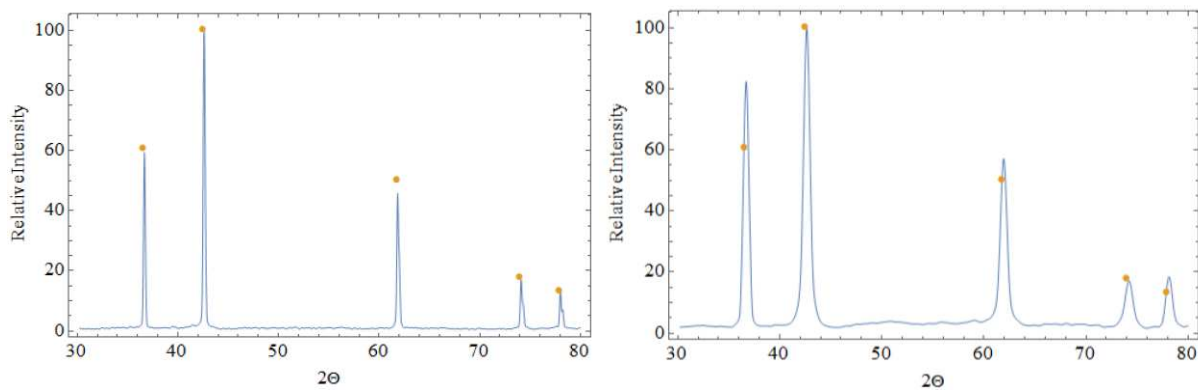
Figure 3.15   XRD patterns of two single phase samples quenched from 1000 °C (left) and 900 °C (right) compared to the predicted XRD pattern, shown by (•).

While the sample quenched from 1000 °C reveals a peak intensity ratio closer to that of the ideal pattern, the height of the (200) peak still appears shorter than the calculated pattern would predict. The diffraction pattern of the sample quenched from 900 °C not only reveals a further skewed peak intensity ratio, but also selective peak broadening that affects the (200), (220), and (311) peaks, while the (111) and (222) peaks remain sharp. While both temperatures are above the temperature required to form a single phase, this suggests that there may be some sort of lattice distortion without any detectable precipitation or second phase.

Low temperature anneals at temperatures between 600 and 875 °C have been shown to result in the precipitation of tenorite. Heating a single-phase sample from room temperature up to 700 °C reveals that at low temperatures, significant peak distortion is visible, as seen in Figure 3.16.
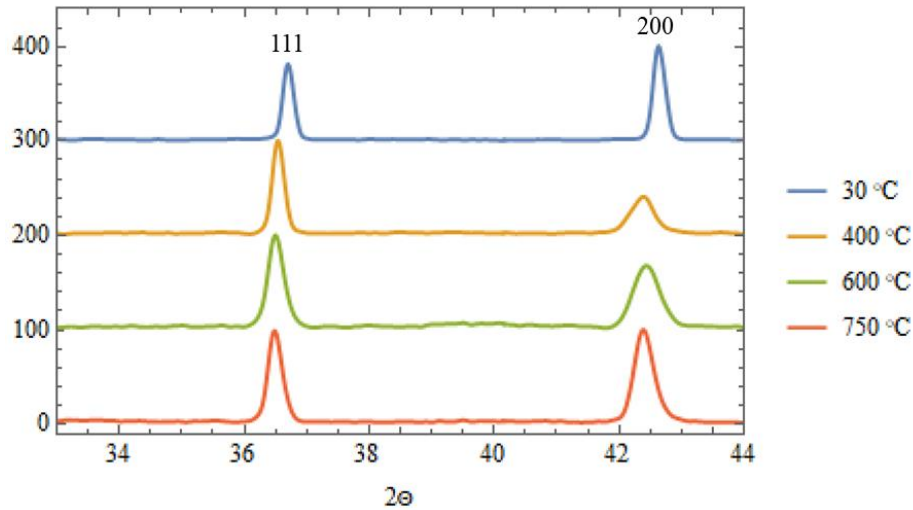
Figure 3.16 *In situ* XRD revealing the temperature dependence of the (200) peak broadening.

At room temperature, the (200) peak height is greater than the (111) peak height, as expected from the predicted powder diffraction pattern. At 400 and 600 °C, there is significant broadening, decreased peak height, and even asymmetric distortion to the (200) peak. By the time the sample reaches 750 °C, the distortion starts to resolve into a diffraction pattern closer to the ideal or starting peak height ratios. Berarden *et al.* reported similar asymmetric peak broadening between room temperature and the onset of phase precipitation that can be better indexed with a lattice structure adopting a slight tetragonal distortion. This would lead to the splitting of the (200), (220), and (311) peaks, leaving the intensity of the (111) and (222) peaks unaffected. In this situation, the (111) peak in the cubic system would correspond to the (101) peak in the tetragonal system, the (200) peak would split into (110) and (002) peaks in the tetragonal system, and (220) peak in the cubic lattice would split into the (200) and (112) peaks corresponding to the tetragonal system [27]. These diffraction patterns are presented in Appendix A.

Upon cooling of the same sample after being held at 750 °C for several hours to precipitate tenorite, there appears to be no distortion of the (200) rock-salt peak upon cooling, seen below in Figure 3.17.
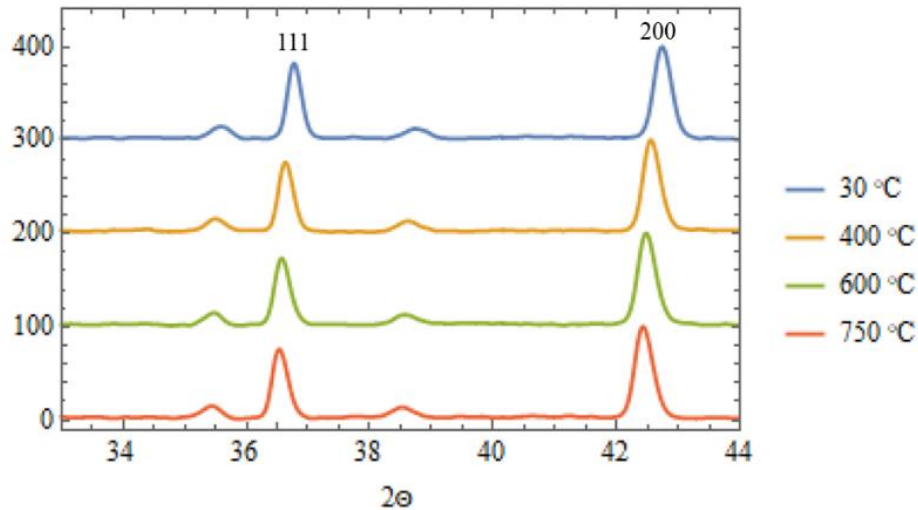
Figure 3.17   *In situ* XRD showing the lack of peak broadening after the phase separation of tenorite and no temperature dependence of the (200) peak height.

The peak height ratio of the (111) and (200) peaks remains relatively constant upon cooling. This suggests that with a reduced copper concentration within the rock-salt matrix, due to the increased copper concentration in the tenorite precipitates, that the peak broadening does not occur.

Berarden *et al.* explored the potential correlation between copper content in the rock-salt lattice and peak broadening, finding that if the copper concentration was increased to x = 0.26, even quenching from elevated temperatures to liquid nitrogen, rather than air, peak broadening still persists [27]. In the same study, they also found that the substitution of Cu^{2+} in the oxide system with charge compensating Li^+ and Ga^{3+} results in a temperature-independent diffraction pattern where the peak heights match the calculated XRD pattern and there is no peak broadening. Between the experimental results and the results presented in recent literature, it can be hypothesized that the copper ions within the system are related to the peak broadening and possible lattice distortion.

It was demonstrated in literature through experimental and simulated systems [12], [27], that the Cu^{2+} polyhedra undergo Jahn-Teller distortion, a tetragonal distortion around copper centers. This results in copper clustering being energetically favorable within the system and other simulations demonstrated that there was slight ordering present where distorted copper centers

28

were likely to be adjacent to other distorted copper centers. TEM EDS images by Hong *et al.* of a sample with acicular defects within a grain are shown below in Figure 3.18. The sample imaged was quenched from 900 °C, and although XRD revealed the sample to be single-phase, TEM imaging clearly reveals nanoscale defects [6]. These defects were shown to be copper-rich through TEM EDS, further suggesting that the segregation of copper occurs, even at temperatures where the global phase is still rock-salt.
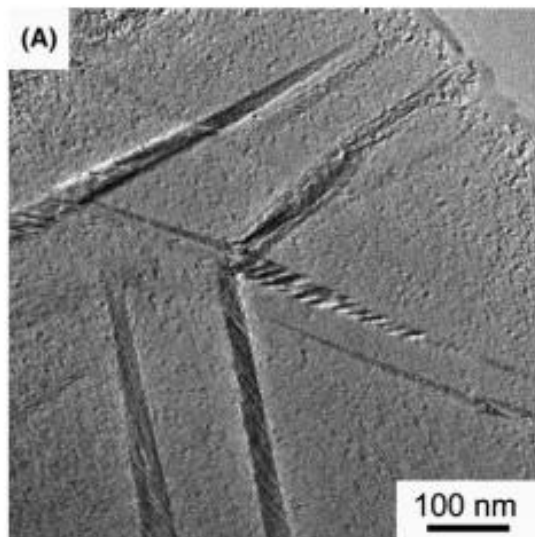
Figure 3.18   TEM images by Hong *et al.* [6] revealing nanoscale, copper-rich defects of a sample quenched from 900 °C, despite XRD revealing a single phase.

The morphology of these acicular defects appears similar to that of the tenorite precipitates in Figure 3.10 on page 21. There also appears to be similar, regular spacing to these features. It is possible that within these copper-rich clusters, the increased number of adjacent copper ions in a distorted octahedral coordination results in the displacement of the cations from their ideal lattice points. A schematic to illustrate this distortion of cations with increased copper concentrations is shown below in Figure 3.19. These regions of randomly oriented tetrahedral distortion would result in the peak broadening seen in XRD patterns.
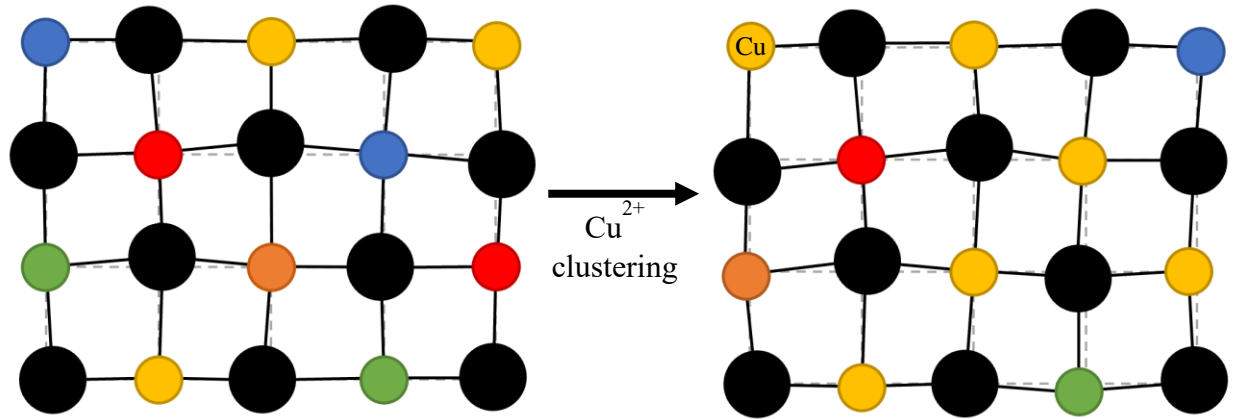
Figure 3.19 Schematic illustrating displacement of copper ions off of ideal lattice positions as a result of increased local concentration of copper ions.

The collection of experimental and reported findings suggest that at temperatures where the phase transformation to tenorite is not kinetically favorable, there is still an energetic benefit to the clustering of copper ions. At lower temperatures, below 600 °C, the clustering occurs due to diffusion of copper ions despite the tenorite phase transformation being kinetically hindered. At temperatures above 875 °C, the entropy stabilized rock-salt is the stable phase. However, at temperatures below 1000 °C the energetic benefit associated with clustering of copper is still able to compete with the entropy-driven homogenous mixing of cations. As the temperature increases further, and the $T\Delta S$ term is further increased, configurational entropy drives the random mixing of cations, resulting in decreased copper clustering. This hypothesis suggests that while the rock-salt phase is stabilized by entropy above 875 °C, there are still competing enthalpic mechanisms within systems containing copper that drive the segregation and clustering of these ions.

CHAPTER FOUR: SINTERING AND GRAIN GROWTH

The conditions under which sintering and grain growth occur were investigated in bulk samples with solid state sintering methods. Different thermal profiles were conducted with the goal of achieving microstructural control and to be able to obtain dense samples with a fine grain structure.

4.1   Methods

Milling:

Calcined powders were milled to reduce particle size using a planetary mill with 2 mm diameter spherical YSZ media, ethanol, and fish oil as a dispersant. Planetary mill speeds ranged from 350 to 500 RPM and times varied from 4 to 24 hours. All powder suspensions were dried in a drying oven over night to remove the alcohol and mixed using a mortar and pestle to break up clumps and remove any size segregation upon drying. Particle sizes and distributions after milling were analyzed using particle size analysis and ESEM techniques.

Green body formation:

Samples were sintered as cylindrical pellets that were formed using dies and a uniaxial carver press. Dies were either ¼", ½", or 1" in diameter. The dies used for forming were lubricated with a stearic acid in methanol prior to using. Pressures varied between 14 and 30 ksi. Pressure was maintained between 1 and 5 minutes before releasing the press.

After the green bodies were ejected from the dies, the green density was verified by weighing the sample and using calipers to determine the volume of the sample. Samples were sintered if the green density was above 55% of the theoretical density of the (Mg,Ni,Co,Cu,Zn)O system. If geometric densities were below 55%, a new sample was pressed at a higher pressure. If the higher pressure did not improve the geometric density of the green body, then it was assumed that there was a packing issue due to the particle size or morphology of the powder and milling was redone.

Sintering:

Pellets were sintered in a vertical tube furnace with the hot zone calibrated using an external thermocouple. Unless slow cooling was utilized for the purposes of phase segregation, all samples were air quenched by removing the sample from the hot furnace at temperatures above 900 °C. Due to the volatile nature of cobalt, all heat treatments were done in a double crucible set up where the first layer of insulation was a box made of platinum foil, to prevent reaction with alumina that was observed at temperatures above calcining temperatures through EDS measurements, and the outer layer was an alumina crucible and lid.

Characterization techniques:

Linear shrinkage was measured using dilatometry with a Netzsch Dilatometer 402. Constant rate heating experiments were conducted between 2 and 15 °C/min ramp rates to 1100 °C without an isothermal hold.

Images were collected using a FEI Quanta 600i Environmental Scanning Electron Microscope under high vacuum or low vacuum (0.75 Torr) with 20 kV and a 5.0 spot size using backscatter detection to examine the samples for porosity and grain size. Prior to imaging, samples were polished down to a 1 µm diamond polish and thermally etched for 40 minutes at a temperature 50 °C below the sintering temperature.

Densities of samples were obtained by either geometric density for samples with regular geometries or by Archimedes measurements for samples with irregular geometries. ESEM imaging was used to examine the porosity within the samples after sintering.

Grain sizes were quantified using ESEM images of polished samples. A variation of the line intercept method was used where three concentric circles with a known length were placed on an image, using ImageJ software, and intercepts were counted. For each sample, a minimum of 1000 grain boundary intercepts were counted across multiple images before combining to find the average grain size of the sample.

4.2   Motivation

In order to fully characterize the material properties of the (Mg,Ni,Co,Cu,Zn)O system, it is important to be able to achieve dense samples with controlled microstructures. Microstructural control involves being able to predictably tune grain size, sintered density, and the size and distribution of secondary phases, including pores [28]. Because all these factors can impact measured properties, such as mechanical and electrical properties, diffusion and sintering mechanisms should be understood so that they can be controlled. In most cases, desired microstructures are fully dense with fine grains, so determining adequate solid-state processing methods is crucial because generally there is a trade-off between densification and grain growth.

Original samples created by Rost *et al*. were determined to only be 75 and 80% of the theoretical density of the material system. Other groups, Berarden *et al.*, who sintered bulk samples for electrical characterization, reported densities of 75-80% by sintering for 12 hours in alumina crucibles at 1000 °C [4]. Field assisted sintering techniques (FAST) obtained samples that approached fully dense microstructures by sintering under 35 MPa in a vacuum. The advantages of this technique involve faster heating rates to minimize grain growth and enhanced densification due to the electric field [3].

4.3   Sintering

Pressed powder compacts were heated under various thermal profiles to achieve densification and sintering. The resultant geometric densities were determined and the microstructures were evaluated using ESEM techniques. For each sample discussed, additional ESEM images are presented in Appendix A to support claims made about the microstructural evolution.

4.3.1   Overview of Sintering

The driving force for sintering is the reduction of the total interfacial area in a powder compact, where solid – vapor interfaces are replaced with solid – solid interfaces, which reduces

the overall energy of the system [28]. Surface area, interfacial energies, and curvature gradients provide the thermodynamic driving force for sintering [29]. As diffusional processes involved in sintering are thermally activated, densification is typically increased at higher temperatures. These processes, such as the diffusion of atoms and vacancies, have an Arrhenius dependency on temperature [29]. Certain diffusion mechanisms, such as surface diffusion and vapor transport, are non-densifying mechanisms. These mechanisms also have an Arrhenius dependency on temperature, so it is important to control the temperatures of heat treatments to activate densifying mechanisms, such as grain boundary diffusion, instead.

Solid state sintering can generally be broken into three stages. During the initial stage, the green body loses up to 50% of its surface area as necks start to form between adjacent particles, and is associated with minimal coarsening of particle size and densification [30]. The initial stage of sintering is accompanied by only around 3% linear shrinkage [29]. The intermediate stage of sintering involves an increase in the neck size, between 1/3 and half of the particle size, the onset of particle coarsening, and the rounding of pores. The pores are still tubular and interconnected, so the sample is not yet hermetic. The intermediate stage corresponds to relative densities of 70-92% of the theoretical density [29], [30]. The final stage of sintering starts when the sample is about 92% dense and involves the final closure of pores, minimal additional densification, due to the reduced driving force for sintering, and significant grain coarsening [30]. Sintering only continues as long as the rate of surface area annihilation exceeds that of grain boundary annihilation [29], so as coarsening begins, the driving force for densification is greatly reduced.

There are several variables that can be controlled to alter the resulting density and microstructure of a sample after sintering. The materials variables that can be controlled are the variables related to the raw materials itself, such as the powder (shape, size, distribution and the agglomeration of particles) as well as the chemistry of the material (composition, homogeneity, and presence of impurities). Processing variables that can be controlled include the pressure of forming, temperature, time, atmosphere, and heating and cooling rates [28]. Many sintering attempts were conducted by altering the different variables that can impact densification and grain growth, showing that while the (Mg,Ni,Co,Cu,Zn)O system can be densified, much of the system is not understood and densification is therefore not easily controllable.

4.3.2 Optimizing Green Density

The density of a green body is crucial to the eventual density of the sintered body. When the green body starts with a higher density, closer to that of the final theoretical density of the material, it means that less shrinkage is required throughout the heat treatment process to obtain a dense sample. The primary factors that will impact the density of the green body are the particle size and morphology of the starting powder, including the presence of particle agglomeration, and the pressure used upon forming the green body.

To obtain the best random packing fraction, it is important to have round particles with a distribution of particle sizes, so that the smaller particles can fit within the interstices of the larger packed particles. The particle size for powders used for sintering should be between 0.1 and 100 μm [29]. While a narrow distribution of small particles will allow for improved packing over a narrow distribution of larger particles, the small particles are more likely to form agglomerates which can lead to inhomogeneous packing [31].

Smaller particles have a higher surface area to volume ratio relative to larger particles, which means they are higher energy per unit volume. The driving force for mass flow during sintering, or the sintering stress, is equal to the surface energy divided by the particle size [30]. Powders of smaller particle size then have a much higher sintering stress due to increased surface energy and decreased particle size, leading to faster sintering and often at much lower temperatures. As a green body made from finer particles starts to sinter, there are also many more grain boundaries present, which are high defect regions. Grain boundary diffusion is a favorable method for atomic motion within sintering processes [30]. Two different powders, one just crushed by using a mortar and pestle, and another milled with a planetary mill were analyzed for linear shrinkage using dilatometry, shown below in Figure 4.1. In this plot below, it is visible that while both compacted powders achieve comparable linear shrinkage, the milled powder begins to densify at a much lower temperature, exhibiting notable shrinkage at 750 °C, whereas the powder that has not been milled starts to rapidly densify at nearly 1100 °C.
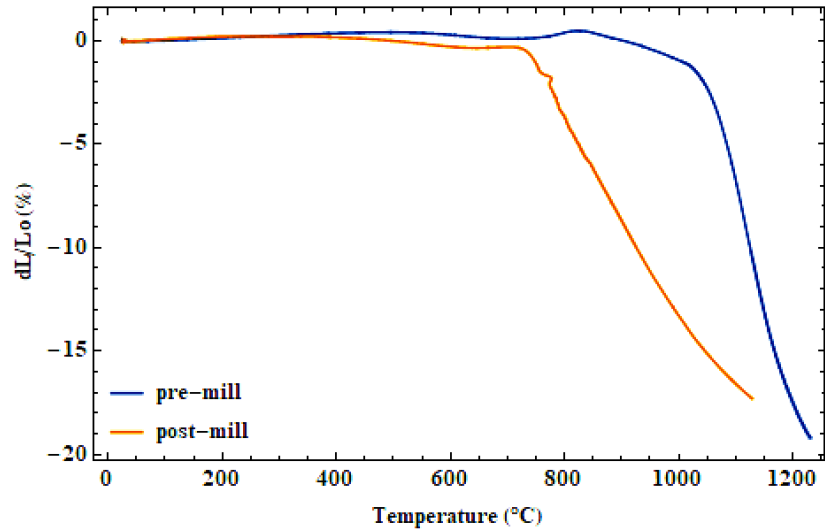
Figure 4.1   Dilatometry of calcined powders of two different particle sizes at a ramp rate of 5 °C/min.

This confirms that the reduction of particle size is an adequate way to speed up sintering [31]. What is interesting to note, is that the phase transformation from the two-phase powder to the single-phase rock-salt system occurs above 800 °C, and densification for fine milled powders occurs at a lower temperature than the phase transformation. This has the potential to lead to inhomogeneity within the compacted powder upon sintering which can lead to stresses within the system that may prove difficult to work with.

Another factor to control when optimizing the green density is the load under which the green bodies are compacted. While 14 ksi, or approximately 96 MPa, is often considered a broadly effective load for compacting green bodies in a uniaxial press, the optimal die pressure will vary for different samples, dies, etc. If too low a load is used, there will still be larger voids and reduced packing between the powders. If too high of a load is used, upon releasing the die, the sample can expand as a result of being too strained. This can result in visible "c" shaped cracks in the sintered sample and horizontal delamination in the green body, or springback effects.

Four samples were prepared from the same powder and sintered under the same thermal profile of ramping from room temperature to 970 °C at a constant 5 °C/minute ramp rate, an isothermal hold at 970 °C for 8 hours, and then air quenching to room temperature. All four samples were sintered at the same time to ensure identical furnace conditions and timing. A fifth

36

sample was prepared under a load of 14 ksi and did not hold together well after being expelled from the die, suggesting that this was too low of a load. The other samples were pressed at 18, 21, 25, and 28 ksi and the resultant micrographs are shown below in Figure 4.2.
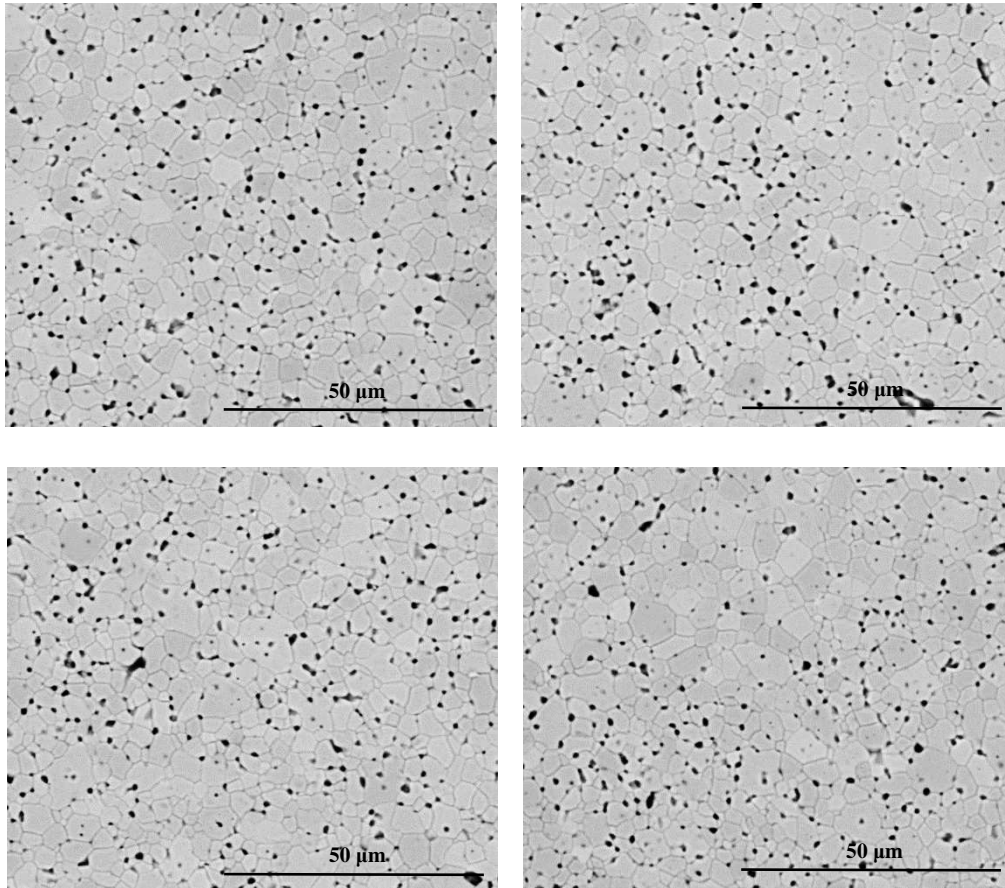
Figure 4.2   ESEM images of four samples sintered at 970 °C for 8 hours after a 5 °C/min ramp rate, where green bodies were pressed to 18, 21, 25, and 28 ksi (from left to right, top to bottom).

The above images show that there is not a significant difference in the resultant microstructure post sintering. The porosity in all four of these images suggest that the thermal profile is not ideal for sintering to full density in this material. The samples pressed at 18 and 21 ksi show similar grain and pore size and distribution. The samples pressed at 25 and 28 ksi start to show less of a homogenous microstructure. Regions of higher density are visible in the sample pressed at 28 ksi, suggesting that some inhomogeneous spring back was seen in the green body, which is supported by the macroscopic "c" shaped cracks within the sample.

37

4.3.3   Heating Schedules

For solid state sintering methods, there are an infinite number of variations on thermal profiles that can be applied to sintering, by altering ramp rates, isothermal hold temperatures, number of holds, and more.

Dilatometry allows for the monitoring of linear shrinkage of the compacted powder as a function of temperature and time. Assuming that densification is isotropic in a powder compact, the linear shrinkage can be extended to a rate of volume shrinkage, and the rate of densification with respect to time can be determined. Dilatometry was conducted on a single-phase milled powder sample at three different ramp rates to determine how the ramp rate affected densification and to identify an ideal temperature for isothermal holds, shown below in Figure 4.3.
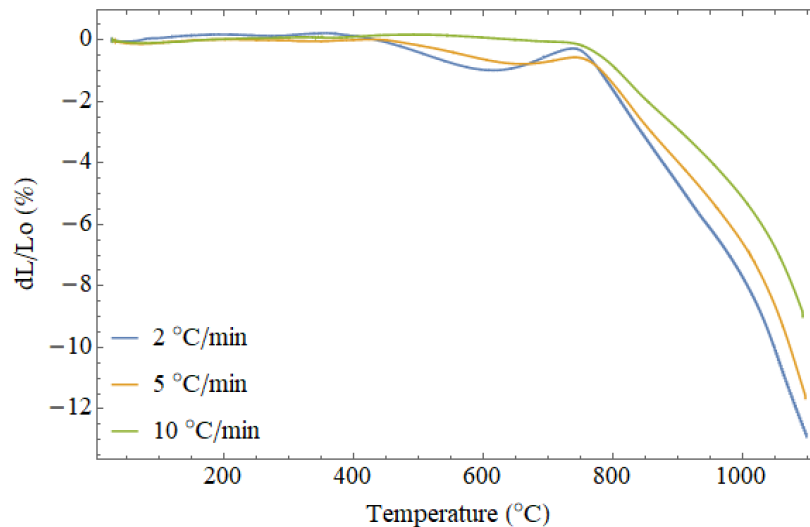
Figure 4.3   Dilatometry of the same powder heated under three different ramp rates, 2, 5, and 10 °C/min.

The derivative of these plots would provide the rate of densification, and the maximum slope of the dilatometry plots would suggest the temperature where the sintering rate is the highest. An ideal starting point for isothermal sintering temperatures is often slightly above this temperature of the maximum densification rate, where densification will occur without excessive grain growth [31]. This isothermal sintering temperature should be as low as possible to avoid coarsening but be high enough that sintering still can occur within a reasonable time frame [31]. For all three of these ramp rates, the plot reveals similar trends once densification takes off: the

38

magnitude of the slope increases, and inflection points can be seen around 900 °C for the three ramp rates. However, after the samples reach 1000° C, the magnitude of the slope increases yet again, suggesting that in this material, there are two distinct temperature regimes where different mechanisms dominating densification are active: the first, from 750 to 1000 °C, and the second above 1000 °C.

Another noteworthy feature about the plot in Figure 4.3 on page 38 is in the temperature range of 450 to 800 °C. The 10 °C/min ramp rate is essentially flat and featureless in this temperature range, but the 2 and 5 °C/min ramp rates reveal shrinkage to about 650 °C followed by expansion. This phenomenon is more evident in the 2 °C/min sample than the 5 °C/min ramp rate. It is likely that this shrinkage and expansion is due to the formation of intermediate phases that occurs over this range of temperatures. The faster ramp rate of 10 °C/min does not allow enough time for any intermediate compounds to form.

Several isothermal hold temperatures were attempted after a constant ramp rate for sintering. After 5 °C/min ramp rates, isothermal holds were conducted for 8 hours at 900, 950 and 1000 °C and the samples are shown below in Figure 4.4.
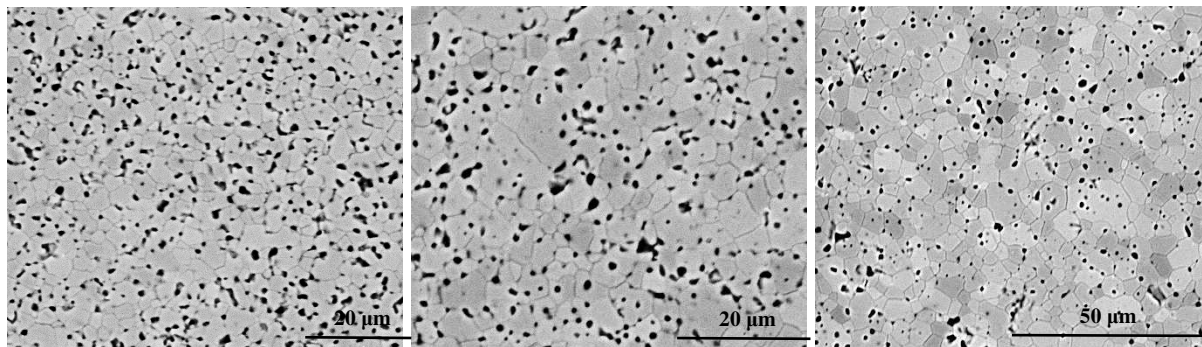
Figure 4.4   ESEM images of polished samples sintered at 900 (left), 950 (middle), and 1000 °C (right) after a 5 °C/min constant ramp rate.

The samples sintered at a temperature of 900 °C appear to still be in the intermediate stages of sintering, where pores have not completely rounded out and there is still a significant amount of porosity. The grain sizes are still quite small, representative of the starting particle size of a few micrometers. At the sintering temperature of 950 °C, the grains are significantly larger. While there is still significant porosity, both the grain and pore sizes have increased, indicative of the

sample progressing within the intermediate stage of sintering. At 1000 °C, the density is again slightly improved but still does not approach full density. In this image, the pores appear to have rounded, and there is evidence of high grain boundary mobility because of the porosity trapped within the grains. While higher temperatures lead to faster diffusion for processes that promote densification, they also lead to increased coarsening and activation of different diffusion mechanisms that can result in abnormal grain growth [31].

Additional isothermal hold temperatures were tested after a ramp rate of 2 °C/min. Slower ramp rates can allow for additional time at lower temperatures, which can lead to increased coarsening. Slower ramp rates also provide more time at temperatures that can result in densification and allows for the precipitation of tenorite and reformation of a single phase throughout sintering. These stresses associated with the different densities of the tenorite and rock-salt can potentially affect the resulting microstructure after sintering by creating areas of different stress that can lead to areas densifying at different rates [31]. Isothermal holds of 940, 970, 1000, and 1050 °C were tested after a 2 °C/min ramp rate, and microstructures are shown below in Figure 4.5.
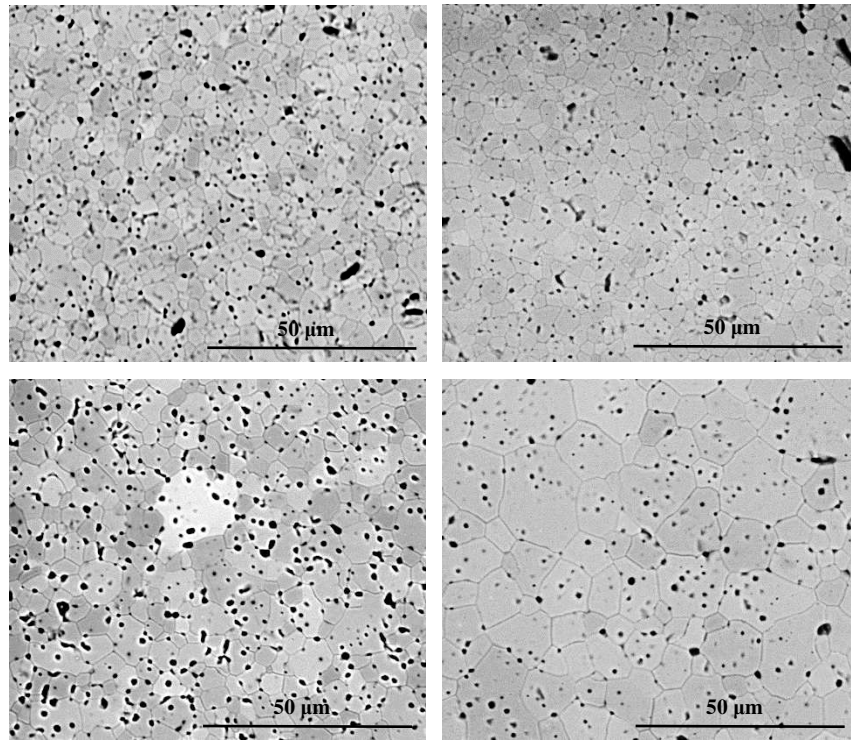

Figure 4.5   Four samples of isothermal holds at 940, 970, 1000, and 1050 °C (from left to right, top to bottom) after a 2 °C/min ramp rate.

40

A similar trend is observed after the 2 °C/min ramp rates: as the temperature of the isothermal hold increases, the density, grain size, and amount of trapped porosity increases. The samples sintered at 940 and 970 °C have a significant amount of porosity on grain boundaries and triple points. At 1000 °C, there is still porosity at the grain boundaries, but there is a significant amount of porosity within the grains, and a few have grown significantly more than the others. In the sample that was sintered at 1050 °C, almost all the porosity within the sample exists within the grains. At this temperature, especially after a slow ramp rate, the grain boundaries easily break away from the pores that pinned them at lower temperatures. For all these images, there appears to be more intragranular porosity than the samples after the 5 °C/min ramp rate, suggesting that the slower ramp rate does provide more driving force for coarsening and grain mobility that results in trapped pores.

With different isothermal holds after constant heating ramps not resulting in dense samples, several attempts at sintering were conducted with two stage ramp rates. Dilatometry showed two distinct temperature regimes that yield densification. The second regime, over 1000 °C has a steeper slope and therefore a more rapid rate of sintering. Thermal profiles were designed to ramp slowly up to 750 °C, the temperature of the onset of densification, and then quickly through the temperature range for this first densification regime to a final sintering temperature within the second temperature range, around 1000 °C. An example of this thermal profile is shown schematically below in Figure 4.6.
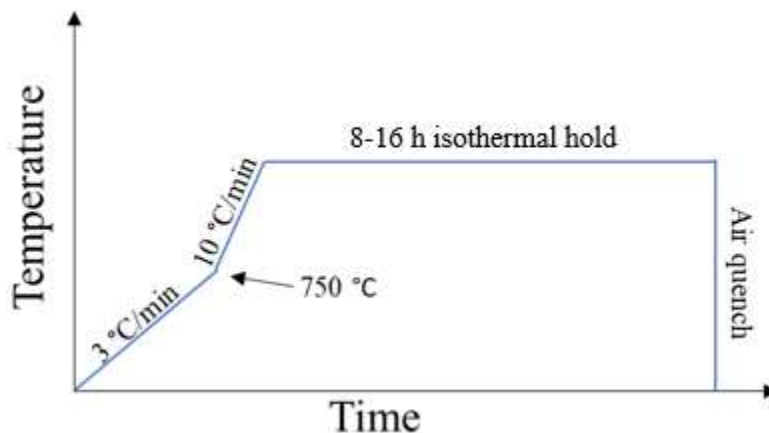

Figure 4.6   Schematic representation of heating schedules with a two-stage ramp rate and an isothermal hold.

41

These heat treatments, following a two-stage ramp rate, led to increased densification without excessive coarsening and trapped porosity. Samples were heated at a rate of 3 °C/min to 750 °C and then to a temperature of 940 or 970 °C at a rate of 10 °C/min, followed by an 8 h isothermal hold and air quenching. The micrographs for these samples are shown below in Figure 4.7.
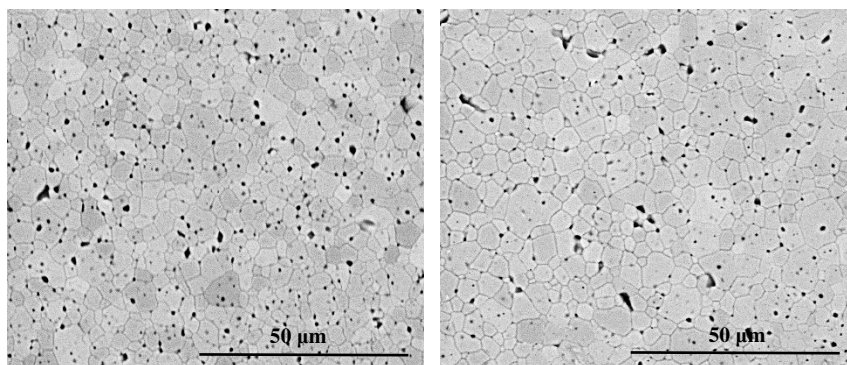

Figure 4.7   ESEM images of samples after two step ramp rates and an isothermal hold at 940 °C (left) and 970 °C (right).

While these samples still show porosity at the grain boundaries and triple points, this porosity is noticeably less than what is observed after sintering at these temperatures after a constant ramp rate. There also appears to be minimal porosity trapped within the grains, suggesting that these heat treatments better managed grain boundary mobility relative to pore mobility. Thermal profiles similar to these were investigated further in the following section on grain growth.

Cooling rates and chemistry were not altered in attempts to achieve densification. The samples were always quenched to ensure the metastable rock-salt phase did not undergo a phase separation. The stoichiometry of the system was also not altered because the goal was to sinter the equimolar system of (Mg,Ni,Co,Cu,Zn)O, not an altered composition. While most of the heat treatments were conducted in a tube furnace where one end of the tube was closed, some heat treatments were repeated in a tube with two open ends to promote airflow and potentially alter the atmosphere within the furnace. Concerning the phase separation of the powders when sintering, several samples were prepared starting with a powder that was already two-phase, rather than

single-phase. None of these alterations to the homogeneity of the sample or the sintering atmosphere led to changes from the previously reported heat treatments.

4.4   Grain Growth

After investigating heat treatments and ramp rates that resulted in increased densification, the optimal temperature for sintering was investigated. Varying the isothermal hold after a two-step ramp rate provided insight into the grain growth and resultant grain sizes after these different heat treatments.

4.4.1   Grain Growth Overview

Since densification and grain growth both involve similarly activated diffusion mechanisms and typically occur simultaneously, it is impossible to solely consider the kinetics of just sintering without grain growth. During initial stages of sintering, abundant pores are able to pin grain boundaries, preventing grain growth from occurring. Towards the end of the intermediate stage and during the final stage of sintering, grain growth increases rapidly once the density of the material reaches 85-90% of the theoretical density [31]. In simple ramp-and-hold thermal profiles, the temperature required for densification will also result in significant grain growth. There are techniques to avoid grain growth while still achieving full sintering, but they require improved understanding of temperature ranges of various diffusion mechanisms, which is not yet known for the (Mg,Ni,Co,Cu,Zn)O system.

The driving force for grain growth, similar to sintering, is the reduction of free energy within the system. While grain boundaries have lower specific energy than solid-vapor interfaces, the atoms at grain boundaries still have higher energy than that of the bulk of the crystalline grains [31]. The reduction in the surface area associated with grain boundaries is accompanied by a reduction in the free energy of the system. This process results in the growth of one grain at the expense of another. In normal grain growth, the sizes and shapes of the grains remain within a fairly narrow range, whereas abnormal grain growth is often characterized by the rapid growth of a few grains.

There is a high probability that pores will sit on grain boundaries, even during grain growth. This affinity between pores and grain boundaries reduces the overall grain boundary energy and the configurational energy of the system, essentially pinning the pore-grain boundary combination [29]. During the intermediate stages of sintering, the grain boundaries must drag the associated pores in order to move, which is why coarsening is minimal. If the grain boundaries are able to break away from the pores, and the pores end up within grains, it is almost impossible to shrink them further, and a porous sintered body results [29]. This behavior, where the increased grain boundary mobility allows the boundaries to break free from the pinning pores, can be indicative of too high of a sintering temperature and possibly of abnormal grain growth.

4.4.2   Grain Growth Study

To better understand the temperature and time dependence of the (Mg,Ni,Co,Cu,Zn)O microstructure and density, a combined sintering and grain growth study was performed. Samples were pressed and sintered under similar conditions from the same batch of milled powder. All samples were heated with the thermal profile represented in Figure 4.6 on page 41, from room temperature to 750 °C over four hours, then to their final sintering temperature at a rate of 10 °C/min. Final sintering temperatures varied from 950 to 1150 °C. At a given hold temperature, samples were either isothermally held for 8, 12, or 16 hours before being air quenched.

Samples held at a sintering temperature of 950 °C are shown below in Figure 4.8. From right to left, the average grain sizes of these samples are 1.87 ± 0.07μm (8 hour hold), 2.00 ± 0.16 μm (12 hour hold), and 2.27 ± 0.06 μm (16 hour hold). In these micrographs, there is still some porosity visible at triple points and grain boundaries, indicative of insufficient thermal energy to fully densify. The grain sizes of these samples reveal that the starting powder had a relatively homogenous distribution and fine particle size. As expected with normal grain growth, the grain size increases as the time of the isothermal hold increases.
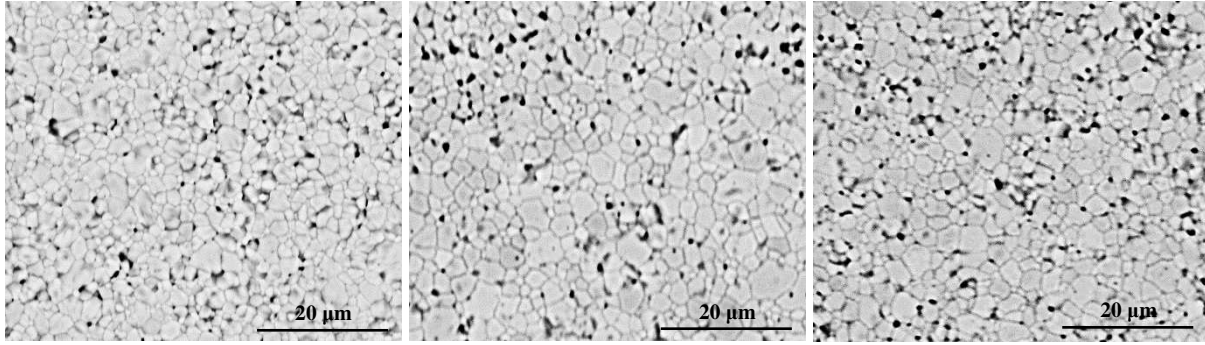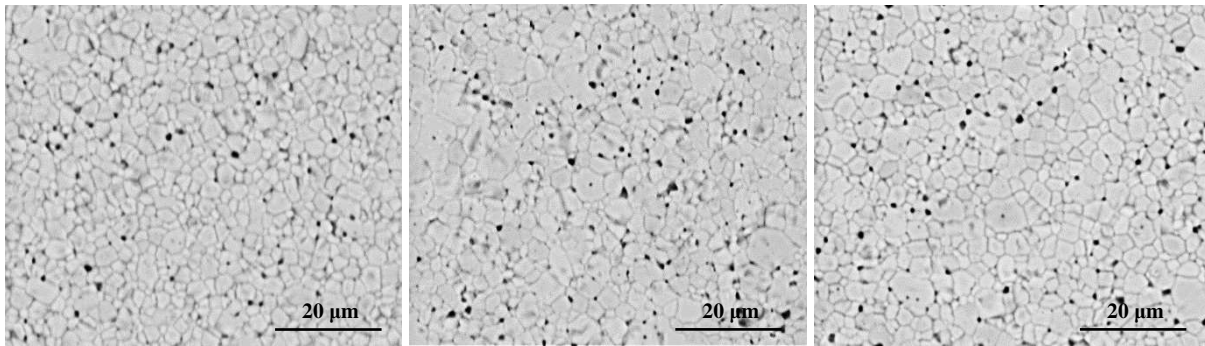
Figure 4.8   Samples sintered at 950 °C for 8 h (left), 12 h (middle) and 16 h (right).

The samples sintered at 1000 °C, seen below in Figure 4.9, have an average grain size of 2.38 ± 0.06 μm (8 hour hold), 2.59 ± 0.10 μm (12 hour hold), and 2.68 ± 0.12 μm (16 hour hold). These average grain sizes are larger than those of the samples sintered at 950 °C, consistent with normal grain growth. While some porosity remains at triple points and grain boundaries, the porosity is decreased from the samples treated at 950 °C.

Figure 4.9   Samples sintered at 1000 °C for 8 h (left), 12 h (middle) and 16 h (right).

The samples sintered at 1050 °C, seen below in Figure 4.10, have an average grain size of 2.99 ± 0.10 μm (8 hour hold), 3.29 ± 0.20 μm (12 hour hold), and 3.52 ± 0.09 μm (16 hour hold). The first noticeable feature of these micrographs is that the porosity is minimal and reduced from the samples sintered at 1000 °C. This suggests that under these conditions, 1050 °C is a suitable temperature for sintering after the two-step heating rate. Another notable feature is that there appear to be a few grains, especially visible in the center image, that appear abnormally large relative to the rest of the grains within the sample.
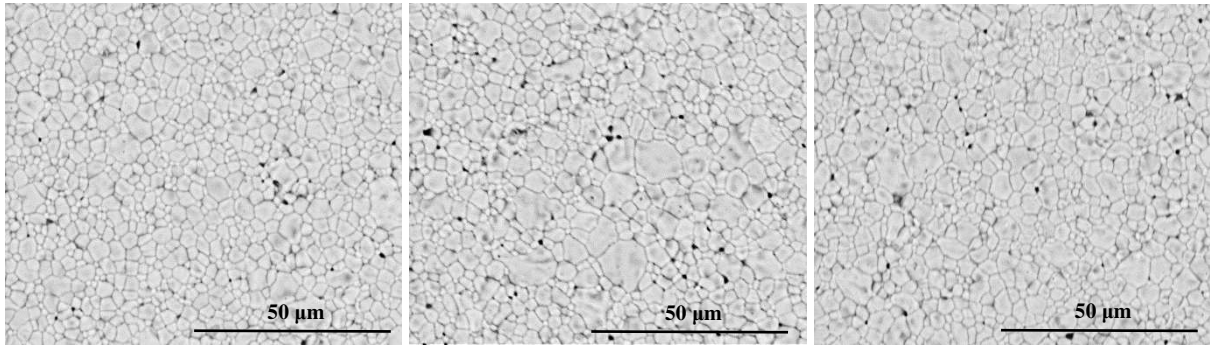
Figure 4.10   Samples sintered at 1050 °C for 8 h (left), 12 h (middle) and 16 h (right).

The samples sintered at 1100 °C, seen below in Figure 4.11, have an average grain size of 4.04 ± 0.14 μm (8 hour hold), 4.14 ± 0.12 μm (12 hour hold), and 4.35 ± 0.24 μm (16 hour hold). Similar to the samples sintered at 1050 °C, there is minimal porosity in these samples sintered at 1100 °C. There are still the occasional grains that appear abnormally large, relative to the rest of the image.
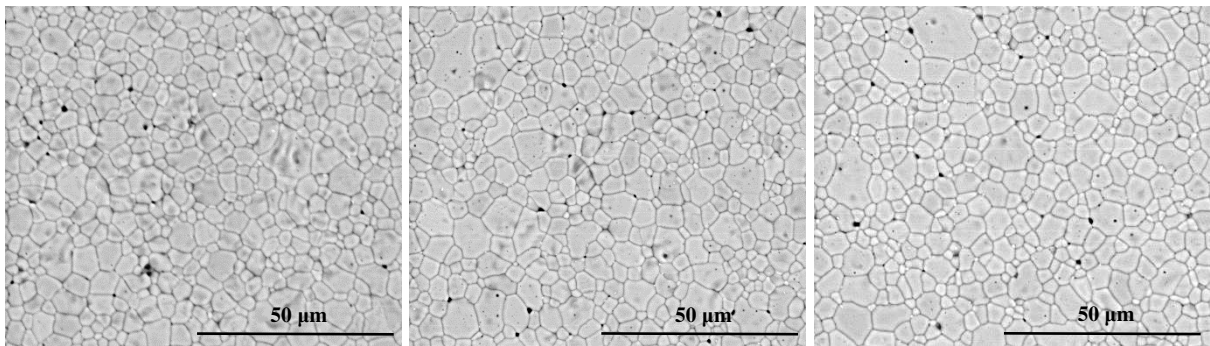

Figure 4.11   Samples sintered at 1100 °C for 8 h (left), 12 h (middle) and 16 h (right).

The final samples sintered at 1150 °C, seen below in Figure 4.12, have an average grain size of 7.38 ± 0.34 μm (8 hour hold), 7.60 ± 0.22 μm (12 hour hold), and 7.81 ± 0.21 μm (16 hour hold). The samples sintered at 1150 °C show potential signs of abnormal grain growth, where there appears to be some pores trapped within the grains. These trapped pores show that at 1150 °C, grain boundaries are able to break away from the pores, resulting in a less dense sintered body.

The average grain size at this temperature is significantly larger than the grain sizes of the other temperatures.
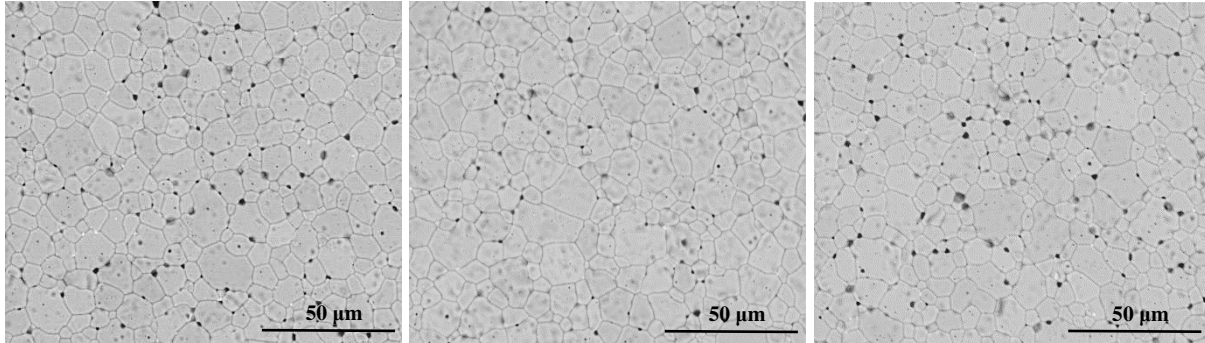

Figure 4.12   Samples sintered at 1150 °C for 8 h (left), 12 h (middle) and 16 h (right).

The resultant grain sizes for each sample are summarized in Table 4.1 below. If the system follows ideal grain growth behavior, the data should follow the equation of ideal grain growth, $D^2 - D_0^2 = Kt$, where D is the average grain size, D_0 is the initial grain size, t is the time at a given temperature, and K is a temperature-dependent constant.

Table 4.1   Tabulated grain size with 95% CI for samples sintered at different times and temperatures.

Temp (°C)	Grain Size (µm)		
	8 h	12 h	16 h
950	1.87 ± 0.07	2.00 ± 0.16	2.27 ± 0.06
1000	2.38 ± 0.06	2.59 ± 0.10	2.68 ± 0.12
1050	2.99 ± 0.10	3.29 ± 0.20	3.52 ± 0.09
1100	4.04 ± 0.14	4.14 ± 0.12	4.35 ± 0.24
1150	7.38 ± 0.34	7.60 ± 0.22	7.81 ± 0.21

The squared values of the average grain sizes were plotted against time for each isothermal temperature hold. If the material system follows ideal grain growth behavior, this should yield a linear plot for each temperature. Each of the tested temperatures yields a line with a relatively good linear fit for the three time points, seen below in Figure 4.13. The error bars on each point represent the 95% confidence interval (CI) for the grain size at each point. The error around the grain sizes

47

for the higher temperatures are larger, which is not consistent with ideal grain growth, where there should be a relatively similar size distribution of grains throughout sintering.
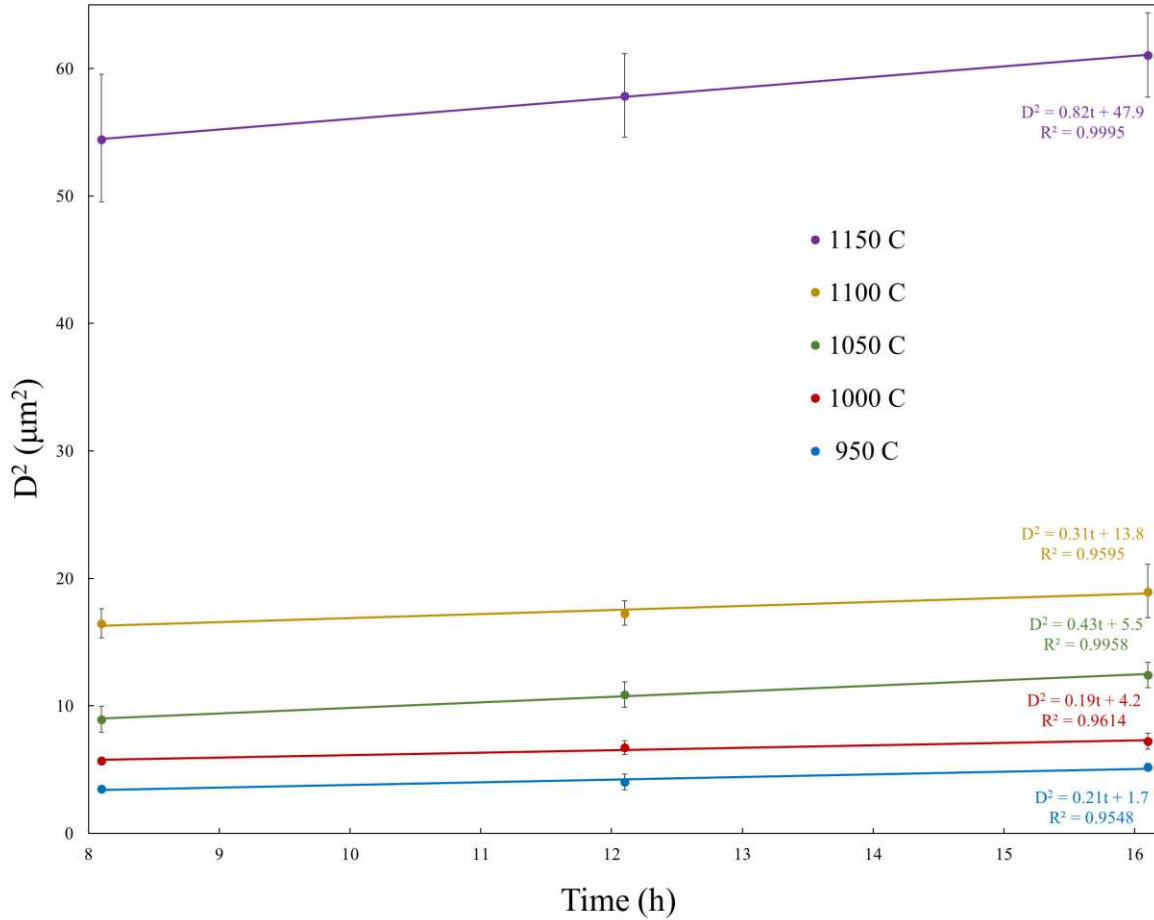

Figure 4.13   Plot of squared average grain size with 95% CI versus time for different temperatures and fitted according to ideal grain growth parameters where the slope of the trendlines is equal to K.

The slope of the linear fit, K, should have an Arrhenius relationship with temperature, as determined by the relationship seen in Equation 4.1. In this equation, K is the temperature-dependent constant, K_0 is a constant for the material system, Q is the activation energy for boundary mobility, R is the ideal gas constant, and T is temperature.

$$K = K_0 \, e^{-Q/RT}$$ (4.1)

The calculated values for K from the assumed ideal grain growth plots above, are plotted against the inverse of time to examine the potential Arrhenius relationship below in Figure 4.14.
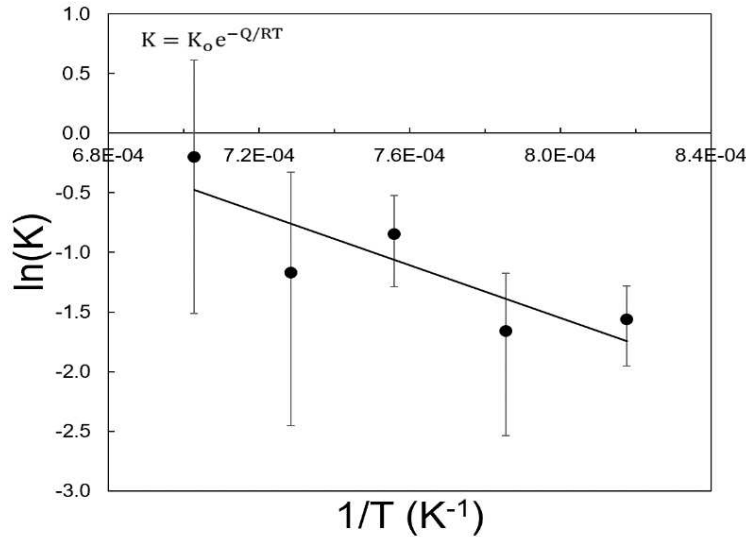

Figure 4.14   Plot of the natural log of *K* versus the inverse of temperature, with a drawn line indicating a potential linear fit.

The error in the slopes from the grain size versus time plots are quite large due to the uncertainty in the individual data points and there only being three times for each temperature. Because of this, it cannot be said with certainty whether there is an Arrhenius relationship. Even if this dataset were to yield a perfectly fit line, the activation energy, *Q*, determined by this setup would be representative of multiple diffusion mechanisms, varying from sintering mechanisms in the early stages of sintering (seen at 950 °C) all the way to increased grain boundary mobility seen in the higher temperatures. In order to get a better idea of the particular activation energies associated with grain growth, a better understanding of the diffusion mechanisms active at different temperatures is required, as well as a controlled experiment where samples are subjected to a common sintering profile prior to additional heat treatments for grain growth.

CHAPTER FIVE: ELECTRICAL CHARACTERIZATION

Various experimental techniques were employed to test the electrical properties of the dense entropy stabilized samples. Single-phase and the two-phase samples, consisting of the rock-salt matrix and the tenorite precipitate, were both investigated to examine how the presence of the copper-rich second phase impacts the properties of the bulk material.

5.1   Methods

Sample Preparation:

All bulk electrical testing was carried out on samples above ~95% of the theoretical density. Silver electrodes were painted on the entire circular face of the cylindrical samples and allowed to cure overnight at room temperature prior to testing. For elevated temperature testing, the electrodes were cured on a hot plate above the temperature reached during testing. Precise electrode areas were determined using ImageJ software.

DC Measurements:

Direct current (DC) measurements were conducted with a Keithley 237 High Voltage Source Measure Unit. Voltage sweeps were performed from 0 V to ± 1000 V with a linear stair sweep method, using 50 V steps and 5 – 60 s delay or hold times at each voltage step, and a 0 V bias. Current sweeps were performed from 0 mA to ± 10 mA with a linear stair sweep method, using 0.5 mA step sizes and 5 – 60 s delay times at each current step with a 0 mA bias. Sweeps were performed from zero to the maximum absolute value of voltage or current to avoid any potential Joule heating or hysteresis. Samples were cooled over five minutes between consecutive measurements to ensure samples were at room temperature.

Impedance Spectroscopy:

Impedance measurements were conducted with a ModulabXM Solartron by Ametek from 0.1 Hz to 1 MHz. with a 1 V oscillator to determine the electrical response of samples under

alternating current (AC). Non-ambient measurements were achieved using a Sun Chamber for heating and cooling. Samples were equilibrated for 10 minutes at each temperature prior to testing. Impedance data were processed using XM-Studio MTS software that was used for the data collection interface with the Solartron.

5.2   DC Measurements

Two single-phase samples with different grain sizes were tested with a linear voltage sweep: one with an average grain size of 7.3 ± 0.3 µm that was sintered at 1150 °C, and another with an average grain size of 2.6 ± 0.2 µm that was sintered at a temperature of 1000 °C. Both samples are approximately 95% of the theoretical density. Both samples exhibit a linear current response to voltage input, seen below in Figure 5.1.
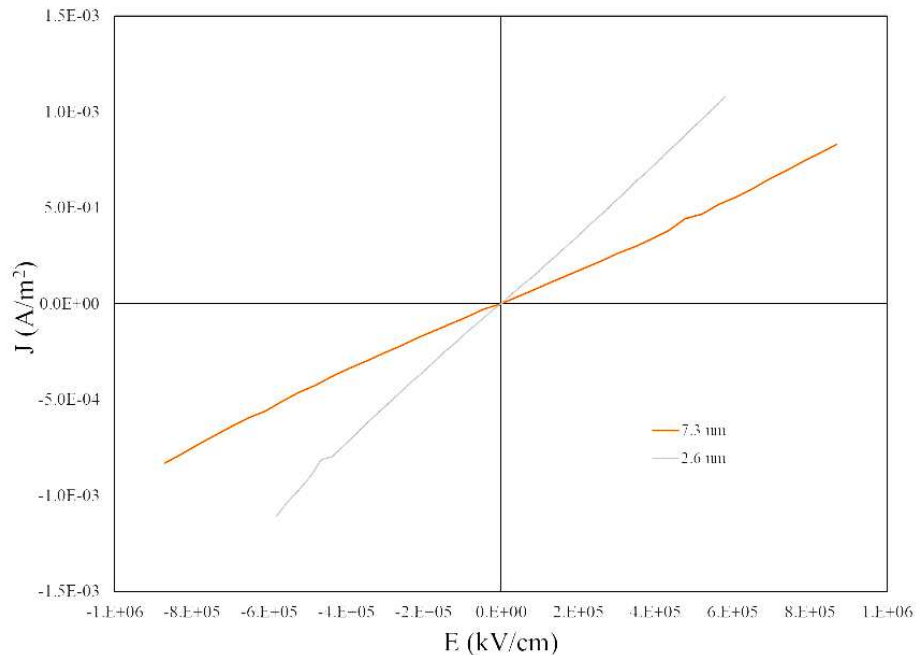
Figure 5.1   I-V curve for two single-phase samples at room temperature with different grain sizes.

With the relationship $V=IR$ where V is voltage, I is current, and R is resistance, (or $E = \rho J$ to be geometry independent) this linear, or ohmic, behavior is indicative of a constant resistance of the sample throughout the voltage sweep. There is a slight difference in the resistance of the

51

two samples, and the sample with a smaller grain size has a steeper slope, indicative of a reduced resistivity in this sample. While this one data point suggests that there may be a dependence of the conductivity on the grain size, and that increasing grain boundary area increases conductivity, additional data sets would be needed to make a conclusion with a wider variety of grain sizes.

The sample with the larger grain size, 7.3 µm, was tested under a voltage sweep again at two different time rates, as seen below in Figure 5.2. The voltage sweep was conducted by holding for a time at each voltage, in 50 V increments. The hold time was tested at 5 and 30 seconds per step to look for any changes in behavior or evidence of resistive, or Joule, heating which can often occur in conductive materials, as P is proportional to I^2R, where P is the power dissipated by the Joule heating. By fitting a linear trend line to the I-V plots above, the resistivity for the sample with a 5 and 30 seconds are both approximately $1 \times 10^9 \, \Omega$ m.
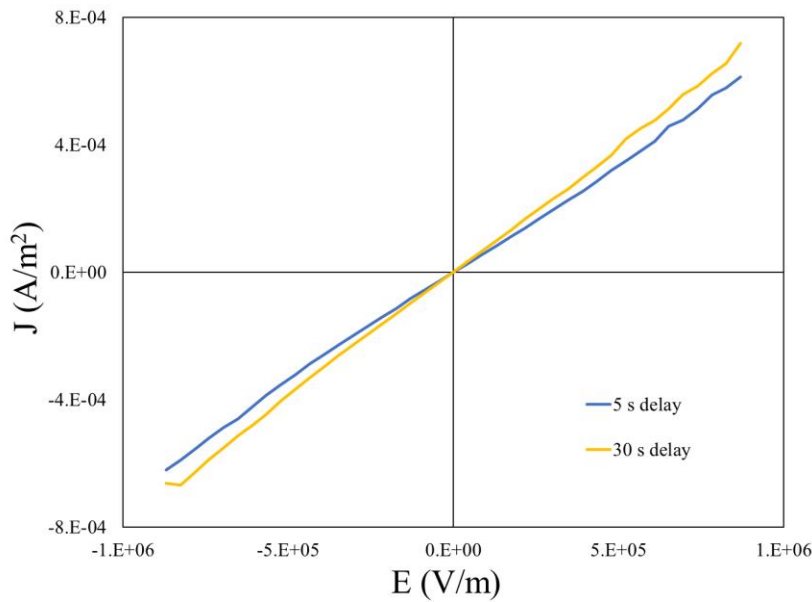
Figure 5.2   I-V curve for single-phase sample at room temperature with different delays or hold times.

Similar DC measurements were conducted on a sample that was allowed to slow cool to precipitate the tenorite phase. Current data were only collected to ± 310 V, due to limitations of the instrument only being able to collect data up to ± 10 mA which was exceeded by this measurement. The I-V curve for this data is shown below in Figure 5.3.
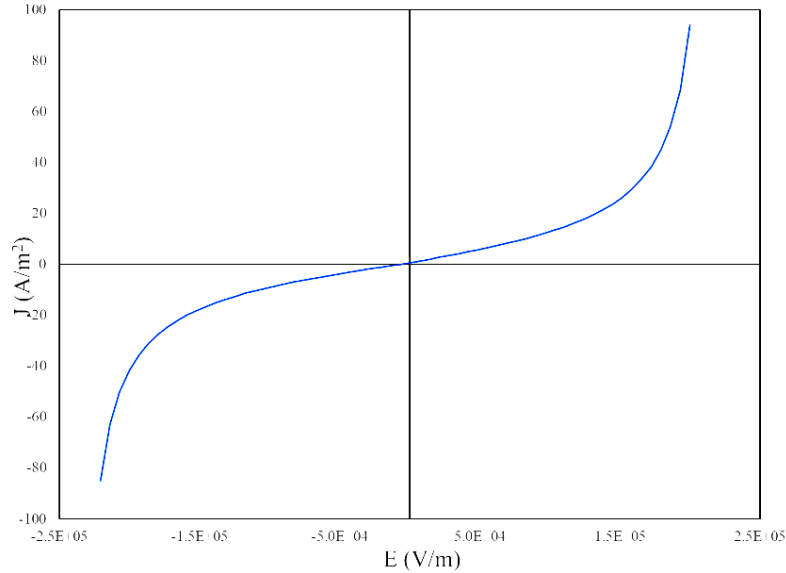
Figure 5.3   I-V curve for two-phase sample at room temperature.

At first glance, it appears as though the sample behaves as a varistor, where the resistance is variable over the range of voltages applied. The current density values reached in this sample are also significantly higher than those of the single-phase sample, meaning that the resistivity is decreased. During the linear portion of the plot, the resistivity of the sample is on the order of 1 x 10^4 Ω m. Once the resistivity starts to drop, it reached measurable values of 3 x 10^3 Ω m. The formation of the tenorite precipitate within this sample reduces the resistivity of the oxide by a factor of 10^6.

The apparent varistor behavior was investigated further by varying the delay or hold time at each voltage step to check for Joule heating, seen in Figure 5.4 below. By holding for a longer time at each voltage step, the sample heats more during each step. This change in behavior with a change in time, along with the qualitative observation that the sample physically heats during testing, suggests that Joule heating is the reason why the I-V curve displays a nonlinear trend. As the sample begins to heat and the temperature is increased, the number of charge carriers, such as electrons or holes, will increase as these charge carriers are thermally activated.
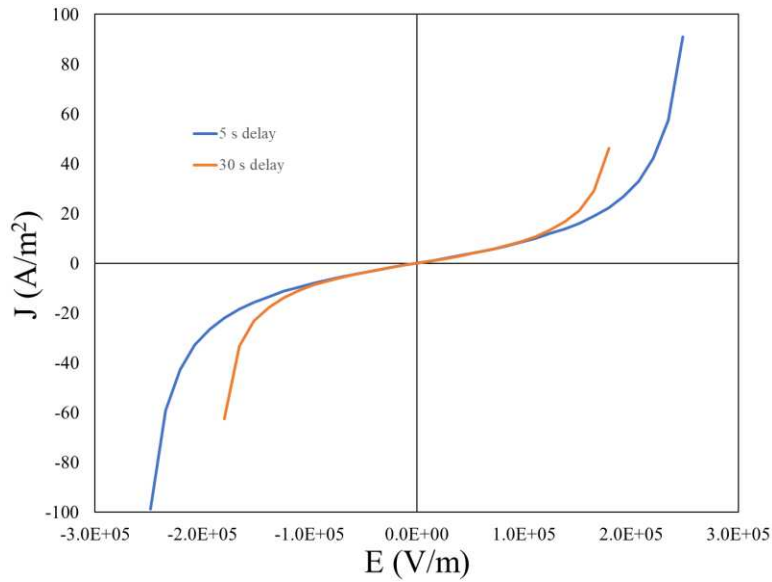
Figure 5.4   I-V curve for two-phase sample at room temperature under different delay or hold times.

A potentiometric scan was conducted on the same sample with different time delays at each current step throughout the sweep, seen in Figure 5.5. As the sample heats and the resistance drops, the voltage across the sample will also drop. This is preferable over the current increase during the voltage sweeps to avoid the compliance issues with the equipment.
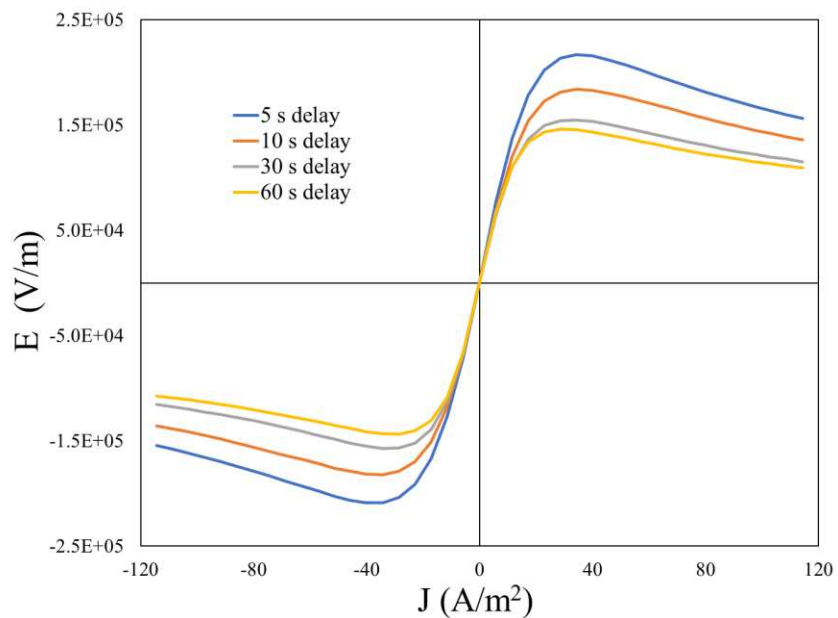

Figure 5.5   Potentiometric scan of two-phase sample under different delay or hold times.

At low current densities, up to approximately 10 A/m^2, the behavior of the material is linear. After this current density is reached, the sample appears to begin to heat faster than heat is dissipated to the environment, resulting in a decrease in resistance. Plots of the resistivity of the material against the electric field shows that the time delay alters the measured resistivity. Plotting the resistivity against the current density shows less of a variation between the different time delays, suggesting that the resistive heating is a function of the current within the material, shown in Figure 5.6.
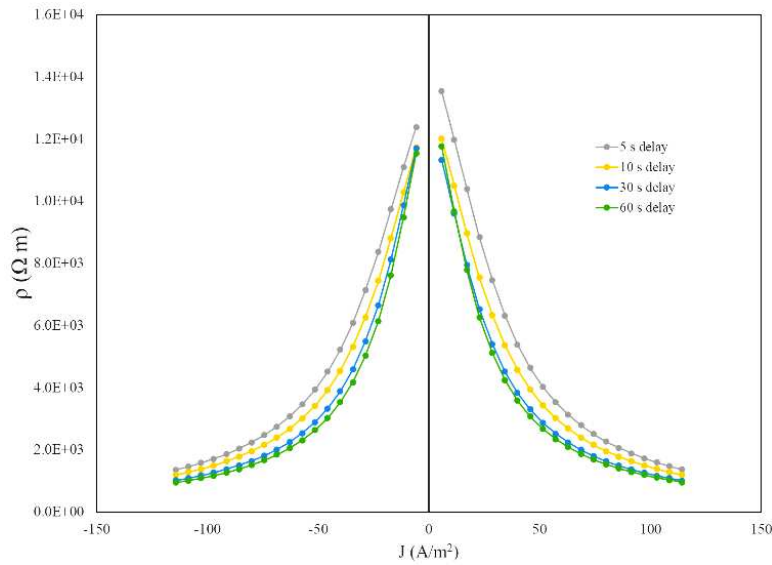
Figure 5.6   Plotted dependence of resistivity on current density of two-phase sample after current sweeps at different hold times.

5.3   AC Measurements

Impedance spectroscopy is a powerful technique that uses AC measurements to characterize the electrical properties of a material over a range of frequencies and can enable the resolution of distinct polarization mechanisms according to their relaxation frequencies [32], [34] [34]. These different polarization mechanisms weaken the applied electric field over characteristic frequencies in dielectric materials [35]. Real materials have complicated responses over a range of frequencies where the overall response is built of contributions from various polarization mechanisms such as the transport of electrons, polarization of dipoles, and the transport of ions under electric fields [33]. Comparing experimental results to expected or modeled results based on

55

the microstructural and chemical models allows for one to decipher the different polarization mechanisms within a material.

5.3.1   Single-Phase Impedance

Frequency sweeps were conducted on a single phase material over a frequency range of 0.1 to 10^6 Hz while the temperature was varied within the material from room temperature to 200 °C. Plots of the real portion of the relative permittivity, $\varepsilon_r{'}$, vs frequency as well as the loss coefficient, *tan δ*, vs frequency are shown in Figure 5.7. These plots reveal that at room temperature, and above frequencies of 10 Hz, where the loss and conductivity within the sample are low, the dielectric constant of the material is approximately 13.
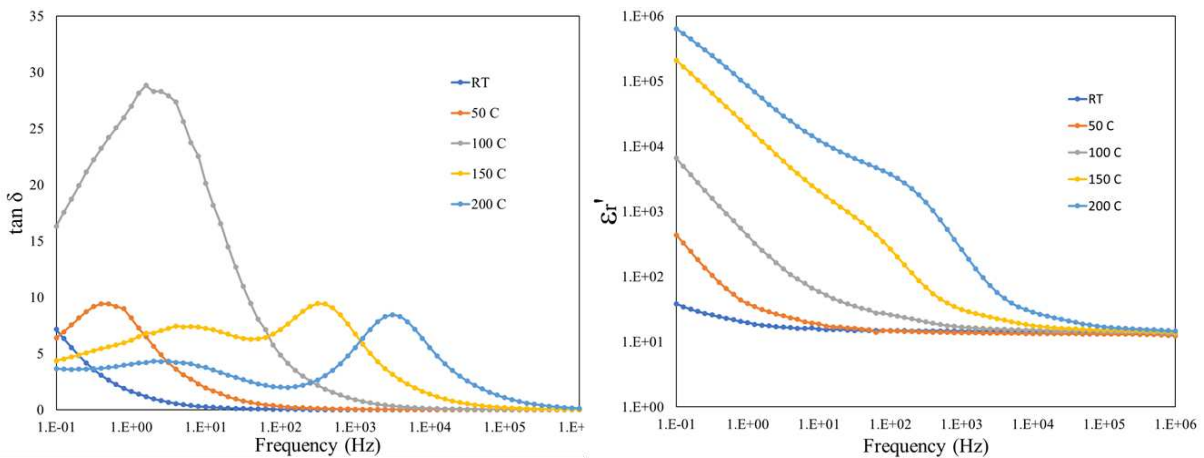
Figure 5.7   Real part of relative permittivity and loss versus frequency for single-phase sample at different temperatures.

Apparent dielectric constants on the order of 10^6 were measured for this sample at temperatures over 150 °C. These large relative permittivity values measured at low frequencies and high temperatures are similar to those reported by Berarden *et al.* [13] but are dominated by conductive contributions within the material, revealed by the large *tan δ* values.

Bode plots of the complex impedance and phase angle as a function of frequency at varied temperatures, shown below in Figure 5.8. These plots provide insight into the behavior of the

material over these frequencies as a capacitor, inductor, or resistor as well as revealing the presence of relaxations.
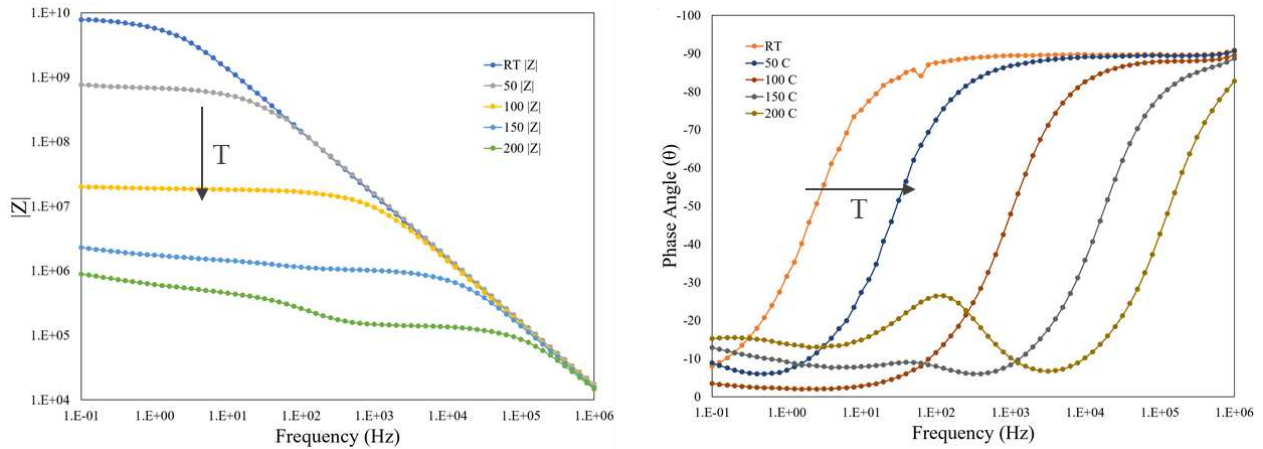
Figure 5.8   Complex impedance (left) and phase angle (right) versus frequency for single-phase sample at different temperatures.

As the phase angle for this material switches from 0 to -90 with increased frequency, the material is transitioning from predominantly resistive behavior to capacitive. For the room temperature frequency sweep, as the frequency is increased, the active charge carriers are not able to keep up with the rate at which the field is switching, and the material appears less like a resistor. As the temperature increases, this frequency where the material switches from resistive behavior to that of a capacitor increases, suggesting that the charge carriers that are active at low frequencies are thermally activated. At low phase angles, the complex impedance is predominantly representative of the resistivity in the sample; as temperature increases, $|Z|$, and therefore the resistivity, decreases. This behavior is consistent with thermally activated conduction mechanisms in the material.

Bode plots also reveal that at higher temperatures, 150 and 200 °C, there may be additional relaxations and polarization mechanisms that become dominant, which can be seen more clearly in the Nyquist plots below in Figure 5.9. It is evident in these plots that as the temperature increases, additional polarization mechanisms are detectable and active within this range of frequencies, indicated by the presence of additional semicircles plotted in the complex Z plane.

57
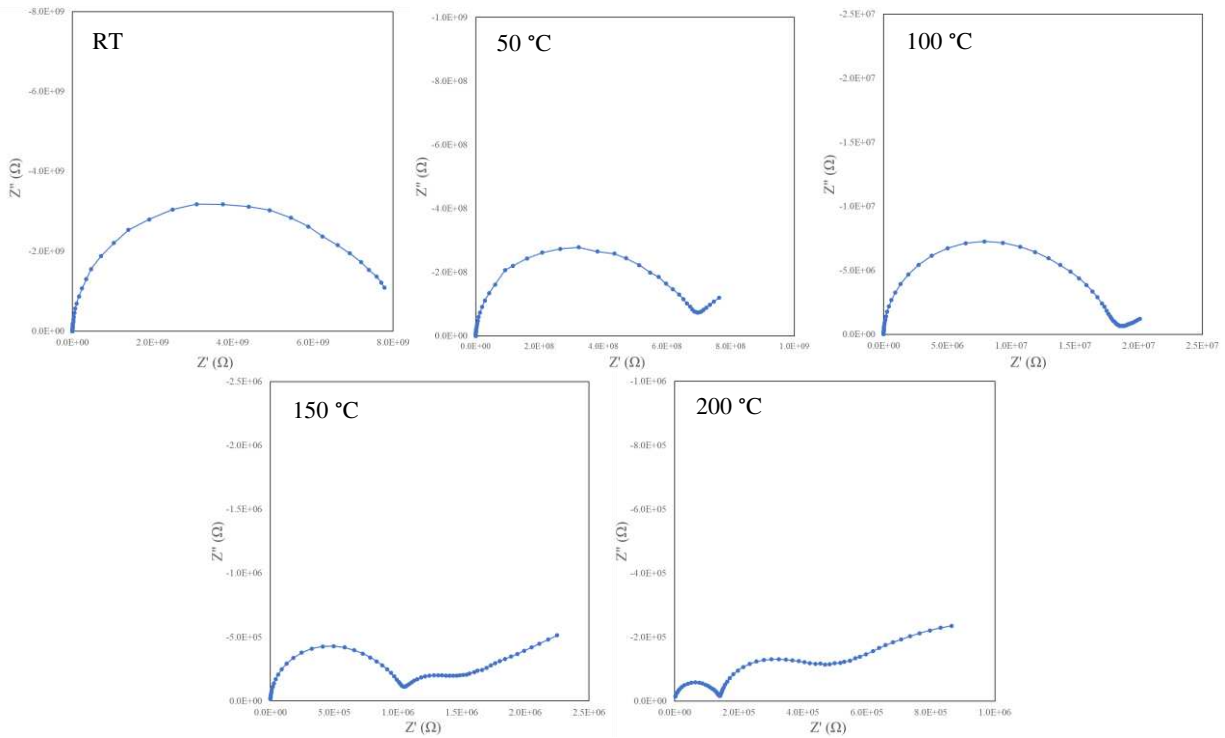
Figure 5.9   Nyquist plots for single-phase sample from room temperature to 200 °C.

The mechanisms detectable at room temperature remain active and dominant at high temperatures and shift towards higher frequencies. The new conduction mechanisms that are seen at higher temperatures are active over lower frequencies and are likely still present at lower temperatures but are not accessible by the parameters of this measurement.

The charge carriers active and visible at room temperature appear to have two overlapping semicircles in the Nyquist plot that would suggest that there are two polarization mechanisms active over a similar range of frequencies. Since there is no change in the shape of these overlapping mechanisms with temperature, the two are treated here as one joint mechanism. It is possible that this overlapping mechanism is related to the contact between the sample and the electrodes. It is likely that an increase in charge carriers with increased temperature causes this mechanism to experience decreased capacitance and resistance, as seen in the Nyquist plots. This thermally activated conduction mechanism is likely responsible for the phase angle shift occurring at higher frequencies as the temperature is increased. While it cannot be determined by the present measurements, it is possible that this constant mechanism is band conduction as a result of hole or

58

electron conductivity, which increases with temperature due to the exponential dependence of charge carriers on temperature.

As the temperature increases, two additional low frequency polarization mechanisms become active. Possible identifications for these mechanisms in this material include electron and hole transport, ion diffusion, and polaron hopping due to the presence of multiple transition metals within the material. Both ion and polaron conductivity have an Arrhenius dependence on temperature due to an increase in the mobility of these mechanisms and could potentially be responsible for the behavior seen in the impedance measurements.

5.3.2   Two-Phase Impedance

An identical experiment was conducted on a two-phase sample, where the temperature was varied from room temperature to 200 °C and frequency sweeps were done over a range of 0.1 to 10^6 Hz. The Bode plots, showing complex impedance and phase angle as a function of frequency, shown above in Figure 5.10, reveal that the two-phase sample behaves purely as a resistor over a larger range of frequencies than the single-phase sample.
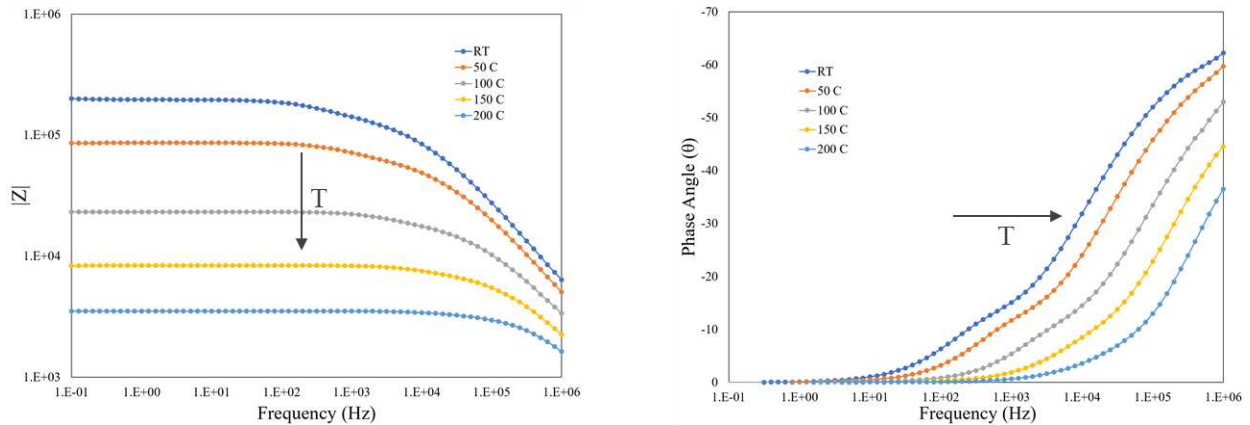
Figure 5.10   Complex impedance (left) and phase angle (right) versus frequency for two-phase sample at different temperatures.

Over a range of 0.1 to nearly 10 Hz, the complex impedance is purely the real impedance, which is equal to the resistance of the material. The complex impedance plot shows that as the

temperature increases, the resistivity of the sample decreases, indicative of thermally activated charge carriers. As the temperature and frequency increase, the phase angle shifts towards the behavior of a capacitor, however, at no temperature does the material reach a purely capacitive behavior. This suggests that the material's active conduction mechanisms are able to keep up with high frequencies of field switching, likely due to an increase in charge carriers or mobility.

Despite the sample having additional interfaces and phases (such as tenorite – rock-salt interfaces and the presence of a second bulk phase), the Nyquist plots, shown below in Figure 5.11, for these frequency sweeps only appear to reveal two active conduction mechanisms, seen as semicircles, over this frequency and temperature range.
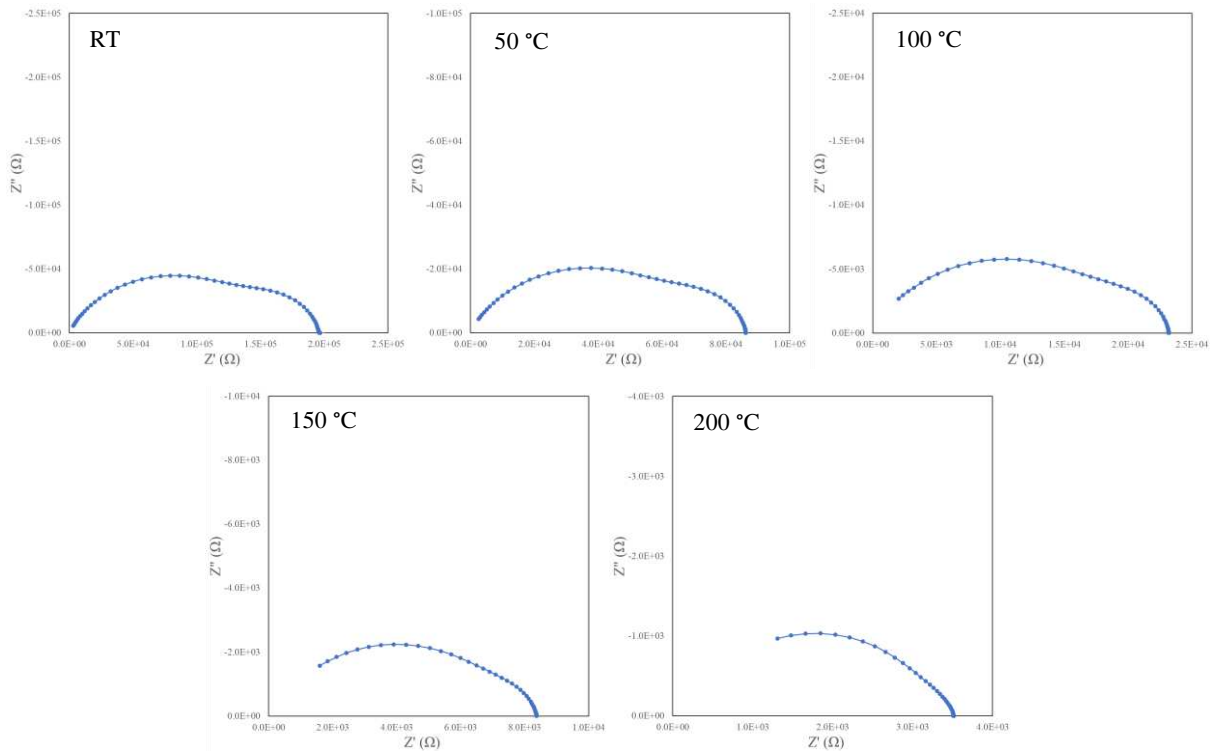
Figure 5.11   Nyquist plots for two-phase sample from room temperature to 200 °C.

The limited change in the Nyquist plots with respect to temperature suggests that the conduction mechanisms that are dominant at room temperature are also dominant throughout the entire temperature and frequency range probed, preventing any other mechanisms from being identified. The decrease in resistivity with an increase in temperature also suggests that these two active mechanisms, seen as two overlapping circles, are thermally activated.

60

CHAPTER SIX: CONCLUSIONS

The formation and entropy stabilization of the (Mg,Ni,Co,Cu,Zn)O system has been evaluated and the reversibility of the phase formation has been confirmed in this study. While the material is globally rock-salt, there are nanoscale defect regions where the cations are displaced off of their ideal lattice points. These regions of inhomogeneity are a result of the tendency of Cu^{2+} ions to cluster to relieve the global stress within the system as well as the tetragonal distortion often seen around octahedrally coordinated copper ions as a result of Jahn-Teller distortion. This copper segregation occurs over temperature ranges where the full phase transformation to tenorite is still kinetically hindered. This leads to selective peak broadening seen in experimental XRD patterns and many patterns published in literature.

The reversible precipitation of a second, copper-rich tenorite phase can be quantified and controlled by altering the time and temperature of low temperature anneals. After extended anneal times, XRD is able to detect the presence of additional phases as the stability of the rock-salt matrix is reduced.

Sintering investigations produced improved densities over other reports using bulk processing methods and solid-state sintering. Densities of 95% of the theoretical maximum were achieved by planning thermal profiles around the different densification mechanisms determined by dilatometry experiments. Attempts to utilize the higher temperature regime while still allowing for low temperature oxidation and reduction reactions to occur yielded denser samples than previously reported with these fabrication methods.

Electrical characterization revealed that the single-phase sample is a resistive material with a linear relationship between voltage and current. Impedance measurements revealed several thermally activated conduction mechanisms over low frequencies. The two-phase sample is more conductive by a factor of 10^6 than the single-phase material, likely as a result of the CuO tenorite phase. Impedance measurements reveal that the conduction mechanisms active at room temperature continue to dominate the material's properties at elevated temperatures.

REFERENCES

[1]   K. T. Butler, A. Walsh, A. K. Cheetham, and G. Kieslich, "Organised chaos: Entropy in hybrid inorganic-organic systems and other materials," *Chem. Sci.*, vol. 7, no. 10, pp. 6316–6324, 2016.

[2]   C. M. Rost *et al.*, "Entropy-stabilized oxides," *Nat. Commun.*, vol. 6, p. 8485, 2015.

[3]   J. W. Yeh *et al.*, "Nanostructured high-entropy alloys with multiple principal elements: Novel alloy design concepts and outcomes," *Adv. Eng. Mater.*, vol. 6, no. 5, pp. 299-303+274, 2004.

[4]   D. B. Miracle and O. N. Senkov, "A critical review of high entropy alloys and related concepts," *Acta Mater.*, vol. 122, pp. 448–511, 2017.

[5]   M. C. Gao, D. B. Miracle, D. Maurice, X. Yan, Y. Zhang, and J. A. Hawk, "High-entropy functional materials," *J. Mater. Res.*, vol. 33, no. 19, pp. 3138–3155, 2018.

[6]   W. Hong, F. Chen, Q. Shen, Y. H. Han, W. G. Fahrenholtz, and L. Zhang, "Microstructural evolution and mechanical properties of (Mg,Co,Ni,Cu,Zn)O high-entropy ceramics," *J. Am. Ceram. Soc.*, vol. 102, no. 4, pp. 2228–2237, 2019.

[7]   J.-W. Yeh and S.-J. Lin, "Breakthrough applications of high-entropy materials," *J. Mater. Res.*, vol. 33, no. 19, pp. 3129–3137, 2018.

[8]   A. Sarkar *et al.*, "High-Entropy Oxides: Fundamental Aspects and Electrochemical Properties," *Advanced Materials*. Wiley-VCH Verlag, 2019.

[9]   B. S. Murty, J.-W. Yeh, and S. Ranganathan, *High-Entropy Alloys*. London, 2014.

[10]   G. Anand, A. P. Wynn, C. M. Handley, and C. L. Freeman, "Phase stability and distortion in high-entropy oxides," *Acta Mater.*, vol. 146, pp. 119–125, 2018.

[11]   C. M. Rost, Z. Rak, D. W. Brenner, and J. P. Maria, "Local structure of the MgxNixCoxCuxZnxO(x=0.2) entropy-stabilized oxide: An EXAFS study," *J. Am. Ceram. Soc.*, vol. 100, no. 6, pp. 2732–2738, 2017.

[12]   Z. Rák, J. P. Maria, and D. W. Brenner, "Evidence for Jahn-Teller compression in the (Mg Co Ni Cu Zn)O entropy-stabilized oxide: A DFT study," *Mater. Lett.*, vol. 217, pp. 300–303, 2018.

[13]   D. Bérardan, S. Franger, D. Dragoe, A. K. Meena, and N. Dragoe, "Colossal dielectric constant in high entropy oxides," vol. 10, no. 4, pp. 328–333, Apr. 2016.

[14]   A. Sarkar *et al.*, "Nanocrystalline multicomponent entropy stabilised transition metal oxides," *J. Eur. Ceram. Soc.*, vol. 37, no. 2, pp. 747–754, 2017.

[15]   R. Djenadic *et al.*, "Multicomponent equiatomic rare earth oxides," *Mater. Res. Lett.*, vol. 5, no. 2, pp. 102–109, 2017.

[16] A. Sarkar *et al.*, "Multicomponent equiatomic rare earth oxides with a narrow band gap and associated praseodymium multivalency," *Dalt. Trans.*, vol. 46, no. 36, pp. 12167–12176, 2017.

[17] S. Jiang *et al.*, "A new class of high-entropy perovskite oxides," *Scr. Mater.*, vol. 142, pp. 116–120, 2018.

[18] J. Gild *et al.*, "High-Entropy Metal Diborides: A New Class of High-Entropy Materials and a New Type of Ultrahigh Temperature Ceramics," *Sci. Rep.*, vol. 6, no. 1, p. 37946, 2016.

[19] J. L. Braun *et al.*, "Charge-Induced Disorder Controls the Thermal Conductivity of Entropy-Stabilized Oxides," *Advanced Materials*, 2018.

[20] A. Giri, J. L. Braun, and P. E. Hopkins, "Reduced dependence of thermal conductivity on temperature and pressure of multi-atom component crystalline solid solutions," *J. Appl. Phys.*, vol. 123, no. 1, 2018.

[21] M. Lim *et al.*, "Influence of mass and charge disorder on the phonon thermal conductivity of entropy stabilized oxides determined by molecular dynamics simulations," *J. Appl. Phys.*, vol. 125, no. 5, 2019.

[22] A. Sarkar *et al.*, "High entropy oxides for reversible energy storage," *Nat. Commun.*, vol. 9, no. 1, 2018.

[23] D. Bérardan, S. Franger, A. K. Meena, and N. Dragoe, "Room temperature lithium superionic conductivity in high entropy oxides," *J. Mater. Chem. A*, vol. 4, no. 24, pp. 9536–9541, 2016.

[24] P. B. Meisenheimer, T. J. Kratofil, and J. T. Heron, "Giant enhancement of exchange coupling in entropy-stabilized oxide heterostructures," *Sci. Rep.*, vol. 7, no. 1, 2017.

[25] H. Chen *et al.*, "Entropy-stabilized metal oxide solid solutions as CO oxidation catalysts with high-temperature stability," *J. Mater. Chem. A*, vol. 6, no. 24, pp. 11129–11133, 2018.

[26] B. H. Toby and R. B. Von Dreele, "GSAS-II: the genesis of a modern open-source all purpose crystallography software package," *J. Appl. Crystallogr.*, vol. 46, no. 2, pp. 544–549, 2013.

[27] D. Berardan, A. K. Meena, S. Franger, C. Herrero, and N. Dragoe, "Controlled Jahn-Teller distortion in (MgCoNiCuZn)O-based high entropy oxides," *J. Alloys Compd.*, vol. 704, pp. 693–700, 2017.

[28] S.-J. Kang, "1 - Sintering Processes," in *Sintering: Densification, Grain Growth, and Microstructure*, 2005.

[29] R. M. German, "Thermodynamics of Sintering," in *Sintering of Advanced Materials*, 2010, pp. 2–32.

[30] R. M. German, "Sintering," *Encyclopedia of Materials: Science and Technology (Second Edition)*. pp. 8641–8643, 2001.

[31] M. N. Rahaman, *Sintering of Ceramics*. Boca Raton: Taylor & Francis Group, 2007.

[32] R. Gerhardt, "Impedance and dielectric spectroscopy revisited: Distinguishing localized relaxation from long-range conductivity," *J. Phys. Chem. Solids*, vol. 55, no. 12, pp. 1491–1506, 1994.

[33] N. Bonanos, P. Pissis, and J. R. Macdonald, "Impedance Spectroscopy of Dielectrics and Electronic Conductors," *Charact. Mater.*, pp. 1–14, 2012.

[34] E. Barsoukov and J. R. Macdonald, *Impendance Spectroscopy*. 2018.

[35] R. E. Hummel, *Electronic Properties of Materials-Springer-Verlag*. 2011.

A.1   Precursor Characterization

The following section of the appendix characterizes the precursor, starting oxides used to fabricate the (Mg,Ni,Co,Cu,Zn)O entropy stabilized oxide. XRD and ESEM techniques were employed to verify the phase of the starting oxides, particle morphology, and to look for any additional elemental components using EDS techniques.

The zinc oxide precursor should have the formula ZnO with a wurtzite structure and a P63cm space group. The XRD pattern on a powder sample is shown below in Figure A.2 with orange dots showing the calculated powder diffraction pattern for this material. The relative peak heights for the experimental pattern are similar to that of the calculated pattern. There is a slight 2θ offset between the measured peaks and the calculated peaks that increases at larger 2θ values, suggesting that this offset is due to a z-height issue during the sample measurement. ESEM images of the ZnO powder are shown below in Figure A.3. Backscatter imaging and EDS were used to verify that Zn and O are the only elemental components within the system and no Z-contrast was visible to suggest areas of inhomogeneities.
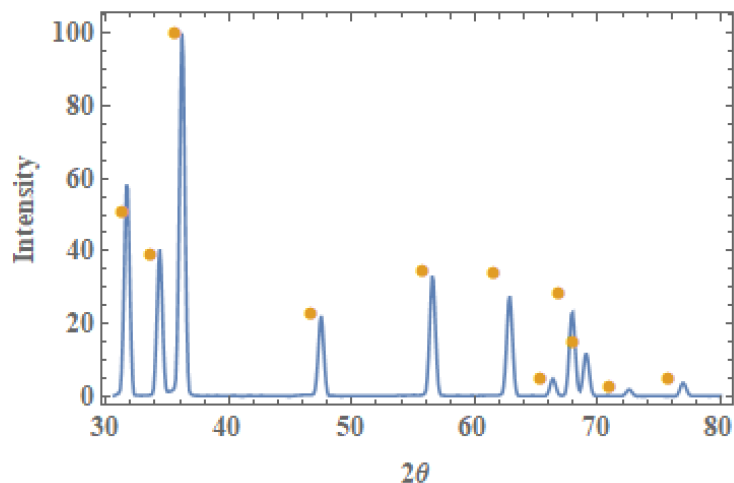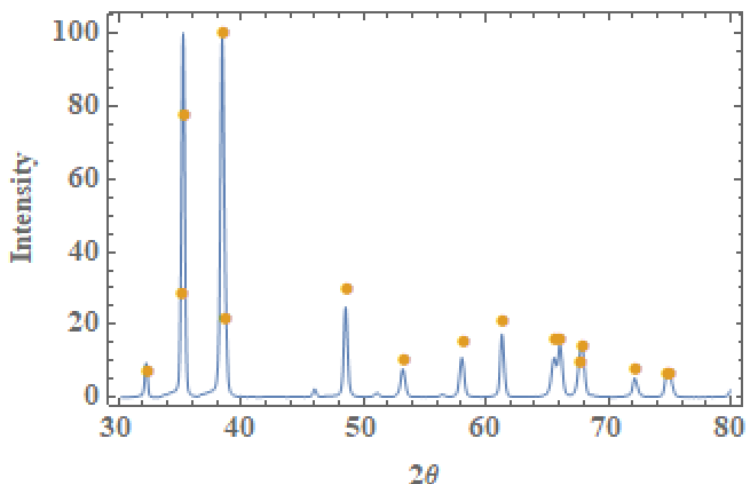

Figure A.1   Experimental XRD pattern for ZnO with calculated diffraction pattern indicated by orange dots (●).
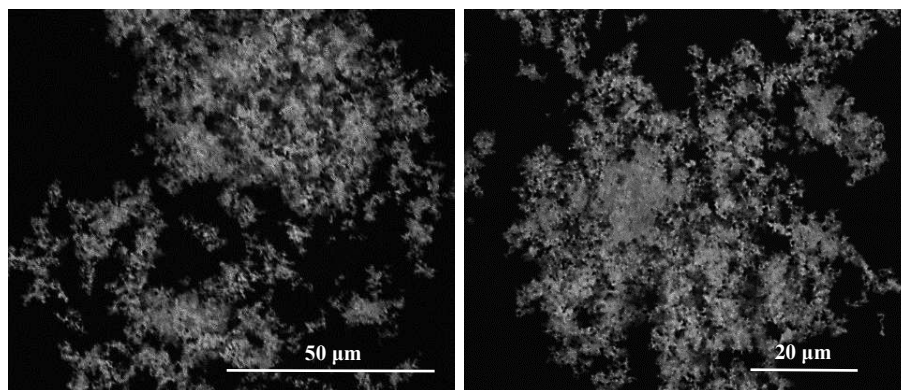
Figure A.2   ESEM images of ZnO powders as received.

The nickel oxide precursor should have a chemical formula of NiO with a rock salt structure and a Fm$\bar{3}$m space group. The XRD pattern is shown below in Figure A.4 and the calculated pattern for the material is shown as orange dots. The peak placement and height match up with the experimental pattern, confirming the identity of the material. Prior to XRD, the NiO powders were crushed using an alumina mortar and pestle due to the large particle size. The ESEM images shown below in Figure A.5 reveal the large particle size of the precursor NiO. These chunks of NiO are on the order of 0.5 mm. EDS and backscatter imaging revealed no areas of inhomogeneities or the presence of additional elements. Due to the size of these clumps, the precursor was crushed prior to further processing.
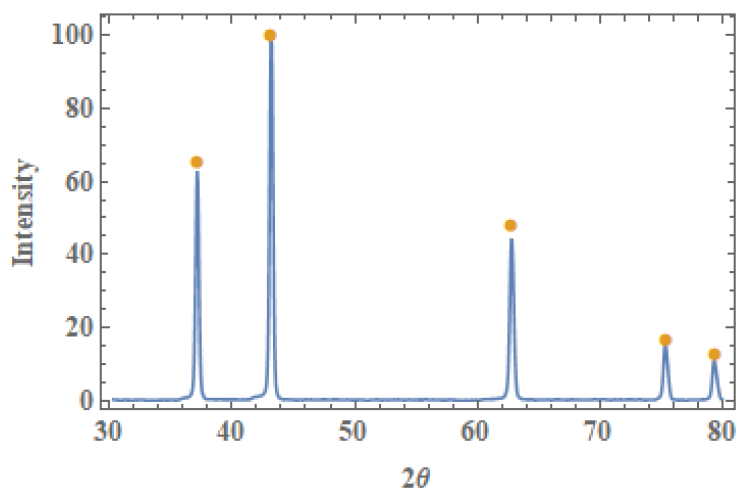
Figure A.3   Experimental XRD pattern for NiO with calculated diffraction pattern indicated by orange dots (●).
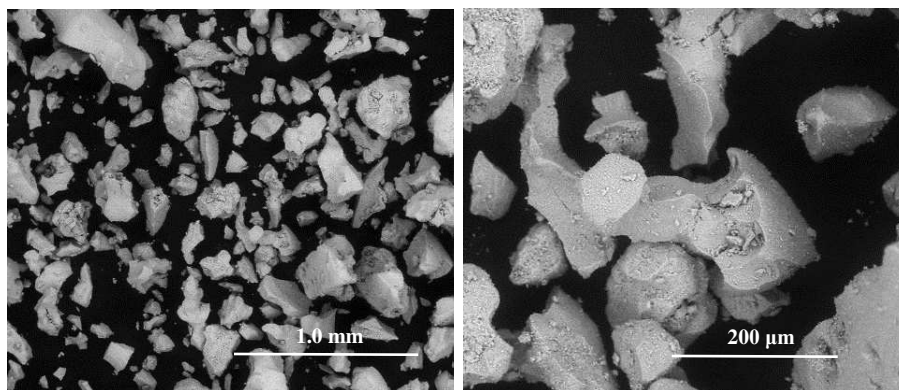
Figure A.4　ESEM images of NiO powders as received.

The magnesium oxide should have a chemical formula of MgO, a rock-salt structure, and a $Fm\overline{3}m$ space group. The measured XRD pattern is shown below in Figure A.6 with orange dots indicating the calculated powder diffraction pattern. The experimental and calculated patterns line up, confirming the phase of the precursor. The ESEM images shown in Figure A.7 reveal the particle size and that there are no visible contaminants within the powders of other elements.
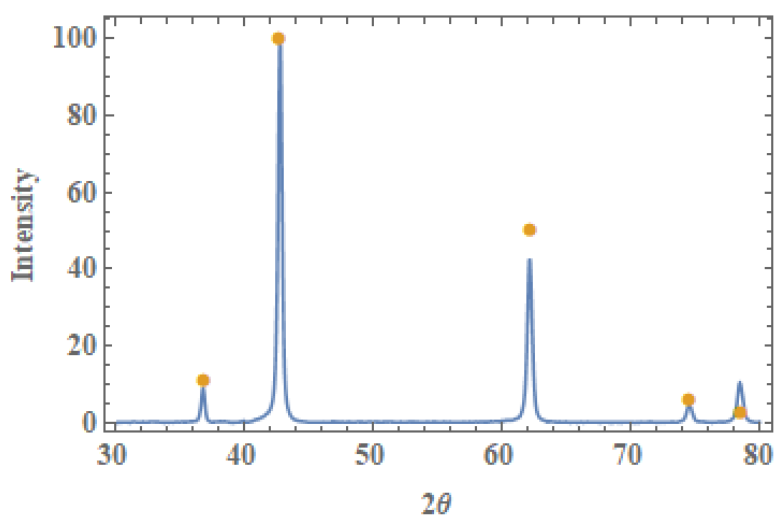
Figure A.5　Experimental XRD pattern for MgO with calculated diffraction pattern indicated by orange dots (●).
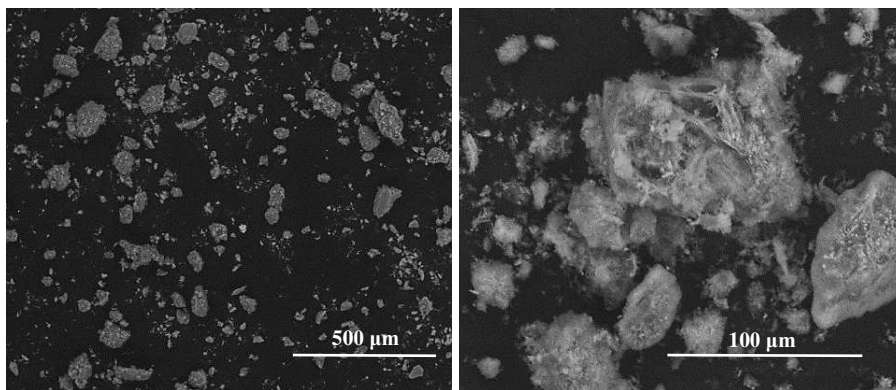
Figure A.6   ESEM images of MgO powders as received.

The copper oxide precursor should have a chemical formula of CuO, a tenorite structure, with a C2/c space group. The XRD pattern shown below in Figure A.8 shows the experimental diffraction pattern for the powders and the calculated powder diffraction pattern. A few peaks are notable that are not accounted for by the C2/c CuO which are instead fit by a minor amount of cubic CuO with a space group of $Pm\overline{3}m$. The ESEM images of the as received powder shown in Figure A.9 show the particle morphology and do not reveal any contaminants.

Figure A.7   Experimental XRD pattern for CuO with calculated diffraction pattern indicated by orange dots (●).
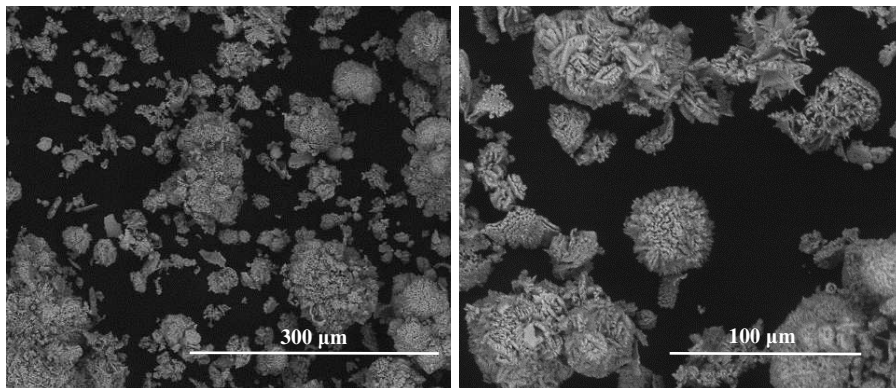
Figure A.8   ESEM images of CuO powders as received.

The precursor cobalt oxide as received should be CoO with up to 10% of Co_3O_4. The CoO should have a rock-salt structure with a $Fm\overline{3}m$ space group and the Co_3O_4 should have a spinel structure with a $Fd\overline{3}m$ space group. The experimental XRD pattern is shown below in Figure A.10 with the calculated powder diffraction pattern for CoO shown in orange dots and the Co_3O_4 calculated pattern shown in green dots. While the peak heights do not match due to the relative amount of each phase, the peak locations do match up and account for all experimentally detected peaks. The phase amounts for CoO and Co_3O_4 were refined using GSAS II [26]. ESEM images with backscatter and EDS did not reveal any contaminants.
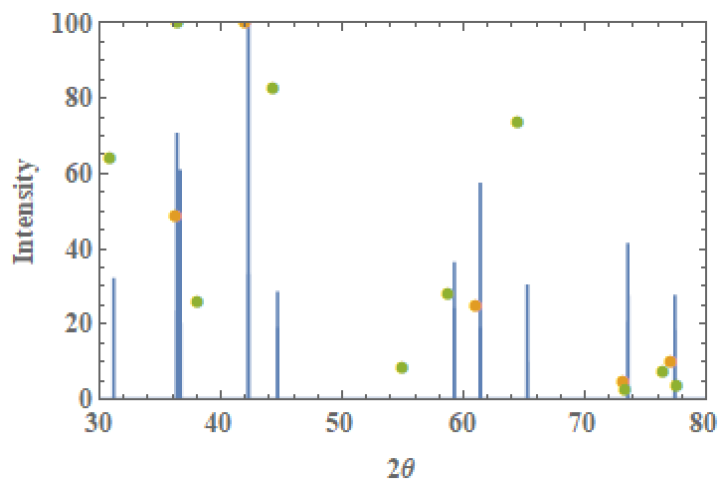
Figure A.9   Experimental XRD pattern for CoO with calculated diffraction pattern indicated by orange dots (●) and Co_3O_4 indicated by green dots. (●)
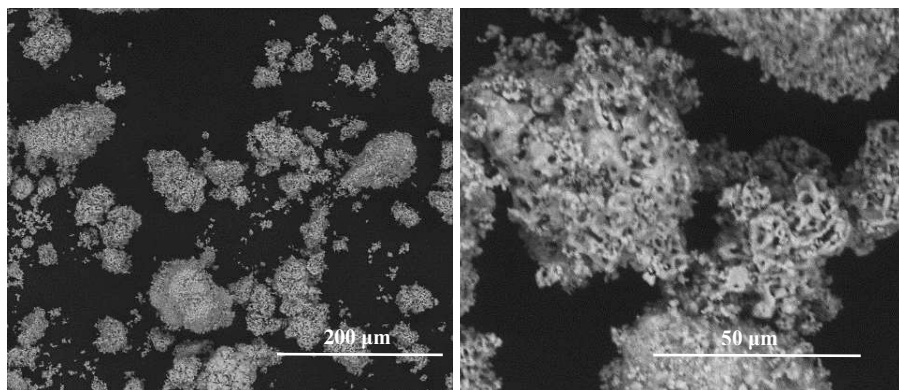
Figure A.10   ESEM images of CoO powders as received.

A.2   XRD Pattern for Reduced Two-Phase Sample

The following plot is of a diffraction pattern for a two-phase sample that was annealed under reducing conditions and shown to contain precipitates of copper, rather than copper oxide.
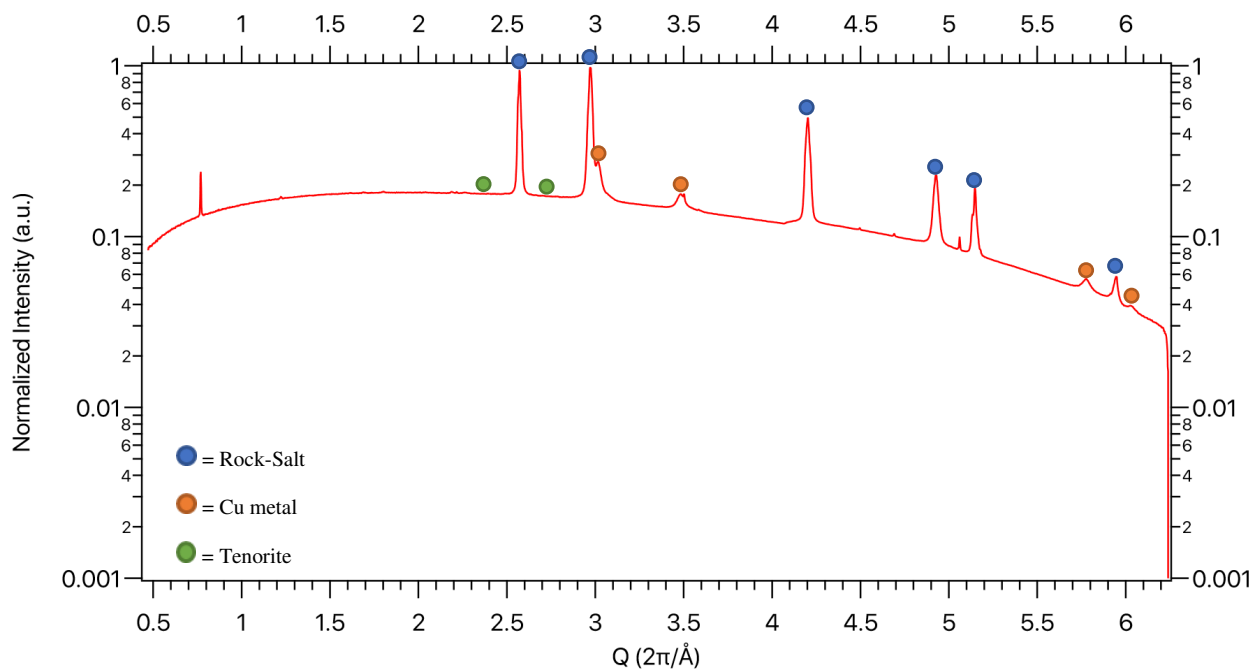
Figure A.11   Diffraction pattern for reduced sample discussed in Figure 3.12. Blue dots indicate the rock-salt structure, orange dots indicate the reduced copper metal, and the two green dots indicate the lack of CuO tenorite. Several peaks are unidentified.

A.3   Calculated Tetragonal Diffraction Patterns

The following calculated powder diffraction patterns show the rock-salt structure as cubic (Figure A.13), as well as experiencing a 1% contraction (Figure A.14) and elongation (Figure A.15) along the c-axis. These plots demonstrate that under slight tetragonal distortion, the (111) and (222) peaks of the parent cubic structure would be unaffected, whereas the other peaks would adopt a broadened, shortened appearance.
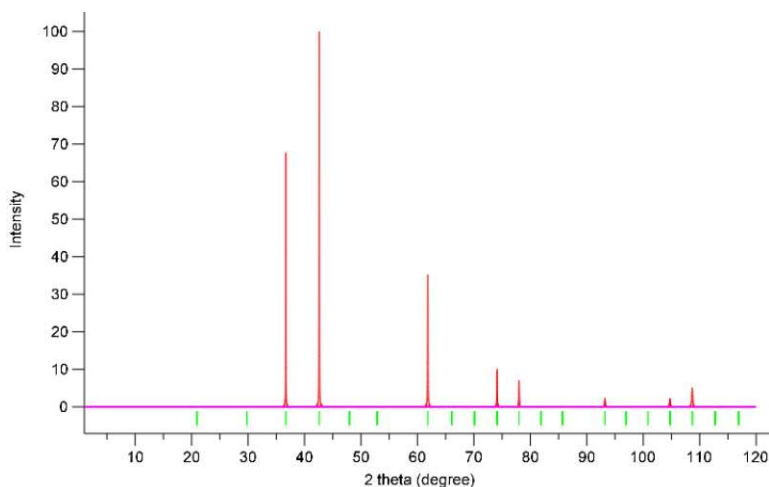
Figure A.12   Calculated powder diffraction pattern for (Mg,Ni,Co,Cu,Zn)O with cubic rock-salt structure: a = 4.24 Å.
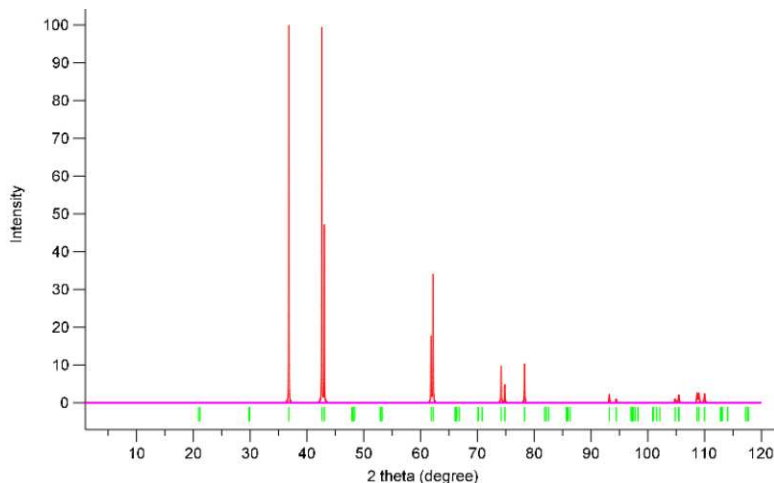
Figure A.13   Calculated powder diffraction for (Mg,Ni,Co,Cu,Zn)O with 1% compression along the c-axis: a = 4.2400 Å, c = 4.1976 Å.
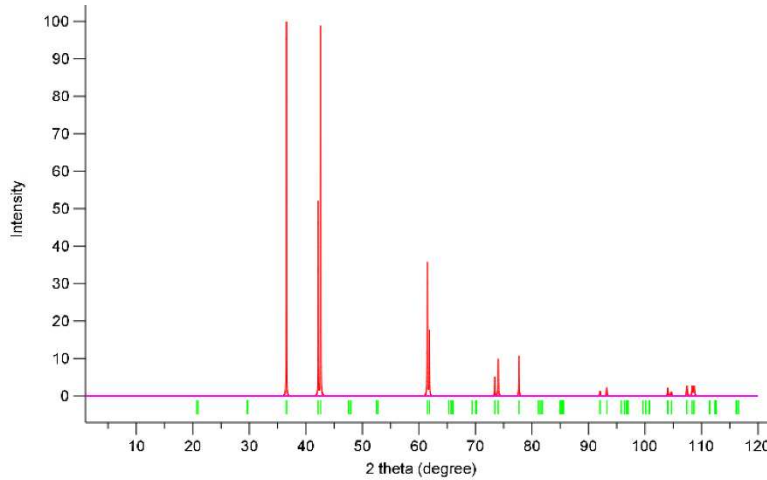
Figure A.14   Calculated powder diffraction patterns for (Mg,Ni,Co,Cu,Zn)O with 1%
elongation along the c-axis: a = 4.2400 Å, c = 4.1976 Å.

A.4   Particle Size Data

Prior to sintering studies, all powders were milled using a planetary mill. In the figures below are particle size data for a calcined powder before milling, after being milled for six hours in the planetary mill at 400 RPM, and after being milled under the same conditions a second time.
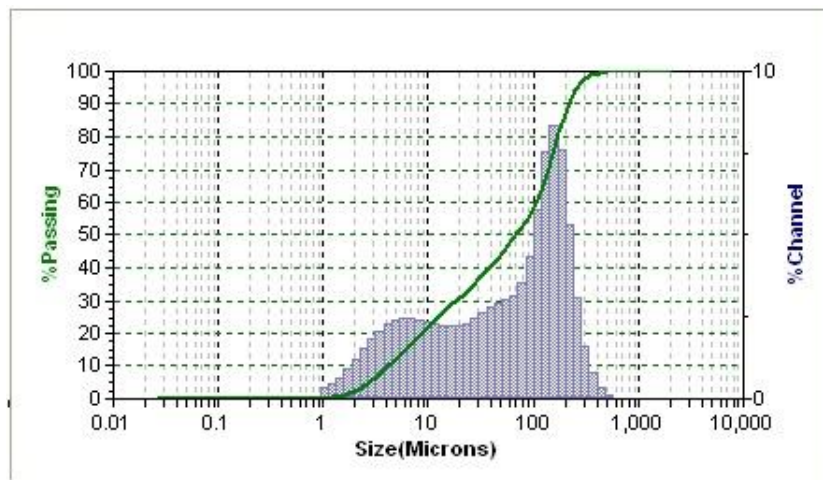
Figure A.15   Particle size data for calcined powder after being crushed with a mortar and pestle.
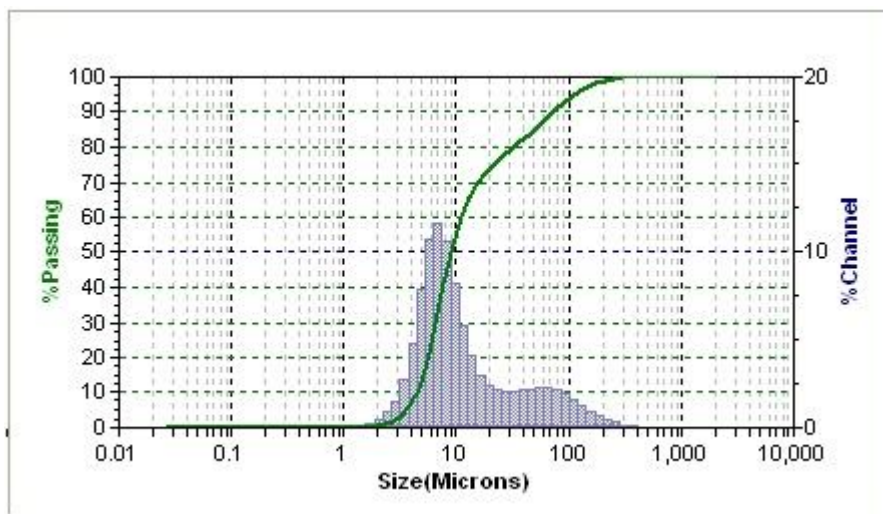
Figure A.16   Particle size data for calcined powder after planetary milling at 400 RPM for 6 hours showing reduced particle size from before milling.
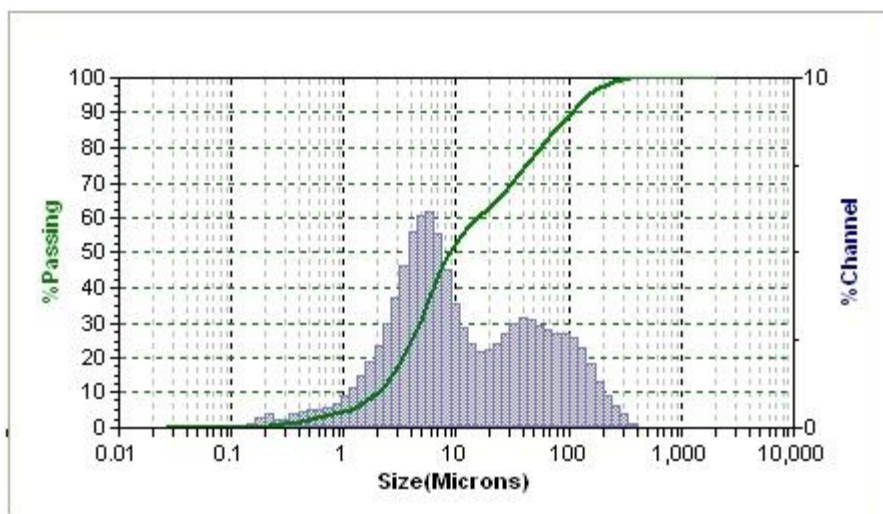
Figure A.17   Particle size data after milling a second time with the planetary mill where the increase in bimodal distribution suggests agglomeration of the small particles.

A.5   Supplementary ESEM Images

In this section of the appendix, additional ESEM images are presented for each sample that was discussed in the main body of the thesis. In order to draw conclusions from the sample images, it is important to demonstrate that the trends can be observed in more than one image.
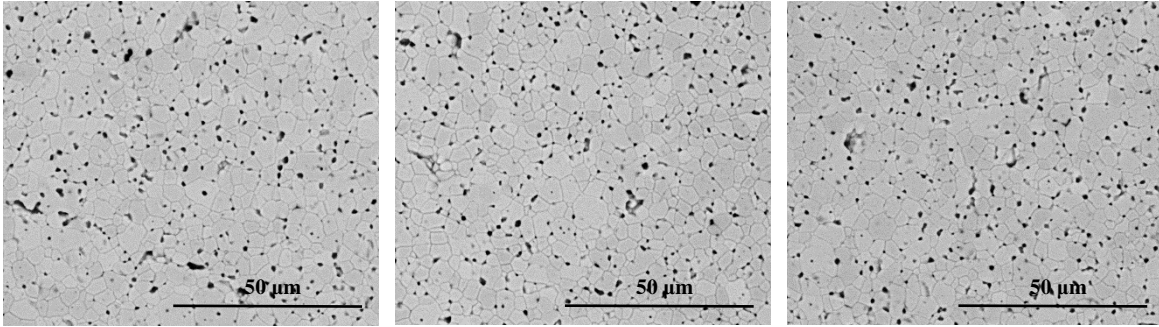
Figure A.18   ESEM images of sample formed with a uniaxial press under 18 ksi pressure and heated from room temperature to 970 °C at a rate of 5 °C/minute, held for 8 hours and air quenched (sample ID *I2*).
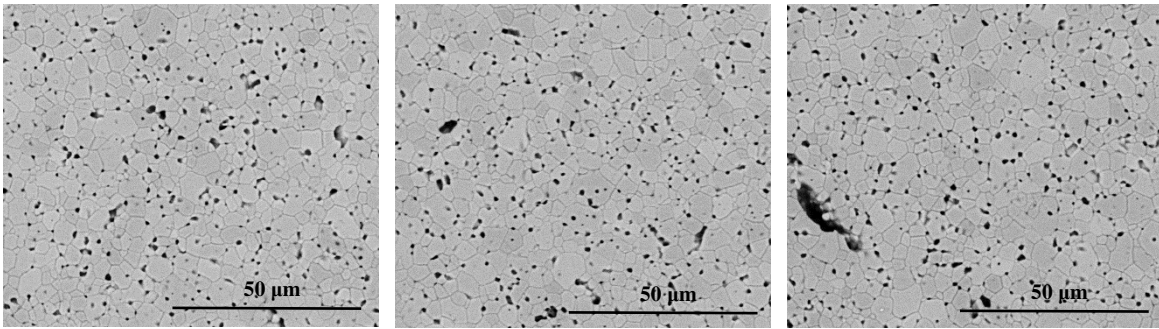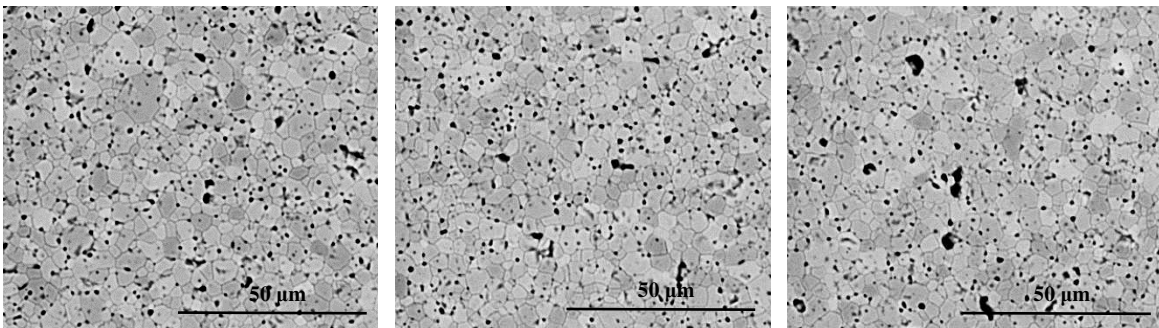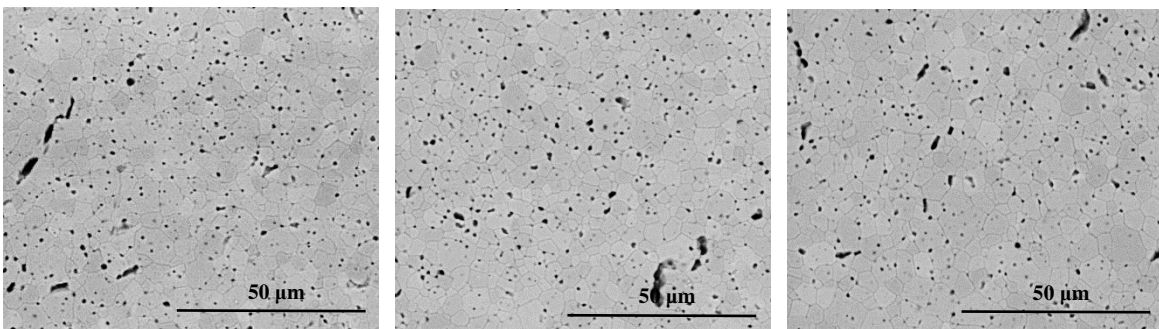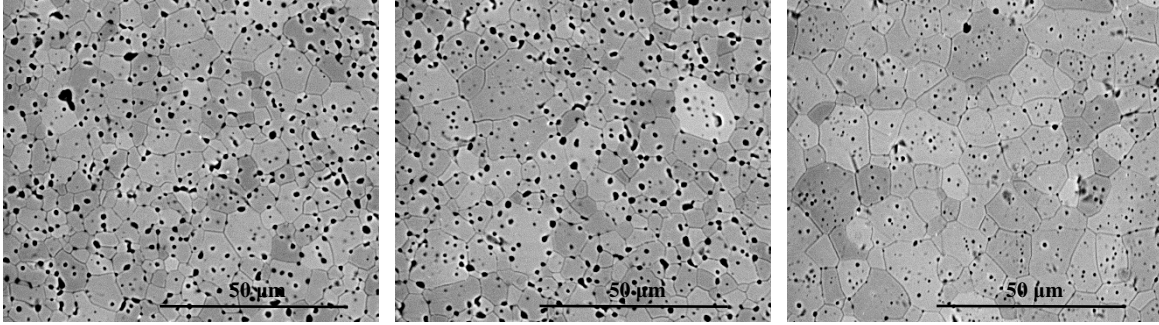

Figure A.19   ESEM images of sample formed with a uniaxial press under 21 ksi pressure and heated from room temperature to 970 °C at a rate of 5 °C/minute, held for 8 hours and air quenched (sample ID *I3*).
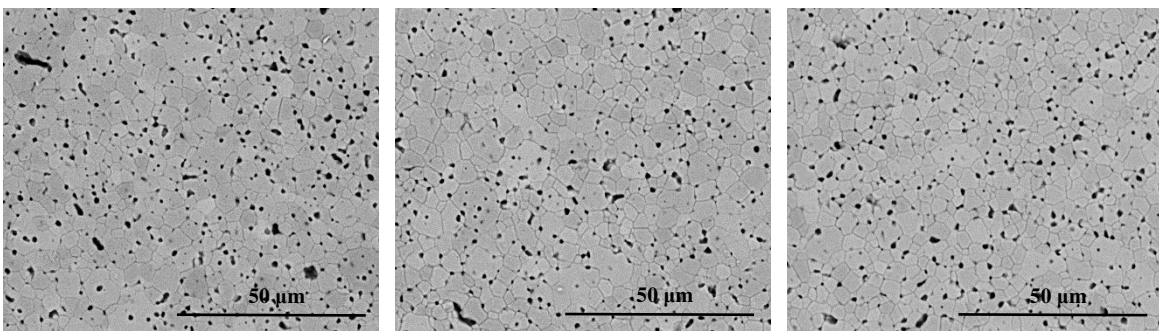
Figure A.20   ESEM images of sample formed with a uniaxial press under 25 ksi pressure and heated from room temperature to 970 °C at a rate of 5 °C/minute, held for 8 hours and air quenched (sample ID *I4*).
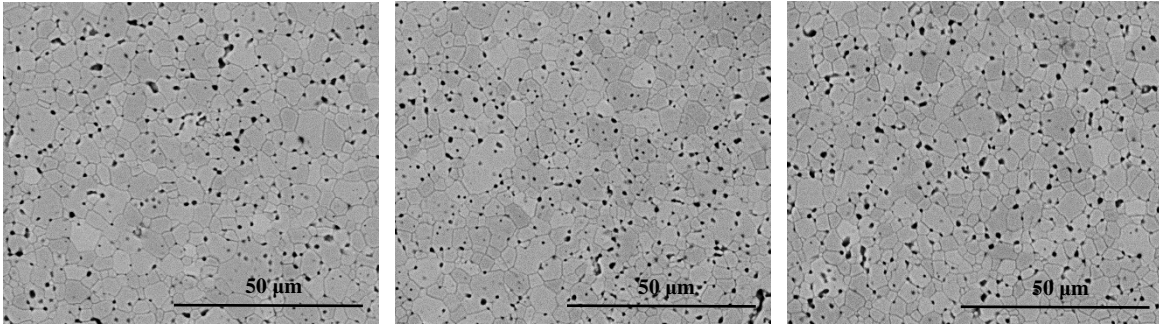
Figure A.21   ESEM images of sample formed with a uniaxial press under 28 ksi pressure and heated from room temperature to 970 °C at a rate of 5 °C/minute, held for 8 hours and air quenched (sample ID *I5*).
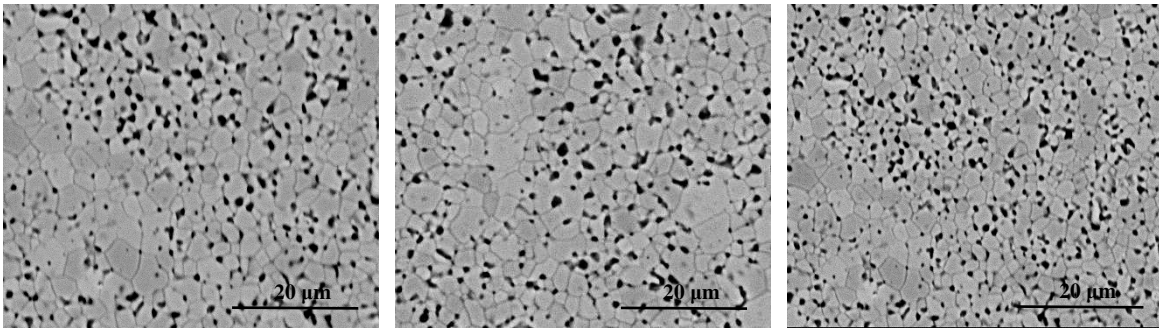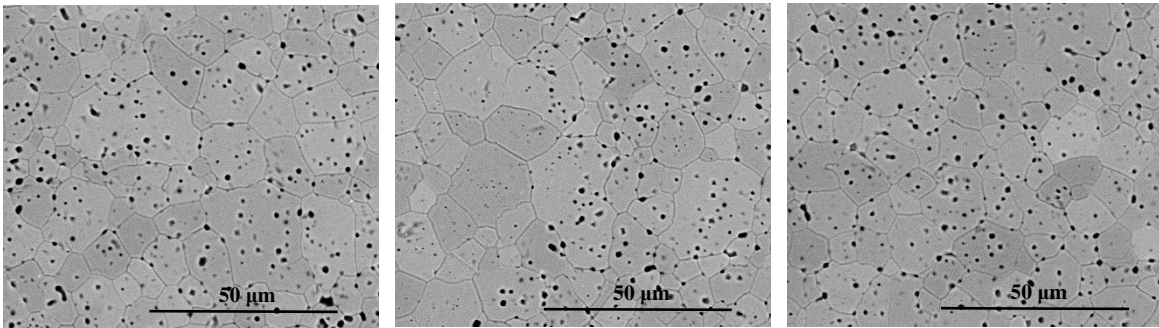

Figure A.22   ESEM images of sample heated from room temperature to 900 °C at a rate of 5 °C/minute, held for 8 hours and air quenched (sample ID *H6*).
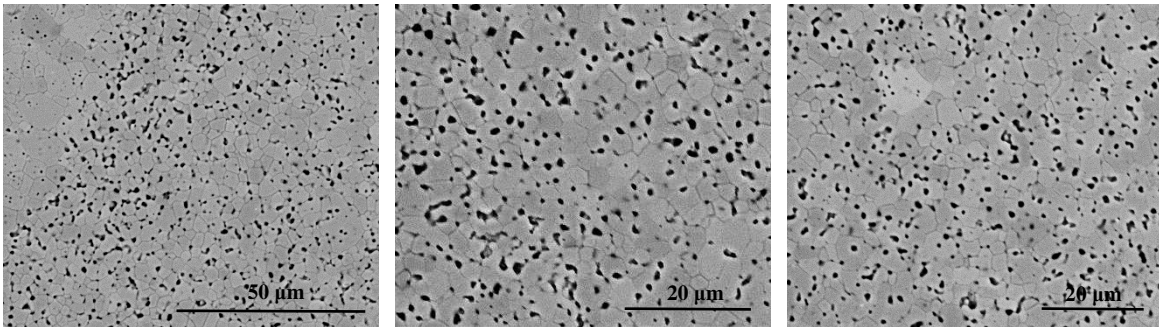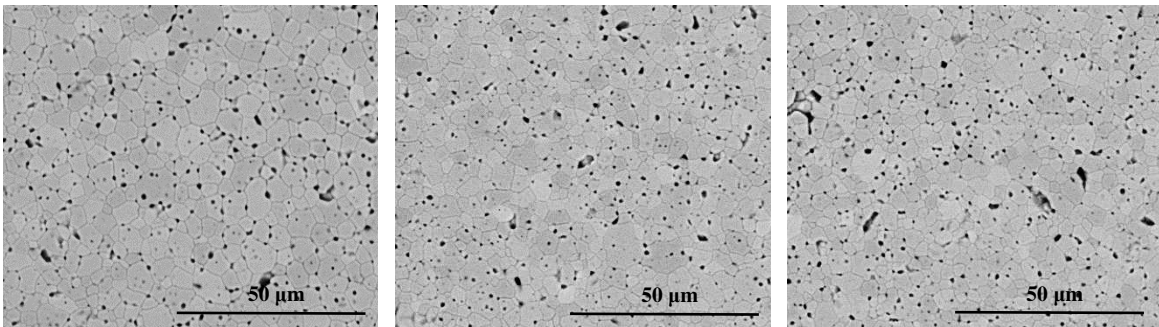

Figure A.23   ESEM images of sample heated from room temperature to 950 °C at a rate of 5 °C/minute, held for 8 hours and air quenched (sample ID *H5*).
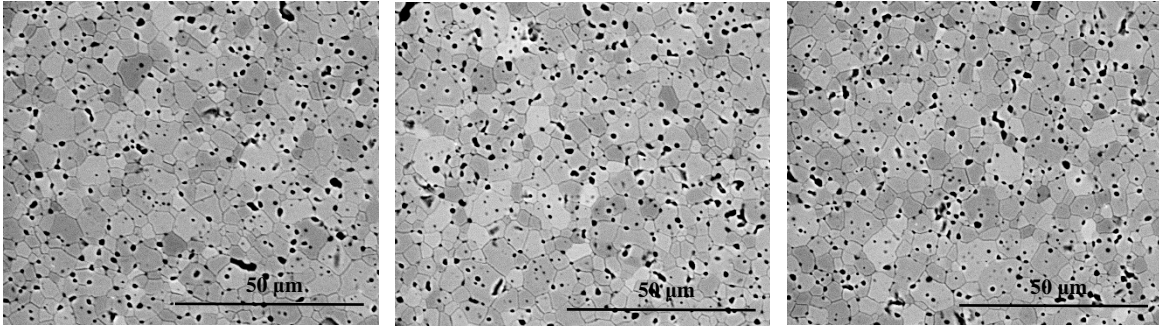
Figure A.24   ESEM images of sample heated from room temperature to 1000 °C at a rate of 5 °C/minute, held for 8 hours and air quenched (sample ID *I1*).

Figure A.25   ESEM images of sample heated from room temperature to 940 °C at a rate of 2 °C/minute, held for 8 hours and air quenched (sample ID *I10*).

Figure A.26   ESEM images of sample heated from room temperature to 970 °C at a rate of 2 °C/minute, held for 8 hours and air quenched (sample ID *I7*).

Figure A.27   ESEM images of sample heated from room temperature to 1000 °C at a rate of 2 °C/minute, held for 8 hours and air quenched (sample ID *H11*).

Figure A.28   ESEM images of sample heated from room temperature to 1050 °C at a rate of 2 °C/minute, held for 8 hours and air quenched (sample ID *H10*).
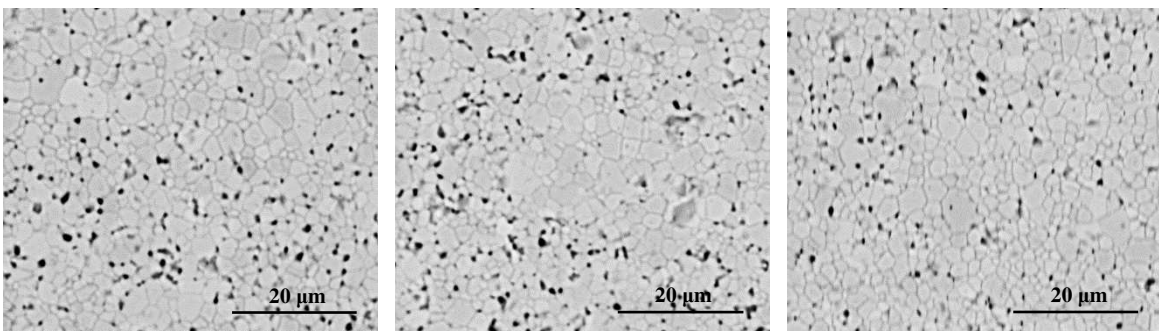

Figure A.29   ESEM images of sample heated from room temperature to 750 °C at a rate of 3 °C/minute, then heated to 940 °C at a rate of 10 °C/minute, held for 8 hours and air quenched (sample ID *I9*).
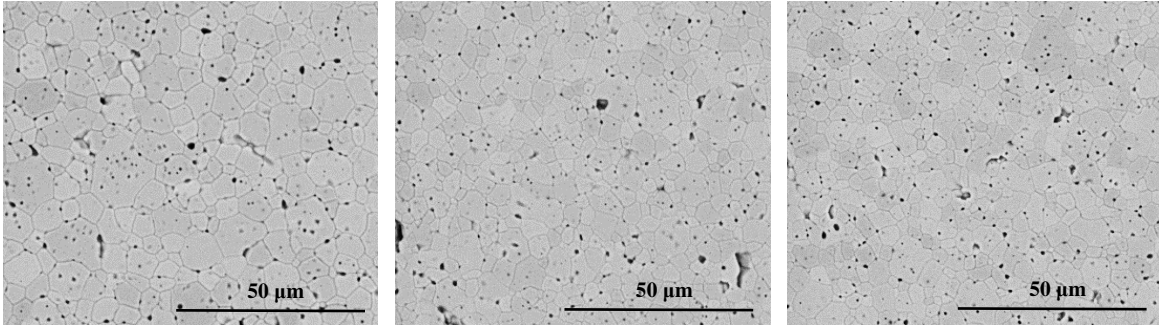
Figure A.30   ESEM images of sample heated from room temperature to 750 °C at a rate of 3 °C/minute, then heated to 970 °C at a rate of 10 °C/minute, held for 8 hours and air quenched (sample ID *I8*).
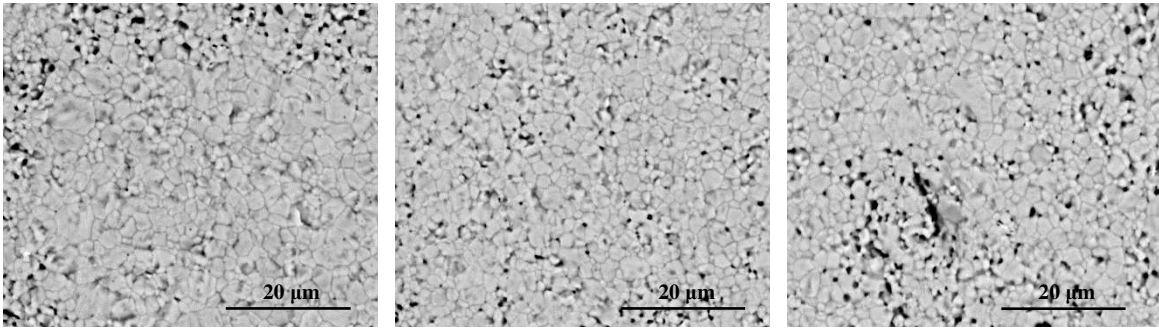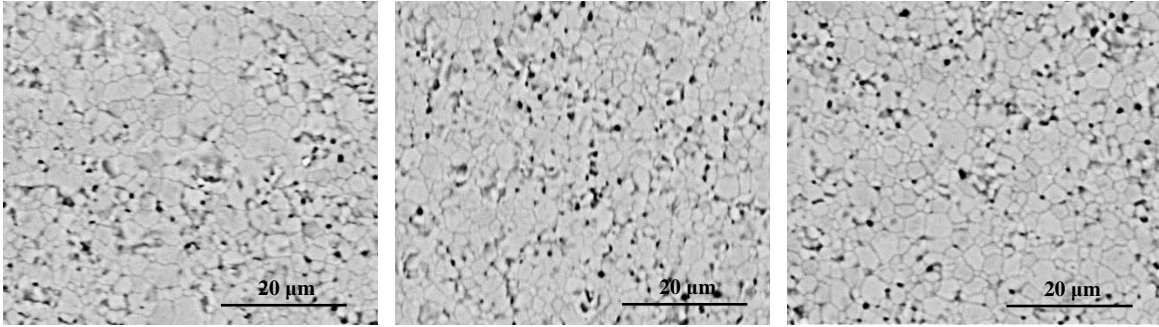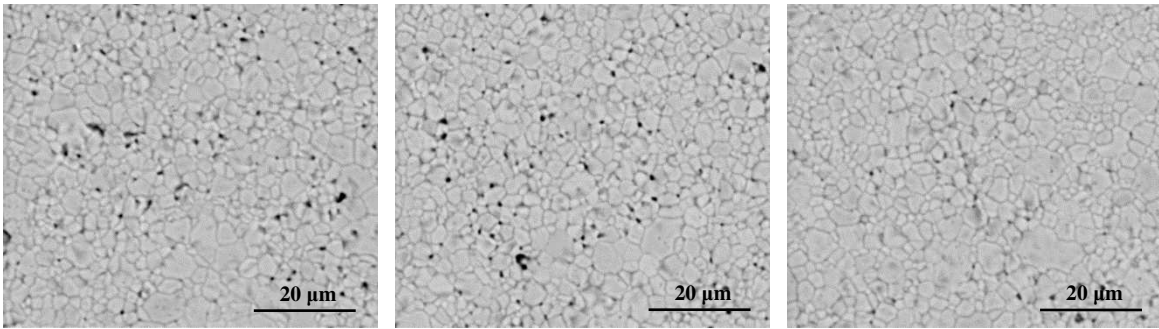

Figure A.31   ESEM images of sample for grain growth study heated from room temperature to 750 °C at a rate of 3 °C/minute, then heated to 950 °C at a rate of 10 °C/minute, held for 8 hours and air quenched (sample ID *D11*).
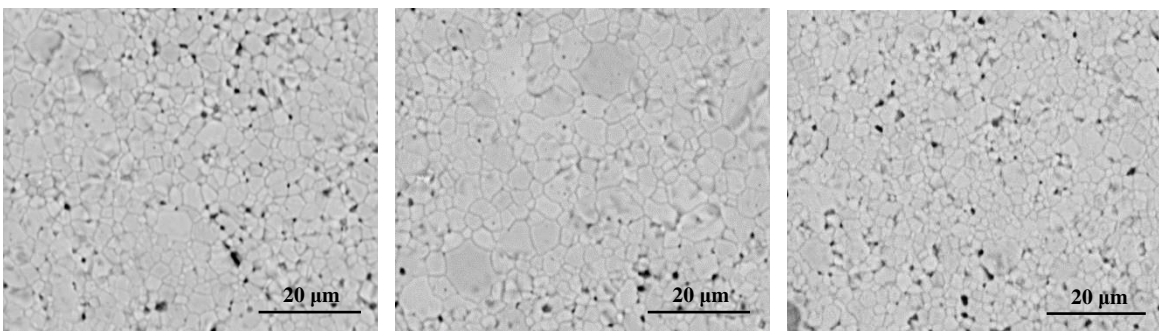

Figure A.32   ESEM images of sample for grain growth study heated from room temperature to 750 °C at a rate of 3 °C/minute, then heated to 950 °C at a rate of 10 °C/minute, held for 12 hours and air quenched (sample ID *D12*).
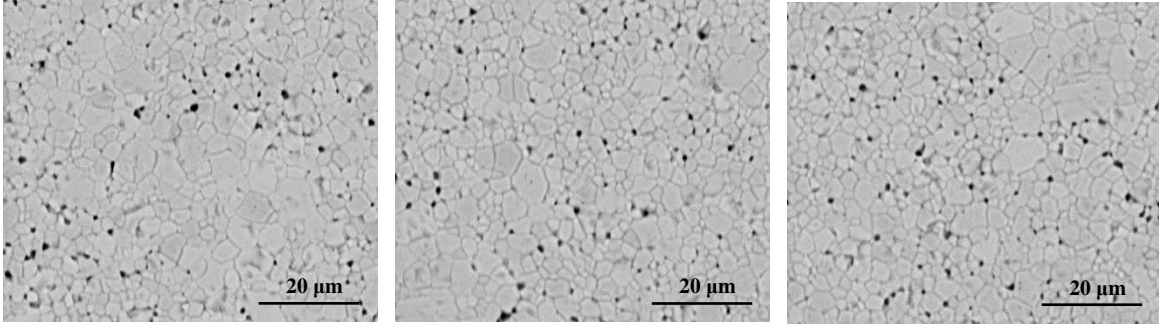
Figure A.33   ESEM images of sample for grain growth study heated from room temperature to 750 °C at a rate of 3 °C/minute, then heated to 950 °C at a rate of 10 °C/minute, held for 16 hours and air quenched (sample ID *D13*).
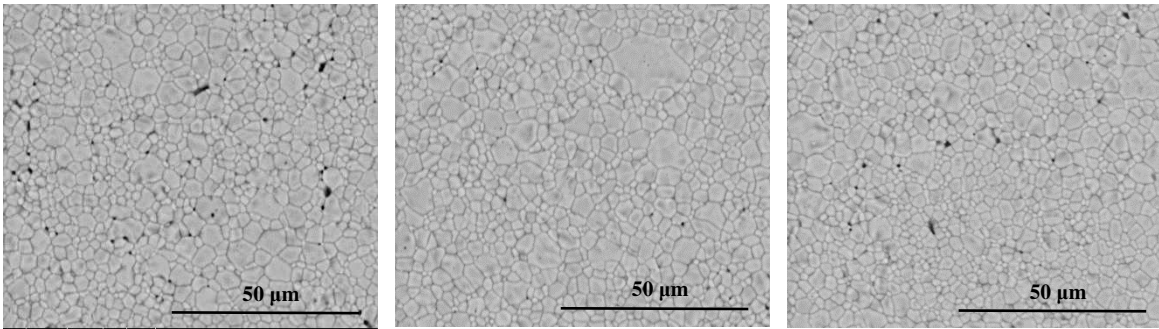

Figure A.34   ESEM images of sample for grain growth study heated from room temperature to 750 °C at a rate of 3 °C/minute, then heated to 1000 °C at a rate of 10 °C/minute, held for 8 hours and air quenched (sample ID *D14*).

Figure A.35   ESEM images of sample for grain growth study heated from room temperature to 750 °C at a rate of 3 °C/minute, then heated to 1000 °C at a rate of 10 °C/minute, held for 12 hours and air quenched (sample ID *D15*).
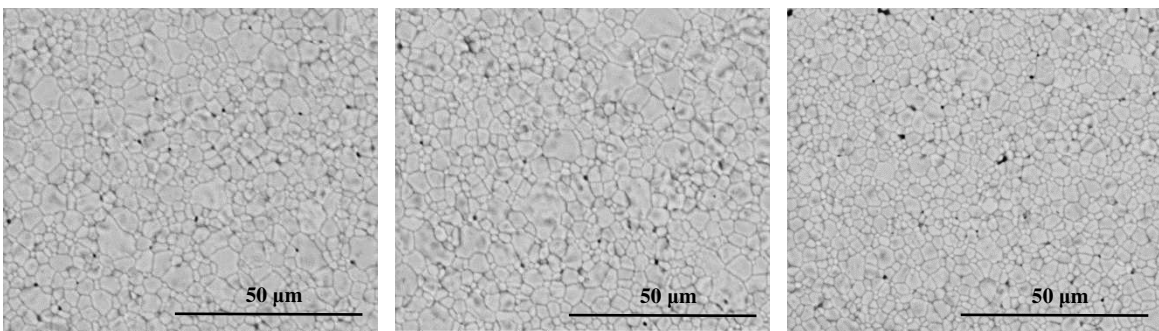
Figure A.36   ESEM images of sample for grain growth study heated from room temperature to 750 °C at a rate of 3 °C/minute, then heated to 1000 °C at a rate of 10 °C/minute, held for 16 hours and air quenched (sample ID *D16*).
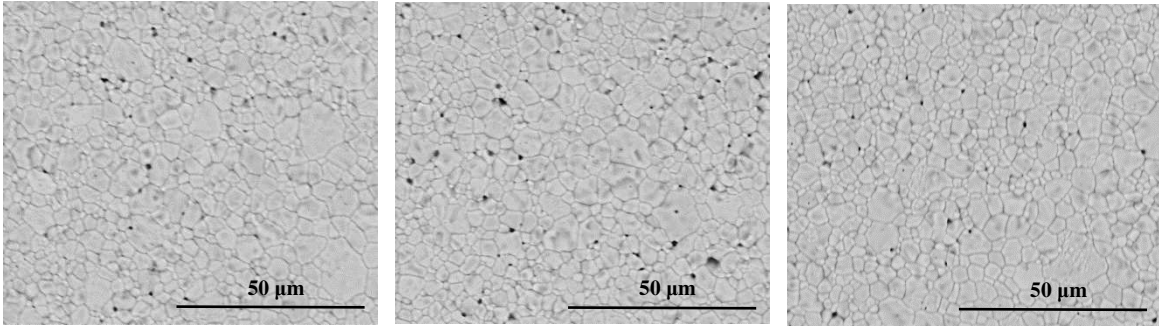

Figure A.37   ESEM images of sample for grain growth study heated from room temperature to 750 °C at a rate of 3 °C/minute, then heated to 1050 °C at a rate of 10 °C/minute, held for 8 hours and air quenched (sample ID *D8*).

Figure A.38   ESEM images of sample for grain growth study heated from room temperature to 750 °C at a rate of 3 °C/minute, then heated to 1050 °C at a rate of 10 °C/minute, held for 12 hours and air quenched (sample ID *D9*).
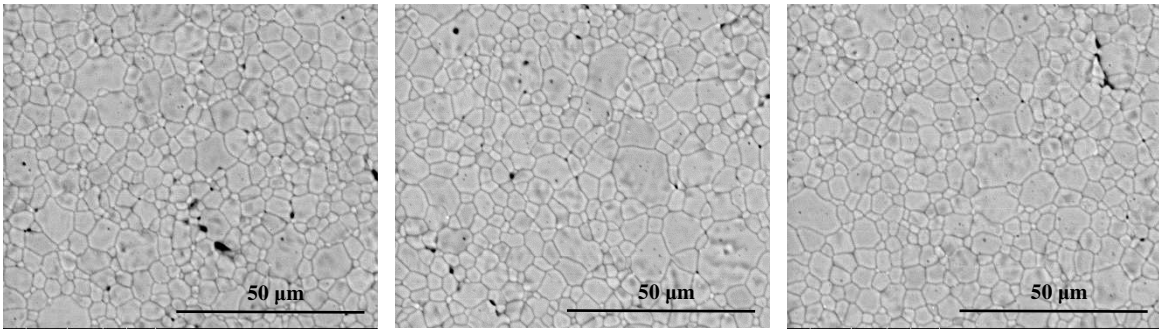
Figure A.39   ESEM images of sample for grain growth study heated from room temperature to 750 °C at a rate of 3 °C/minute, then heated to 1050 °C at a rate of 10 °C/minute, held for 16 hours and air quenched (sample ID *D10*).

Figure A.40   ESEM images of sample for grain growth study heated from room temperature to 750 °C at a rate of 3 °C/minute, then heated to 1100 °C at a rate of 10 °C/minute, held for 8 hours and air quenched (sample ID *D1*).
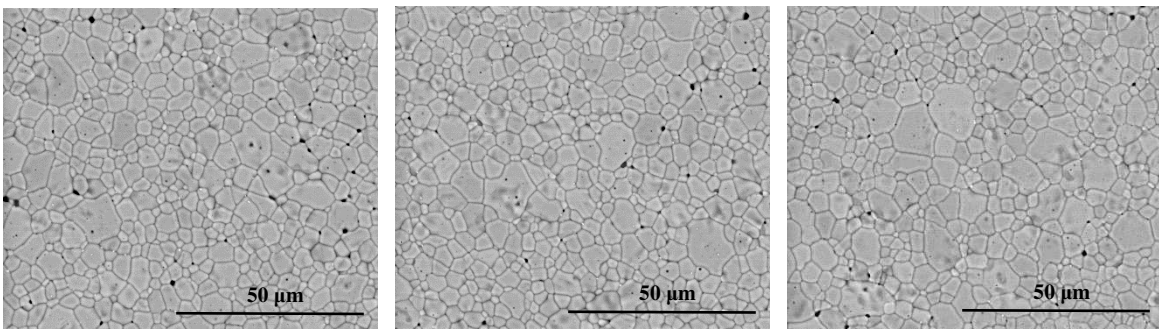

Figure A.41   ESEM images of sample for grain growth study heated from room temperature to 750 °C at a rate of 3 °C/minute, then heated to 1100 °C at a rate of 10 °C/minute, held for 12 hours and air quenched (sample ID *D2*).
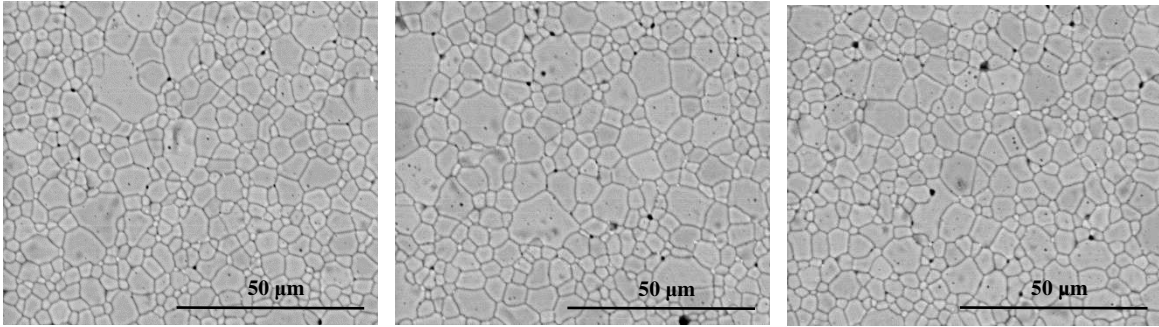
Figure A.42   ESEM images of sample for grain growth study heated from room temperature to 750 °C at a rate of 3 °C/minute, then heated to 1100 °C at a rate of 10 °C/minute, held for 16 hours and air quenched (sample ID *D3*).
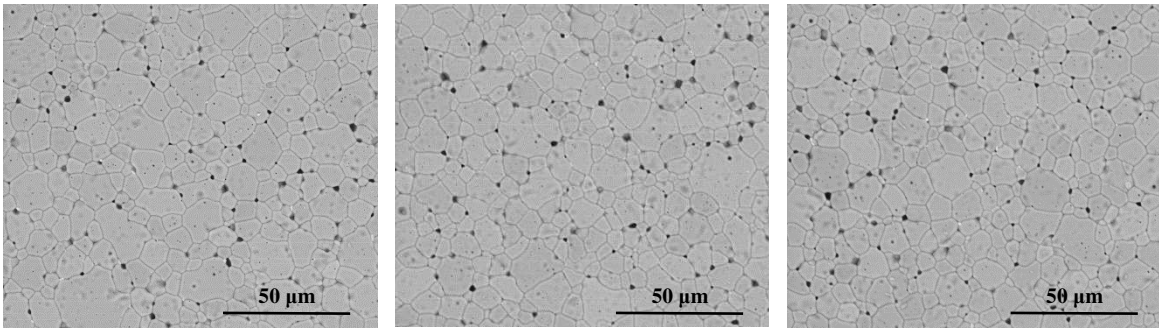

Figure A.43   ESEM images of sample for grain growth study heated from room temperature to 750 °C at a rate of 3 °C/minute, then heated to 1150 °C at a rate of 10 °C/minute, held for 8 hours and air quenched (sample ID *D4*).
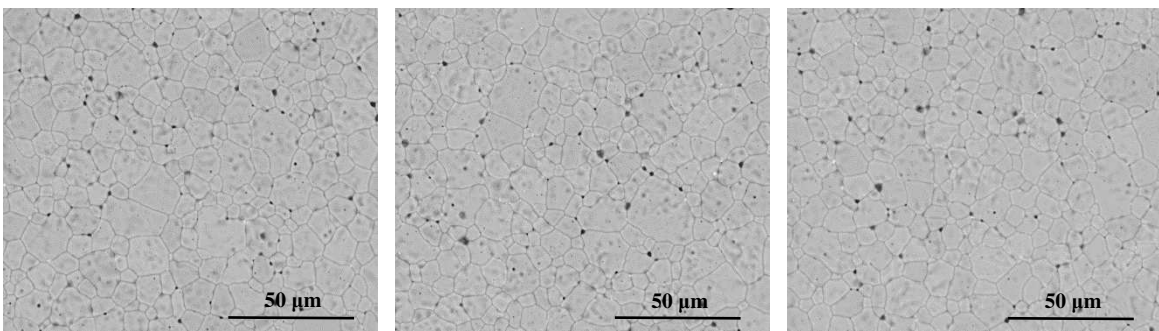

Figure A.44   ESEM images of sample for grain growth study heated from room temperature to 750 °C at a rate of 3 °C/minute, then heated to 1150°C at a rate of 10 °C/minute, held for 12 hours and air quenched (sample ID *D5*).
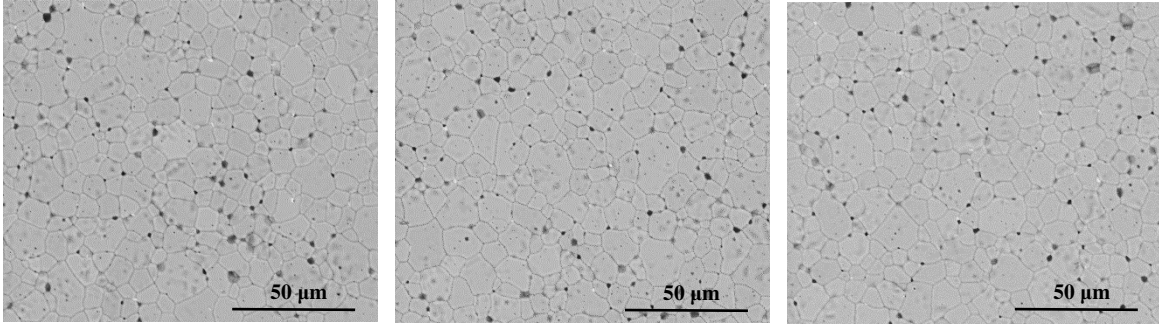
Figure A.45   ESEM images of sample for grain growth study heated from room temperature to 750 °C at a rate of 3 °C/minute, then heated to 1150 °C at a rate of 10 °C/minute, held for 16 hours and air quenched (sample ID *D6*).

A.6   Impedance Spectroscopy

Room temperature AC measurements were conducted for the single and two-phase samples before and after any non-ambient frequency sweeps to demonstrate any change in the samples throughout the non-ambient AC measurements.
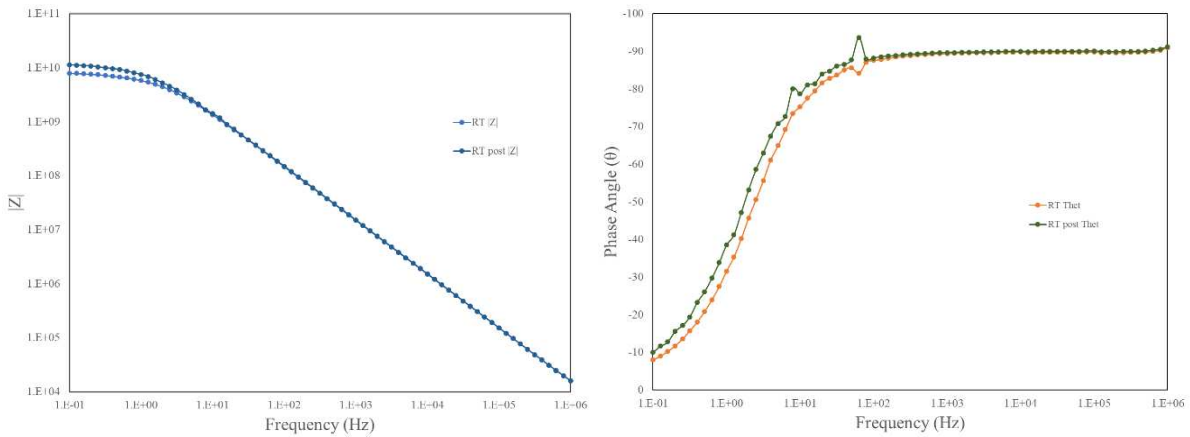

Figure A.46   Complex impedance (left) and phase angle (right) plots as a function of frequency for the single-phase sample before and after the non-ambient frequency sweeps.
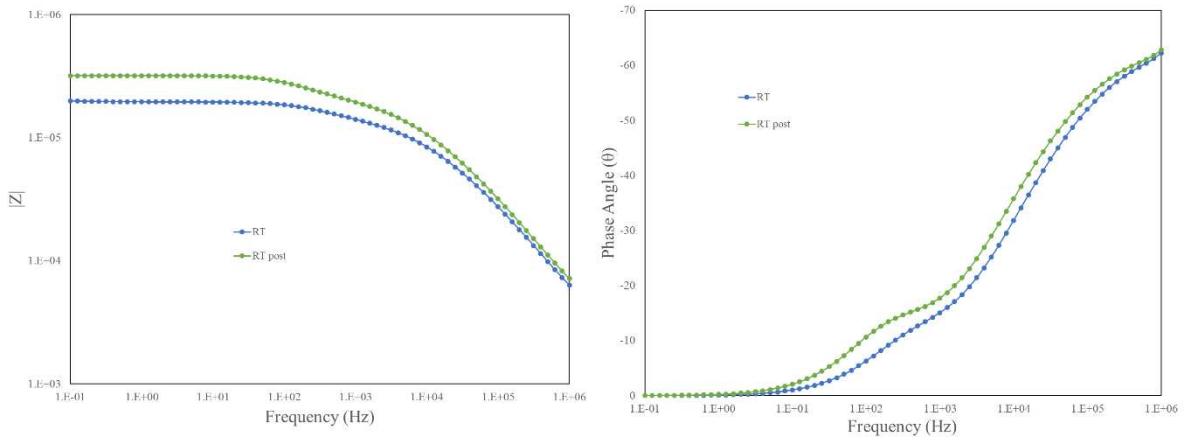
Figure A.47   Complex impedance (left) and phase angle (right) as a function of frequency for the two-phase sample before and after non-ambient frequency sweeps.

APPENDIX B: PERMISSION TO USE COPYRIGHTED MATERIAL

Permission to use image from Figure 2.1 from source [2]:

   This paper by Rost *et al.* is licensed under a Creative Commons Attribution 4.0 International License, or CC-BY 4.0. The image reproduced was not indicated as not being covered by the Creative Commons license.

Permission to use image from Figure 3.18 from source [6]:

**JOHN WILEY AND SONS LICENSE
TERMS AND CONDITIONS**

Jul 1

This Agreement between Katie Gann ("You") and John Wiley and Sons ("John Wiley Sons") consists of your license details and the terms and conditions provided by John and Sons and Copyright Clearance Center.

License Number	4631571095786
License date	Jul 17, 2019
Licensed Content Publisher	John Wiley and Sons
Licensed Content Publication	Journal of the American Ceramic Society
Licensed Content Title	Microstructural evolution and mechanical properties of (Mg,Co,Ni,Cu,Zn)O high-entropy ceramics
Licensed Content Author	Weichen Hong, Fei Chen, Qiang Shen, et al
Licensed Content Date	Oct 1, 2018
Licensed Content Volume	102
Licensed Content Issue	4
Licensed Content Pages	10
Type of use	Dissertation/Thesis
Requestor type	University/Academic
Format	Print and electronic

Figure B.1   Screenshot of permission to use image from Hong *et al.* in Figure 3.18.